COMPUTATIONAL MODELING OF MATERIALS IN POLYMER ELECTROLYTE MEMBRANE FUEL CELLS

A Dissertation

Presented to

The Academic Faculty

By

Giuseppe Brunello

In Partial Fulfillment

Of the Requirements for the Degree

Doctor of Philosophy in the

Materials Science and Engineering

Georgia Institute of Technology

August, 2013

Computational Modeling of Materials in Polymer Electrolyte Membrane Fuel Cell

Approved by:

Dr. Seung Soon Jang

School of Materials Science and Engineering

Georgia Institute of Technology

Dr. David G. Bucknall

School of Materials Science and Engineering

Georgia Institute of Technology

Dr. Thomas H. Sanders

School of Materials Science and Engineering

Georgia Institute of Technology

Dr. David S. Sholl

School of Chemical and Biomolecular Engineering

Georgia Institute of Technology

Dr. Faisal Alamgir

School of Materials Science and Engineering

Georgia Institute of Technology

Date Approved: December 14, 2012

No seas ingenuo, los dos somos inteligentes. Si vos no le entendiste, y yo no le entendí, no será que no tiene idea?

-Captain J. M. Marin-Abarquero.

To my teachers

Acknowledgments

First, I would like to thank my parents, Gustavo and Maria Carmen Brunello who are responsible for everything I am and everything I've accomplished. Upon marrying they embarked on a journey of selflessness and total sacrifice for their children. They have never looked back at the parents, family and friends they've left behind. After almost 30 years of moving, may they finally settle down to enjoy the fruits of their labor.

I would like to thank my thesis advisor, Dr. Jang, for his help and guidance. Without his advice, encouragement, and above all patience, I could not be here. Likewise the members of my thesis committee, Dr Sholl, Dr Bucknall, Dr Alamgir and Dr. Sanders, have been an invaluable help.

I am also grateful to General Motors, Ballard Power and the Department of Energy (DOE) for having supported this study. Department of Energy (DOE) grant No. DE-EE0000466.

I am also very grateful to the folk who run the MSE department, especially Susan Bowman, Tim Banks, James Cagle, and John Holthaus. From guiding the students through the bureaucracy, to installing and fixing the various facilities, they ensure everything in the materials department runs smoothly. I also would like to acknowledge Sarah, Gloria and Rebecca who throughout the years have kept my office mates' and my office clean while sharing their wisdom and warmth.

My past and present lab mates, Seung Geol, Wong Sang, and Byeong Jae have aided me by explaining procedures and patiently reminding me to register for classes. Dr. Choi, especially, has become a mentor and a good friend.

My friends, Olgert Denas, Andrea Menegazzo, Benjamin Hertzberg, Robert Rettew, Jeffery Fuller, Nicolas Espinoza Vincenzo Palermo, Francesco and Claudia Barale, and Anna Maria Conti have always been there to patiently listen to my worries, concerns. If not for every one of them, I surely would not be here. I am most indebted, however, to my friends Michael Czyrka and Juan Marin; two men with the rare moral character of putting what's right before what's easy or in their own self interest.

My aunt and uncle, Carlos and Cecilia, have been like parents to me here in Atlanta. They have shown love, caring and compassion. They went as far as opening the doors to their home when I had nowhere else to stay.

Most significantly, I would like to thank Jonida Mince. Smart, creative, generous and hard working, she loves me for no other reason than "I'm good to her" – whatever that means. Her spirit and her life is living proof of the tenacity of the human spirit to overcome the most insurmountable problems. Despite numerous adversities, any one of which would have broken most people's spirits, she steadfastly believes that God has only challenged her. And then, only to achieve greater things. She is an example to look up to and follow every day.

Table of Contents

List of Tables

List of Figures

Summary

Fuel cells have the potential to change the energy paradigm by allowing more efficient use of energy. In particular, Polymer Electrolyte Membrane Fuel Cells (PEMFC) are interesting because they are low temperature devices. However, there are still numerous challenges limiting their widespread use including operating temperature, types of permissible fuels and optimal use of expensive catalysts. The first two problems are related mainly to the ionomer electrolyte, which largely determines the operating temperature and fuel type. While new ionomer membranes have been proposed to address some of these issues, there is still a lack of fundamental knowledge to guide ionomer design for PEMFC.

This work is a computational study of the effect of temperature and water content on sulfonated poly(ether ether ketone) and the effect of acidity on sulfonated polystyrene to better understand how ionomer material properties differ. In particular we found that increased water content preferentially solvates the sulfonate groups and improves water and hydronium transport. However, we found that increasing an ionomer's acid strength causes similar effects to increasing the water content.

Finally, we used Density Functional Theory (DFT) to study platinum nano-clusters as used in PEMFCs. We developed a model using the atom's coordination number to quickly compute the energy of a cluster and therefore predict which platinum atoms are most loosely held. Our model correctly predicted the energy of various clusters compared

to DFT. Also, we studied the interaction between the various moieties of the electrolyte including the catalyst particle and developed a force field.

The coordination model can be used in a molecular dynamics simulation of the three phase region of a PEMFC to generate unbiased initial clusters. The force field developed can be used to describe the interaction between this generated cluster and the electrolyte.

Chapter I

Introduction

Fossil fuels have been the primary energy source for centuries. Fossil fuels such as petroleum, natural gas and coal, encompass most of our current energy consumption, and demand is still increasing. In particular, the transportation sector relies on oil; over 90% of the energy used in the transportation sector is oil. [1] However, combustion of hydrocarbon containing fuels is a major contributor to greenhouse gas emissions, which are responsible for radiative forcing and therefore global warming. [2] Thus, it is important to reduce the amount of fossil fuels used.

Many upcoming technologies promise to help reduce oil use, including hybrid-electric, battery, advanced diesel, and fuel cell technologies. [3] In particular, fuel cells, especially Polymer Electrolyte Membrane Fuel Cell (PEMFC), hold great promise. Fuel cells are similar to batteries, in that they use an electrochemical reaction to convert chemical energy directly into electrical energy. While a battery stores the chemical energy internally and provides electrical power until it runs out of the reactants, the fuel cell generates electricity indefinitely as long as fuel, oxygen and hydrogen, are provided. Unlike batteries fuel cells replenish their reactants from an external store.

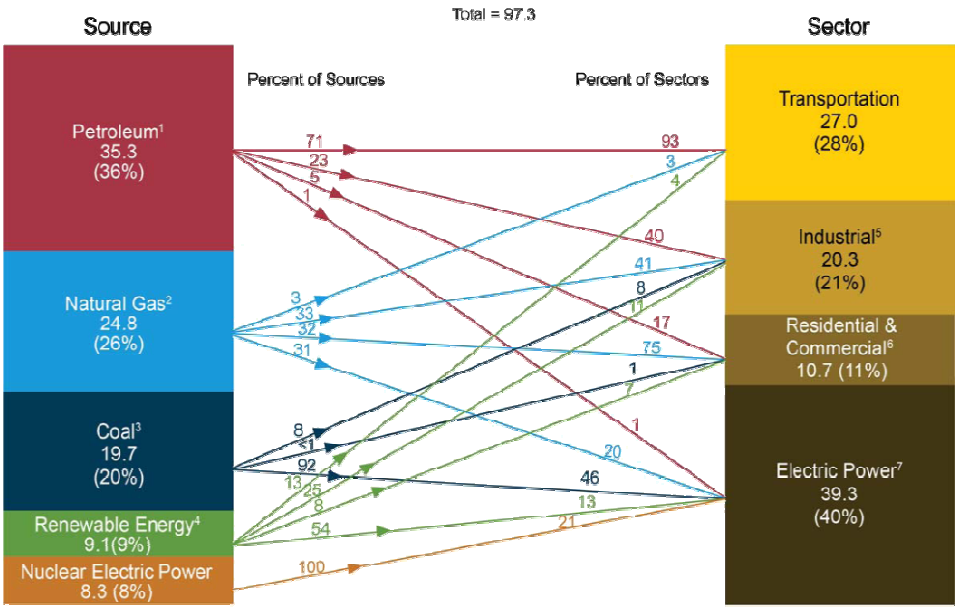

Figure 1: Breakdown of the sources and users of energy in the United States as compiled by the Department of Energy [1]

However, the cost and performance of these fuel cells cannot currently challenge the dominance of the internal combustion engines in the transportation sector. Therefore, for fuel cells to compete the cost must be lowered and the performance improved. Another challenge comes from the storage of the fuel, usually hydrogen. Hydrogen has low volume energy density, so high pressure containment vessels are needed to store it.

A possible solution to this problem is using a hydrocarbon to store hydrogen. Direct methanol fuel cells are fuel cells that use methanol directly without the need of an external reformer. Since methanol is injected into the fuel cell, the electrolyte material chosen must be compatible with methanol. [4]

Most importantly, suitable fuels for use in a fuel cell are largely determined by the electrolyte material chosen. For PEMFCs, a good membrane material is one that is a good electrical insulator, has a low diffusion rate for any species but protons, low electro-osmotic water drag and works at a wide range of temperatures.[4] These properties are largely determined by the microstructure of the material as well as the type of polymer.

1-1. Overview

Fuel cells are similar to batteries, in that they use an electrochemical reaction to convert chemical energy directly into electrical energy. Their main advantage is their reactants are easily replenished and the by product of the reaction is water vapour. As a result fuel cells can be a clean, carbon neutral, technology [4].

A fuel cell is a stack of various layers, the electrode and the electrolyte. The electrode layer is an electrically conductive material with a catalyst coated. This electrically conductive material must be porous to allow the reactant gasses to flow in and out of the system. The electrolyte is a material that allows for ionic conduction between the electrodes. The interface between the electrolyte and electrode layers is called the catalytic layer. Due to their low output voltage, fuel cells are connected in series and referred to as a fuel cell stack. PEMFCs are fuel cells that utilize a two phase hydrated polymer membrane as the electrolyte. This electrolyte allows the fuel cell to operate at low temperatures[4]

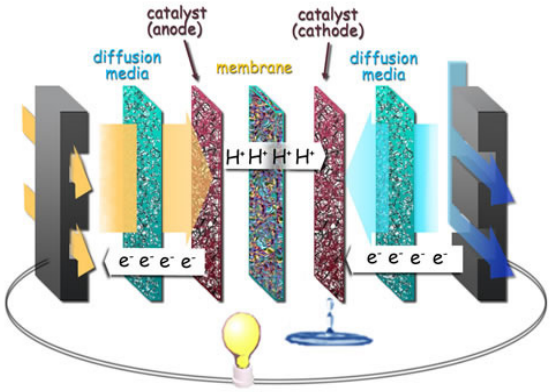

Figure 2: A fuel cell is a stack of several layers controlling an electrochemical reaction to transform the chemical energy directly to electrical energy. The interface between the electrode and electrolyte is the catalyst layer and it is designed to allow efficient transport of gases, achieve effective coupling between the layers, catalyze the reactions and provide a good electrical connection to the electrode.[5]

PEMFCs are low temperature fuel cells that operate between 80 to 105 C. They utilize a hydrated ionomer as an electrolyte. Due to the ionomer's acid groups, the polymer absorb water and therefore ionizes the acid groups providing a pathway for hydrogen transport. Since, the polymeric ionomer has a hydrophobic backbone the membrane develops two phases, a hydrophilic and hydrophobic phase [4, 6]. The former consists of interconnected waters domains around the acid groups, providing the easiest path for proton conduction and the latter consists of the hydrophobic polymer domain, ensuring selectivity of the membrane as well as mechanical stability of the membrane. [6]

The membrane materials largely determines how the PEMFC works, in particular the operating temperature and fuel used. Nafion, the most popular ionomer, has good proton conductivity but it cannot be used with methanol or at high operating temperatures. S-PEEK, on the other hand has lower proton conductivity but can operate at higher temperatures and can use methanol.

1-1.1 Efficiency

Fuel cells convert the differences in electrochemical potential directly to electrical energy without the intermediate step of establishing a temperature difference. As a result fuel cells can be more efficient than heat engines because Carnot efficiency limits are not applicable [7]. However, the fuel cell has unique loss mechanisms that limit the actual efficiency. These loss mechanisms are seen as a drop in electrical potential and include the Ohmic resistance of ions traveling through the membrane material and, in PEMFCs,

the kinetic losses at the anode and cathode to ionize the oxidizer and the fuel. The anodic losses are less significant when compared to the losses at the cathode due to the kinetic difficulties of oxygen reduction reaction (ORR reaction) [8].

1-1.2 Issues

There are currently three large issues with PEMFCs, the fuel they use, their operating temperature and the expensive catalyst materials required.

First, compared to other high temperature fuel cell technologies, PEMFC's much lower operating temperatures is a great advantage: in other fuel cell technologies the fuel cell designer must choose materials that can withstand high temperatures, and account for significant thermal expansion. However, PEMFC's low temperature inhibits the ORR reaction and, if non pure reactant gases are used, allows the catalyst to become poisoned. Also, higher operating temperatures should raise proton mobility, lowering the membrane's Ohmic resistance [4, 8].

Second, due to the difficulties producing, storing and delivering hydrogen, it is also desirable to use these membrane materials with other fuels, for example methanol. Whereas high temperature fuel cells can use the high temperatures to reform fuels into hydrogen, PEMFCs attempt to do this directly in the anode. A problem arises where the fuel has a significant permeability to the electrolyte membrane. Then the fuel crosses over to the cathode and reacts with the oxygen directly without producing electrical current.

Finally the catalyst materials used in PEMFCs are expensive and therefore it is very important that they are fully utilized, and have a long lifetime. Due to its excellent catalytic properties, platinum is the most commonly used catalyst. [9]However, researchers want to improve PEMFC performance by ensuring as much of the platinum surface is available for catalysis. It is important to have a atomistic interpretation of the interaction between the moieties in a PEMFC and the catalyst, as well as have a firm understanding of the catalyst's energy behavior.

In Chapter 2 and 3 we investigate S-PEEKs behavior with changes in temperature and water weight. In Chapter 4 we study the effect of changing an ionomer's acid strength on its proton conduction ability and finally in Chapter 5 we discuss a model we developed for platinum nano-clusters and their interaction with Nafion segments.

1-2. Theoretical Basis

Computational physics is based on the assumption that a materialistic, quantitative, interpretation of reality correctly describes physical behavior – that is that matter and energy act according to the fundamental mathematical equations of physics. It assumes that, taken to the limit, the laws governing elementary particles will correctly describe higher order systems including chemical and biological systems. [10] Therefore, Quantum Electrodynamics can be used to describe relativistic quantum mechanics. For the simpler case of non-relativistic quantum mechanics, Schrodinger's equation describes the interaction between particles. By Bohr's correspondence principle, Quantum

Mechanics reproduces classical physics. [11] Usually this requires few particles. Newton's laws describe, therefore, most physical phenomena. Exceptions include chemical reactions, which are a quantum effect, and heat capacity, which is inaccurately described by classical statistical thermodynamics.

1-2.1 Density Functional Theory

The start of the twentieth century was very exciting for physicists as new experimental discoveries led them to rewrite much of their field. Only thermodynamics was relatively unscathed as Gibb's and Boltzmann had formulated them; the ultraviolet catastrophe was solved by Planck, who treated light as discrete units of energy, called quanta. [12] Initially, this was merely a pragmatic approach to obtain the correct black body distribution. The DeBroglie generalised this idea was generalized to all matter. [13] The "equation of motion" of a wave travelling much slower than the speed of light is Schrodinger's wave equation, which is a linear time dependent non-relativistic partial differential equation, shown below:

$$i\hbar \frac{\delta}{\partial t} \Psi(r,t) = [\frac{-\hbar^2}{2m} + V(r,t)]\Psi(r,t) \qquad (1)$$

The equation is separable, meaning that the time dependent and time independent parts can be solved independently of each other, resulting in the time-independent Schrodinger's equation. [11] The time dependent part is trivial to solve in contrast to the time independent part. However, there is a solution to the particle in a radially symmetric

parabolic well. This is important since this describes the hydrogen system very well. Another approximation used in quantum chemistry is the Born-Oppenheimer approximation, which separates the nuclear and electronic wavefunctions by exploiting the large mass ratio between electrons and nuclei. [14] The classical analog is that the nuclei are assumed immobile compared to the electrons. However, in general, there are no analytical solutions for systems with more than two bodies. The two body system, however, is an excellent first order approximation from which numerical solutions can start.

There are numerous methods to numerically solve Schrodinger's wave equation. In particular Hartree-Fock (HF) and post HF methods are notable. [15] HF, while capable of describing certain systems well, cannot describe the ground state energy correctly in the limit of an infinitely large basis set. This systematic error is known as the HF limit [15], and post-HF methods attempt to fix this. However, they scale very poorly with increasing number of electrons. Therefore, most post-HF methods cannot be used except for the simplest of systems.

Fortunately, it is possible to solve for the energy of a quantum mechanical system by using the electron density instead of electron wave function, and, conceptually, this method is proven to be theoretically exact. Specifically the two theorems by Hohenberg and Kohn [16] proved that it is possible to use electron density. The first theorem states that the external potential is a unique functional of the electron density $\rho(r)$; that is the electron density uniquely determines the external potential, V_{ext} , therefore $H_{ext,}$ and so all the properties of the system. The second theorem states that the ground state density can be obtained variationally. While these theorems have been used to develop Density

Functional Theory, there remains the problem in DFT that the exact functional is unknown.

The quality of DFT relies on the quality of the functional used. Although the HK theorems guarantee that such a functional exists, it is unknown. Instead characteristics of the functional are known and functionals are created that reproduce these qualities and needed features. Currently, therefore, DFT has a fundamental flaw that it has overcome largely on the strength of it's accurate predictions. [17]

1-2.2 Kohn – Sham Theory

Although the Hohenberg-Kohn theory allows the reformulation of QM in terms of density, it does not guarantee exact solutions. In the Hohenberg-Kohn theory, both the kinetic and exchange-correlation energy are approximated. Instead, Kohn and Sham theory [18] replaces the system of real interacting particles with a system of non-interacting particles whose density is equal to the same density of the, real, interacting particles. The particles in this system now act under an effective potential the Kohn-Sham potential, $v_s(r)$. The Kohn-Sham wavefunctions are the lowest energy solutions to:

$$(-\frac{\hbar}{2m}\nabla^2 + v_s(r))\phi_i(r) = \varepsilon_i\phi_i(r) \qquad (2)$$

Since the Kohn-Sham particles are non interacting, the wavefunction that is a solution to this equation is single Slater determinant. This point is what makes DFT such a powerful tool in quantum chemistry, as it substitutes solving a many electron problem to a single electron problem. The orbitals used in the Kohn-Sham formulation have little physical meaning, except that their number density, shown in equation 3, is equal to the number density of the original problem we were trying to solve. [17]

$$\rho(r) = \sum_{j} \psi_j(r)\psi_j^*(r) \tag{3}$$

The Kohn –Sham equation (2) is solved iteratively until the density of the orbitals converge. In practice, the iteration is stopped when the energy converges to within a set tolerance. The energy is the ground state energy of the system. [17]

1-2.3 Molecular Dynamics

Molecular Dynamics (MD) is a computational method of simulating atomic systems based on Newton's laws of motion show below: [19]

$$\vec{F} = \frac{d\vec{p}}{dt} = m\frac{d\vec{v}}{dt} + \vec{v}\frac{dm}{dt} \tag{4}$$

Given that we know atoms' atomic weights (in our case, time independent), if we know the forces acting upon the atoms, we can calculate their acceleration. To obtain the acceleration, we need to have the forces acting on it, which can be described using a force field. The acceleration is not constant, but depends on the positions of the atoms. To integrate this expansion, we use the Verlet algorithm. [20] The Verlet algorithm is chosen because it has good stability, preserves energy well and is a fourth order expansion. This without being a significant computational cost over Euler's method.

MD can have different types of boundary conditions, including vacuum conditions where the atoms are placed in an infinite space, or in a periodic cell. A periodic cell is a cell containing boundaries where all physical quantities beyond the boundary are equivalent to the cell at the opposite end. Periodic conditions allow the simulation to get rid of boundary effects. Although a periodic simulation is essentially "infinite" in size, it introduces a source of error because there are finite unique moieties and they are interacting with images.

A force field is a set of parameters for a given equation used to calculate the force acting on atoms. It is a fit of the energy landscape of a given set of atoms. Force field, therefore, are approximations, or fits, to the real energy of a set of i atoms in position r_i. While many different force fields are available, built for specific purposes, we used the DREIDING force field[21] as previously used to study Nafion[22-28] and Dendrion systems[29, 30]. Our lab has successfully used the DREIDING force field in other molecular systems including hydrogel systems,[31, 32] liquid-liquid and liquid-air interfaces[33, 34] and molecular self-assembly systems. [35-40] The water model we use is the F3C force field.[41] These force field parameters are described in the original

papers[21, 41, 42] and a previous study[26] on hydrated Nafion. Our force field has the form:

$$E_{total} = E_{vdW} + E_{Q} + E_{bond} + E_{angle} + E_{torsion} + E_{inversion} \quad (5)$$

where E_{total}, E_{vdW}, E_{Q}, E_{bond}, E_{angle}, $E_{torsion}$ and $E_{inversion}$ are total energies, van der Waals, electrostatic, bond stretching, angle bending, torsion and inversion components, respectively.

Due to the periodic box, the system simulated size is infinite-like. A problem arises for calculation of the electric field since the electric field decays too slowly (1/r). Instead the long range interaction is calculated in reciprocal space. The Particle-Particle Particle-Mesh (PPPM) [43] that we used is one such method to calculate the electrostatic interactions.

A Molecular Dynamics (MD) code integrates Newton's equations to create a time evolution of the material. Although this is conceptually straightforward, implementing an MD code that is fast, yet stable and physically consistent is not trivial. Problems with numerical stability are those problems that arise from the numerical approximations necessary to perform the calculations in finite time. Other problems include codes that don't preserve the total energy of the system, momentum or angular momentum (zero by symmetry for a periodic box) in the long run. Furthermore, the natural ensemble of a MD code is the NVE ensemble (Newton's laws preserve energy and our simulation box is fixed). However, it is necessary to simulate materials systems at a fixed temperature (or

pressure). Thermostats and barostats are modifications to the governing equations of motion such that a constant temperature and pressure is maintained.

Creating a fast, stable MD simulator is outside the scope of our work, and it is not necessary. Several high quality, open source, codes that implement the necessary features (i.e. Nose-Hoover thermostat [44-46]) are available that use advanced computer programming techniques, including the Message Passing Interface (MPI) for parallelization. This allows us to scale our simulations by adding CPU and memory. Also, since the start of this work, many of the codes used in this study have added the ability to use General Purpose GPUs (GPGPU), which harness the massively parallel architectures developed for gaming purposes. For our work, we used LAMMPS, (Large-scale Atomic/Molecular Massively Parallel Simulator) from Plimpton at Sandia[47, 48] with modifications to handle our force fields.[26, 34].

1-3. Computational Characterization

Aside from simulating a physical system, the systems must also be characterized to obtain the relevant materials data.

1-3.1 Single Point Energy and Binding Energy

Given a set of atoms, of size n, we can define a vector *r* of dimension 3N that describes the arrangement of the atoms in the system. Therefore, we define the energy of the system as a function of *r*, the potential energy surface. The single point energy is the energy of a specific point in the vector space spanned by *r*. Single point energy calculations can be performed using quantum mechanical methods.

If the point is an energy minimum, the single point energy can be used to calculate the binding energy of the system with respect to its constituents. If the system is not at the energy minimum then, using numerical optimization methods, the arrangement of atoms is moved until a minimum is found. While there are optimization algorithms that guarantee finding the absolute minimum energy point, the optimization algorithms commonly use do not guarantee global optimization of the atoms. It is very important, therefore, to choose a suitable starting position and often multiple different starting positions are used.

1-3.2 Radial distribution function (RDF)

This pair correlation function, $g_{A-B}(r)$ indicates the relative probability (the probability is relative to an infinite separation distance) of finding B atoms at a distance *r* from the A atom, averaged over the equilibrium trajectory as in Equation (2)

$$g_{A-B}(r) = \left(\frac{n_B}{4\pi r^2 \Delta r} \right) \Big/ \left(\frac{N_B}{V} \right)$$

(6)

Here n_B is the number of B particles located at the distance r in a shell of thickness Δr from particle A, N_B is the number of B particles in the system, and V is the total volume of the system. The radial distribution function, therefore can be thought of as the ratio of the local number density of species B in a thin shell about A divided by the global number density.

Assuming only pairwise interactions, all thermodynamic properties of a materials can be calculated from the RDF . Furthermore, it is related to the structure factor commonly used in materials research: except for differences in contrast, the structure factor of a material is the Fourier transform of its RDF.

Finally, since the RDF is the ratio of B atom's number densities, the number of B atoms surrounding an A atoms is easily calculated by radially integrating the RDF with the appropriate change of variables.

$$CN = \int_0^{r_0} 4\pi\rho g(r) r^2 dr$$

(7)

By defining a solvation shell as the distance bounded by two troughs in the RDF, we calculate the coordination number of species B surrounding species A by the radial integral of the RDF within the limits of integration of 0 to the first location of the first trough. When calculating the CN for many systems we use a constant r_o for a particular pair.

1-3.3 Mean Square Displacement (MSD)

The mean square displacement is defined as $\langle (r(t)-r(0))^2 \rangle$; that is, it is the ensemble average of the square of the displacement as a function of time. The MSD is used to calculate the diffusion rate of a moiety using the following equation:

$$D = \lim_{t\to\infty} \frac{1}{6t^{\nu}} \left\langle \left(r(t) - r(0)\right)^2 \right\rangle \tag{8}$$

where r(t) an r(0) are the positions of water at a certain time (t) and at the beginning (t=0), respectively, and ν is the exponent that is unity for Gaussian diffusion. Gaussian, or Einstein, diffusion is when this exponent equals one. If this is the case, the diffusion coefficient is proportional to the slope of the linear asymptote of the MSD plot. The proportionality constant depends on the geometrical dimension: 6 for 3D diffusion, 4 for 2D diffusion.

1-3.4 Structure Factor

In this study, we calculated the structure factor, $S(q)$, in order to characterize the nanophase-segregation. This is widely implemented experimentally using small angle scattering experiments (SAXS and SANS). The structure factor, $S(q)$ has been used previous studies on copolymer systems[49] and polymer blend systems[50] as well as hydrated polymer membranes.[26, 29, 30] It is defined as follows:

$$\mathbf{S}(\mathbf{q}) = \left\langle \sum_{r_i} \sum_{r_j} exp\left(i\mathbf{q} \cdot \mathbf{r}_{ij}\right)\left(\xi^i \xi^j - \langle \xi \rangle^2\right) \right\rangle / L^3 \tag{9}$$

where the angular bracket denotes a thermal statistical average, ξ^i represents a local density contrast, $(\phi_A^j - \phi_B^j)$, $\boldsymbol{q}$ is the scattering vector and $\boldsymbol{r}_{ij}$ is the vector between the sites *i* and *j*. While SAXS and SANS experiments measure the electron density contrast and deuterium density contrast respectively, our structure factor is calculated from an artificial density contrast as follows. The local density variables are $\boldsymbol{\phi}_A^j$ and $\boldsymbol{\phi}_B^j$: ϕ_A^j is equal to 1 if the site *j* is occupied by a hydrophilic entity such as water or sulfonate group and equal to 0 otherwise, and ϕ_B^j is equal to 1 if the site is occupied by hydrophobic moiety (for example the hydrophobic PEEK backbone) or equal to zero otherwise. The quantity **S**(**q**) is spherically averaged as follows:

$$S(q) = \sum_{|\mathbf{q}|} \mathbf{S}(\mathbf{q}) / \sum_{|\mathbf{q}|} 1$$

(10)

with $q = (2\pi / L)n$, where $n = 1, 2, 3, \cdots$ denotes that, for a given n, a spherical shell is taken as $n - 1/2 \le qL/2\pi \le n + 1/2$.

Chapter II

A Molecular Dynamics Simulation Study of Hydrated Sulfonated Poly (Ether Ether Ketone) for Application to Polymer Electrolyte Membrane Fuel Cells: Effect of Water Content

The work presented here was published by the author in the Journal of Renewable and Sustainable Energy. [51]

Sulfonated poly(ether ether ketone), S-PEEK with 40 % of degree of sulfonation was studied using full atomistic molecular dynamics simulation at various water contents such as 10, 13 and 20 wt %. The investigation focused on the nanophase-segregated structures, specifically those of the sulfonate group and water phases. By analyzing the pair correlation function, it is found that as the water solvation of sulfonate groups proceeds more with increasing water content, the distance between sulfonate groups is increased from 4.4 Å (10 wt %) through 4.8 Å (13 wt %) to 5.4 Å (20 wt %) and the hydronium ions (H_3O^+) become farther apart from the sulfonate groups. The water coordination number for water and the water diffusion is enhanced with increasing water content because the internal structure of water phase in S-PEEK approaches that of bulk water. Compared to the Nafion and Dendrion membrane, the S-PEEK membrane shows less internal structure in the water phase and smaller water diffusion, indicating that the S-PEEK has less nanophase-segregation than the Nafion and Dendrion membranes

2-1. Introduction

Perfluorosulfonic acid (PFSA) polymers such as Nafion have remained popular as a polymer electrolyte membrane due to their high proton conductivity and excellent chemical stability. However, they have numerous drawbacks: PFSA-based polymers have high production cost, drastically lose proton conductivity if relative humidity is lowered and they have poor methanol fuel cross-over making them unpractical for direct methanol fuel cell (DMFC). This has stimulated intensive studies in developing non-PFSA-based polymers, especially sulfonated hydrocarbon-based polymers such as sulfonated poly(ether ether ketone), (S-PEEK), sulfonated poly (styrene) (S-PS) and sulfonated poly (benzimidazole) (S-PBI).[52]

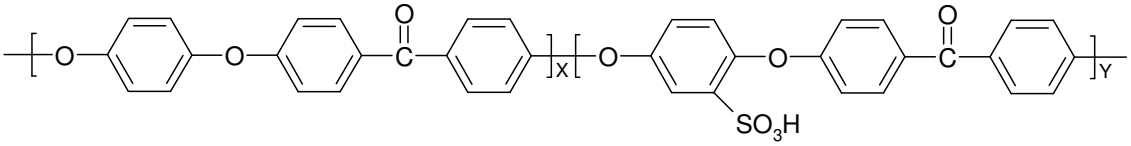

Figure 3: Sulfonated poly(ether ether ketone) (S-PEEK). X and Y are 60 and 40, respectively. The degree of sulfonation (DS) is 40. A random copolymer is used in this study with a degree of randomness (DR) of 1.03..

S-PEEK (Figure 3) is considered a promising candidate for fuel cell applications because it is very chemically stable in the corrosive fuel cell environment, has excellent mechanical properties and is cost effective. The major differences with Nafion are that it is not a perfluorinated polymer and, as Figure 3 shows, that S-PEEK has a its sulfonate group directly attached to the polymer backbone. This is in contrast to Nafion, that has

the sulfonate groups on a side chain. S-PEEK's proton conducting properties were reported by Kobayashi et al.[53] who reported a high proton-conductivity of 10^{-4} – 10^{-2} S/cm at room temperature. This is lower than Nafion that has a proton conductivity of $7.8x10^{-2}$ S/cm.[54] Kreuer found that membranes made of S-PEEK have narrower and less connected hydrophilic channels compared with Nafion, which causes a reduction of the electro-osmotic drag and water permeation in addition to the lower proton conductivity than Nafion.[55] S-PEEK's proton conductivity can be enhanced by constructing a composite membrane with solid heteropolyacids, as Zaidi and his coworkers have observed.[56] Furthermore, S-PEEK's proton conductivity and mechanical strength were shown by Kaliaguine et al.[57] to be affected by the casting solvent. This explains the broad range of experimental data on membrane properties. Xing and coworkers found that the proton conductivity of S-PEEK increases with increasing degree of sulfonation (DS).[58] While the amount of studies on this materials have grown, we still lack knowledge about various properties such as its nanophase-segregated structure, water diffusion and so on. Furthermore, the relationship between the nanophase-segregated structure and the transport properties has not been thoroughly discussed at the molecular level since Kreuer[55] discussed that sulfonated poly ether ketone membrane have a less segregated morphology than the perfluorinated ones.

The fuel cell community has recognized the importance of MD simulations as being useful tools to furnish information on the polymer membrane at different thermodynamic conditions. This mirrors the recent interest in MD studies of polymeric membranes in general, not just for fuel cell use [26-30, 59-69]. Investigations suited for simulation and MD include nanophase-segregation and transport of within hydrated Nafion membranes.

The underpinning physical phenomena of PEM fuel cells can be investigated by taking in experimental results and simulated structures. However, most MD simulation studies have focused on Nafion membrane systems with little serious work done on S-PEEK membranes. This despite that it is a very promising and interesting polymer to study and obtain information on the structure and properties.

Here we discuss the results of our full atomistic MD investigation into hydrated S-PEEK membranes and characterization of the nanophase structure. We focused on the distribution and solvation of the sulfonate groups in water. We compare our results with available S-PEEK experimental results and data in the literature, as well as the results for Nafion.

2-2. Simulation Details

All simulations were carried out using a full atomistic model of S-PEEK. In order to analyze the effect of hydration on the structures and properties of the membrane, various water contents such as 10, 13 and 20 wt % were introduced in the membrane.

2-2.1 Methodology

The simulation used the DREIDING force field and the energy set up as explained in the first chapter. The individual atomic charges of the copolymer were assigned using the

charge equilibration (QEq) method[70] optimized to reproduce the Mulliken charges of small molecules. The atomic charges of water molecule were from the F3C water model.[41]

For this study, the annealing and MD simulations were performed using the MD code LAMMPS (Large-scale Atomic/Molecular Massively Parallel Simulator) from Plimpton at Sandia[47, 48] with modifications to handle our force fields.[26, 34] The equations of motion were integrated using the velocity Verlet algorithm[20] with a time step of 1.0 fs. The Nose-Hoover temperature thermostat[45, 46, 71] for the NVT and NPT MD simulations used a damping relaxation time of 0.1 ps and the dimensionless cell mass factor of 1.0.

2-2.2 Construction and Equilibration of the Amorphous Membrane

The hydrated membrane simulation systems consists of two chains of S-PEEK and the required number of water molecules to obtain 10, 13 and 20 wt % water. This is summarized in Table 1. The degree of polymerization for the S-PEEK chains was set to 100, degree of randomness of 1.03, and the degree of sulfonation set to 40 (Figure 4). The sulfonated monomers were selected randomly from 100 monomeric units in the backbone. All of the sulfonic acid group are assumed to be ionized, this is similar to Jang's previous studies with Nafion.[29, 30] To ensure that this assumption is valid, we used S-PEEK's pKa to calculate the ionization of the sulfonate groups, and therefore limited the water weight to above 10%. Since we are not interested in the crystalline

phase of S-PEEK, the system was built initially with an amorphous structure. This was achieved using Cerius2's amorphous builder, [72] a feature that randomly changes the conformation of the polymer chain and placement of the water molecules. For this procedure the system is placed in a three dimensional periodic box to eliminate the surfaces by creating an infinite bulk.

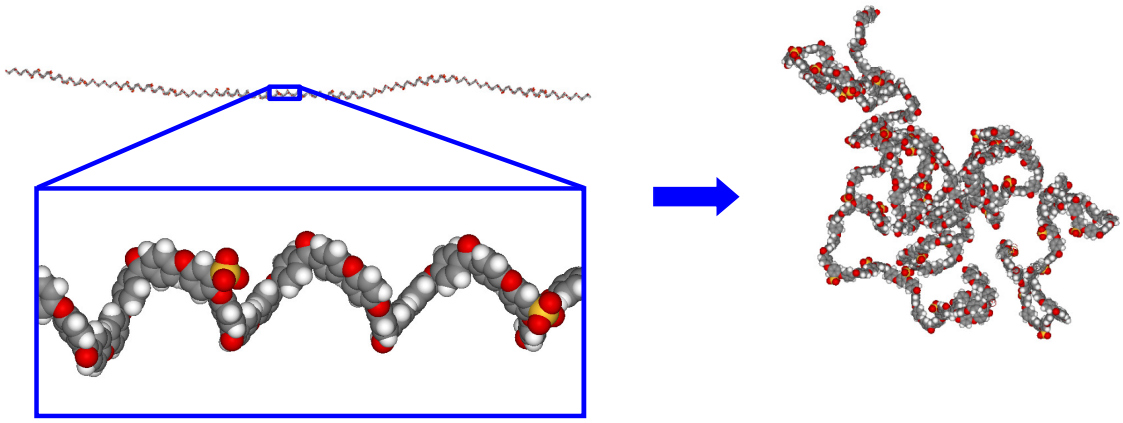

Figure 4: Full atomistic model of the S-PEEK. The conformation in the right-hand side is an equilibrated one selected from the trajectory file of 15 ns NPT MD simulation.

This initial state is very likely unstable, therefore the system should be equilibrated first before analyzing the properties of our interest. However, polymeric systems relax very slowly using standard equilibrium MD. Long relaxation times can make the simulation time impractical. In order to obtain well equilibrated structures of complex amorphous polymers in a reasonable amount of time, we applied the annealing procedure described in previous studies of Nafion and Dendrion membranes. [26, 29, 30] This aids the system to reach a stable equilibrium quickly by driving the system repeatedly through five cycles

of thermal annealing (between 300 and 600 K) and volume annealing (between densities of 0.5 to 1.1 times the expected density). It achieves this by providing excess free volume and kinetic energy, that is, this procedure gives the atoms in the system the space and kinetic energy to escape from various local minima.

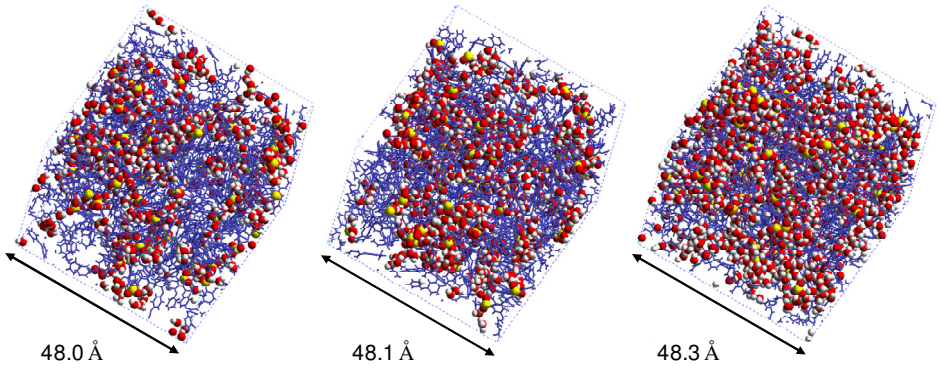

(a) (b) (c)

Figure 5: Nanophase-segregated structures of the hydrated S-PEEK membrane at 353.15 K with various water contents: (a) 10 wt %; (b) 13 wt %; (c) 20 wt %. Blue components denote S-PEEK polymer chain and Yellow balls and attached white balls denote the sulfonate groups. Red and attached white balls are water molecules.

After finishing the *thermal-volume annealing cycles*, a 100ps NVT MD simulation and a subsequent 500ps NPT MD simulation were performed at 353.15 K to finalize the annealing procedure. Then, 15 ns NPT MD simulations were performed at the same temperature to fully equilibrate the structure (). From this, the last 5 ns parts were chosen for the statistical analyses of properties. The equilibrated densities obtained from the simulations are summarized in Table 1.

Table 1: Composition of hydrated S-PEEK membranes and simulation conditions

S-PEEK	Molecular weight	32000	32000	32000
	Equivalent weight	800	800	800
	Degree of polymerization	100	100	100
	Degree of sulfonation (total number of sulfonate group)	40 (80)	40 (80)	40 (80)
	Number of chains	2	2	2
Water content (wt %)		10	13	20
Water volume fraction (%)		6.6	8.7	14.8
Number of water (λ)[a]		395 (4.9)	537 (6.7)	890 (11.1)
Volume ($Å^3$)		110444±487	111261±454	112733±388
Density (g/cm^3)		1.070±0.005	1.100±0.004	1.180±0.004

a λ=*total number of water molecules/number of sulfonate groups*

2-3. Results and Discussion

2-3.1 Sulfonate Groups: Distribution and Solvation

As previous studies have shown,[26, 29, 30] the nanophase-segregation between hydrophobic polymer domain and the water-associated hydrophilic phase is a feature in electrolyte membranes since proton conduction occurs primarily in the water channel. Therefore the size and shape of the water phase will strongly affect the overall electrolyte performance. The water channel is formed around the polymer's sulfonate groups, that is, the resultant nanophase segregated structure is due to the hydrophilic sulfonate groups attached to the hydrophobic backbone. Therefore, we analyzed the spatial distribution of sulfonate group as a function of water content. Figure 6 shows the pair correlation functions for sulfur-sulfur pairs, $\rho g_{s\text{-}s}(r)$. As explained in more detail in Chapter 1, the pair correlation function $\rho g_{s\text{-}s}(r)$ indicates the relative probability (the probability is relative to an infinite separation distance) of finding B atoms at a distance *r* from the A atom, averaged over the equilibrium trajectory as in Equation (2)

$$g_{A-B}(r) = \left(\frac{n_B}{4\pi r^2 \Delta r} \right) \Big/ \left(\frac{N_B}{V} \right) \tag{2}$$

Figure 6, clearly shows that the peak observed for 10 wt % becomes weaker and broadened and the peak position is shifted to further distance with increasing water content (from at ~4.4 Å at 10 wt % through ~4.8 Å at 13 wt % to ~5.4 Å at 20 wt %

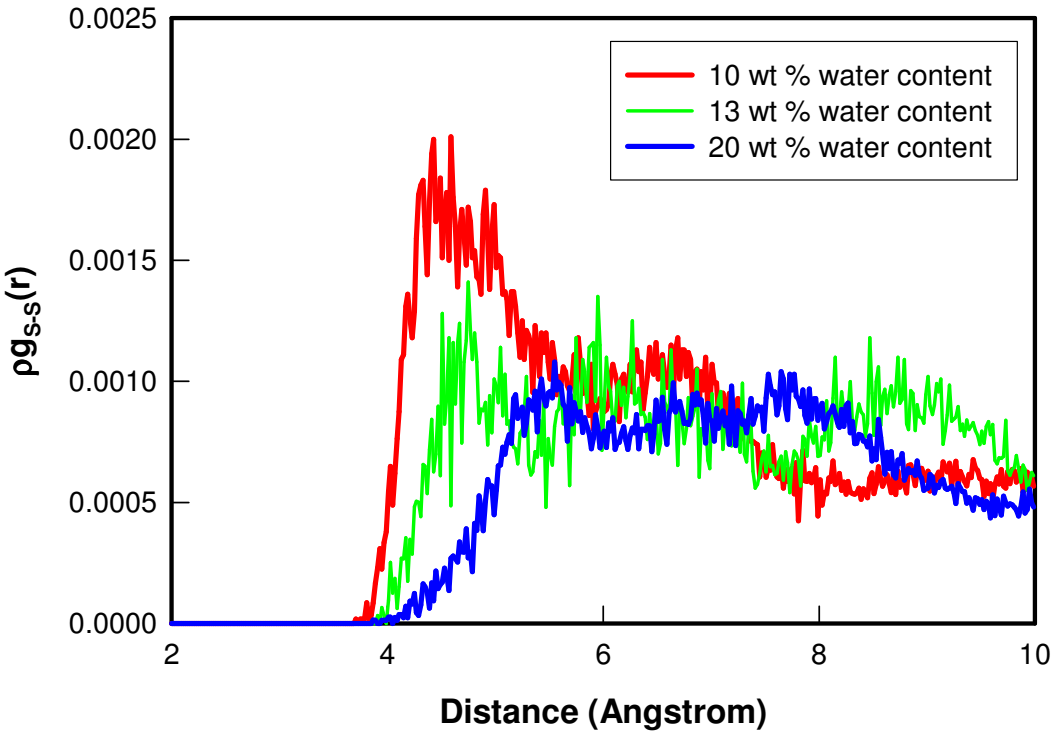

Figure 6: Pair correlation function of sulfur-sulfur, $\rho g_{S-S}(r)$ in the hydrated membranes. ρ indicates the number density of sulfur.

water content). This indicates that the distance between sulfonate groups increases as a function of water content. It is also found that the position of the first peak, that is the most likely distance between nearest neighboring sulfurs, ranges from 4.7 to 6.0 Å for 10 – 20 wt % with water content.

To compare the hydrated S-PEEK membrane with those in Nafion[26] and Dendrion systems [29, 30] hereafter, the RDF is multiplied by the number density ρ. In S-PEEK, increasing the water content causes the S-S distance to increase as well, which is in contrast to Dendrion[30] whose S-S distance is nearly constant regardless of water content. The difference is due to the few covalent bonds separating two sulfurs in the Dendrion system, in contrast to the sulfurs of S-PEEK that are far apart along the PEEK molecule. Because the sulfonate groups of S-PEEK are directly attached to the backbone chain, the reason the first peak position of $\rho g_{s\text{-}s}(r)$ changes, is believed to be swelling-induced conformational changes of the backbone. To verify this, we checked the volume expansion due to the increasing water content. As summarized in Table 1, the volume of the membrane with 13 and 20 wt % increases by 0.7 % and 2 %, respectively, with respect to the 10 wt % membrane. However, such shift of the first peak in Figure 6 (0.4 Å and 1.0 Å for 13 and 20 wt % water content, respectively) is not fully explained by volume expansion alone. This is because the expected contribution from the volume expansion as a function of water content should be just ~0.05 Å and ~0.5 Å on average for 13 and 20 wt % water content respectively. This is assuming that the swelling affects the inter-atomic distance homogeneously throughout the system (~ $\sqrt{\Delta x^2 + \Delta y^2 + \Delta z^2} = \sqrt{3 \times 0.1^2} = \sim 0.05$ Å for 13 wt % water content and $\sqrt{3 \times 0.3^2} = \sim 0.5$ Å for 20 wt % water content where Δx, Δy and Δz are the increment of system size in x, y

and z axis direction as shown in). Therefore, something else is also causing this peak shift. This is the solvation of the sulfonate group by water with increasing water weight percentage. Figure 7 a and b show the pair correlation function for sulfur-oxygen (water) pairs, $\rho g_{s\text{-}o(water)}(r)$ and sulfur-oxygen (hydronium) pairs, $\rho g_{s\text{-}o(hydronium)}(r)$, respectively. The pair correlation function gives us the relative number densities of water or hydronium from a central atom. By integrating the pair correlation function, we can calculate how many water or hydronium surround the sulfonate group. From Figure 7a, it is clear that the intensity of the peaks increase as the water content increases without shifting the location of the peak position. This indicates that the number of water molecules surrounding the sulfonate groups increases with increasing water content. On the other hand, it is observed that, $\rho g_{s\text{-}o(hydronium)}(r)$ peak decreases with increasing water content. This trend is due to the solvation of hydronium as well as the sulfonate ions: more water molecules solvate the hydroniums and sulfonates and thereby the electrostatic interaction between hydronium and sulfonate is screened out by the water molecules.

To quantitatively analyze this, the average number of water and hydronium molecules surrounding each sulfonate group, the coordination number (CN), is obtained by integrating the first peaks of the pair correlation functions. This is summarized in Figure 8 and Table 2; here the water CN for sulfonate increases from 2.8 to 4.6 whereas the hydronium CN for sulfonate decreases from 1.4 to 0.9, as a function of water content.

Table 2: Coordination number (CN) for sulfonate group

Water content (wt %) (λ)	10 (4.9)	13 (6.7)	20 (11.1)
Water CN	2.8	3.6	4.6
Hydronium CN	1.4	1.2	0.9
Total	4.2	4.8	5.5

Through this solvation shell analysis, several additional interesting points are found. First, at lower water contents (10 wt %), the value of the sulfur surrounded by hydronium CN is larger than 1.0. However, in our system there is strictly one hydronium for each sulfonate group. A CN larger than one is possible only when each sulfonate group has an extra hydronium partially shared with a neighboring sulfonate group. The observation of higher hydronium CN at lower water contents is consistent with the close distance between sulfonate groups shown in Figure 6. In other words, at 10 wt % of water content, the sulfonate groups are distributed close to each other and the hydronium molecules are near the sulfonate groups; therefore, one sulfonate group can have more than one hydronium around itself. As water content is increased, the distance between sulfonate groups becomes larger (Figure 6), such that hydronium sharing disappears and the hydronium is more solvated. This causes the hydronium CN to go down with increasing water weight.

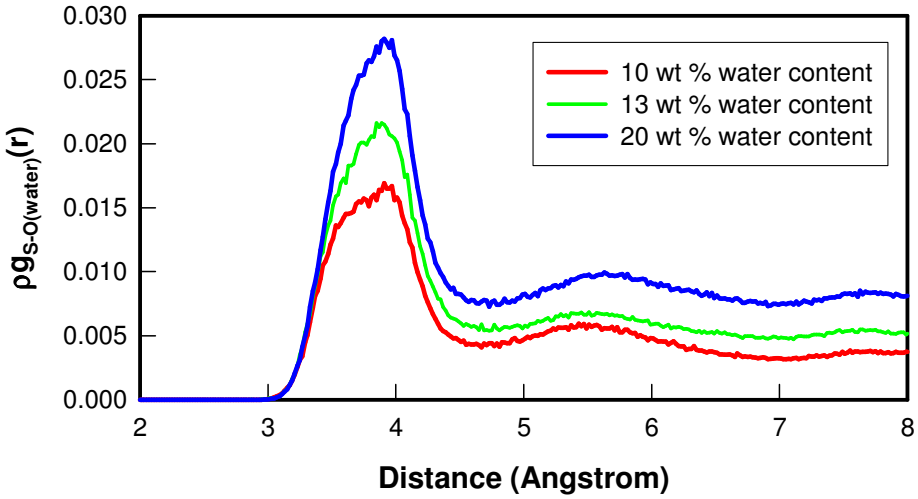

(a)

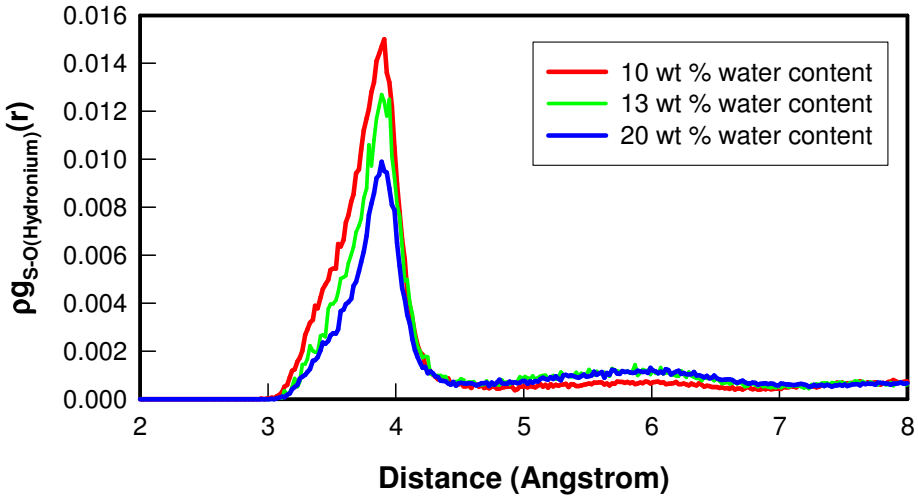

(b)

Figure 7: Pair correlation function of (a) sulfur (sulfonate group)-oxygen (water), $\rho g_{S-O(water)}(r)$ and (b) sulfur (sulfonate group)-oxygen (hydronium), $\rho g_{S-O(hydronium)}(r)$ in the hydrated membranes. ρ indicates the number density of water and hydronium, respectively.

Another point in Table 2 is that for larger water weight, the CN is smaller than the value of λ, the total number of water molecules/number of sulfonate group. While CN is the number of water molecules surrounding a sulfonate group, λ is the ratio of water to sulfonate groups. At lower water content, λ is similar to the CN because relatively small amount of water molecules gather around the hydrophilic sulfonate groups rather than the hydrophobic sites. However, once space surrounding the sulfonate is fully occupied, the excessive water molecules should form their own water phase, therefore, while CN becomes constant, λ becomes larger and larger.

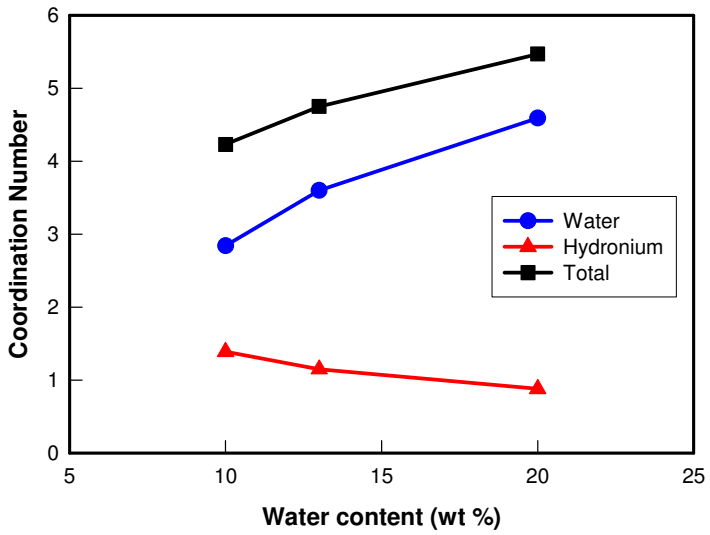

Figure 8: Water coordination number (CN) (blue) and hydronium CN (red) for sulfonate group. The total coordination number is obtained by summing the water CN and the hydronium CN.

2-3.2 Water Phase in the Membrane

The proton conducting channel of the electrolyte membrane is predominantly the water phase, therefore, there are extensive studies on the proton transfer in water[73-81] and in polymer electrolyte membranes. [75-77, 82-85] The general consensus of these studies is that the proton diffusion rate in bulk water is 4~8 times larger than in the hydrated membrane. This is explained by Kreuer[75, 77] and by Paddison,[85] by noting that water's well-organized and compact hydrogen bonding network aids efficient proton hopping, a transport mechanism available due to the proton's small mass. Compared to the bulk water phase, it is known that the water phase in electrolyte membranes has less developed internal structure. The reduced hydrogen bond connectivity, leads to less proton conduction. Therefore, it is very desirable to investigate the internal structure of the water phase in S-PEEK membrane as a function of water content to achieve a quantitative relationship between structure and performance of PEM fuel cell.

We calculated $\rho g_{o(water)\text{-}o(water)}(r)$, as shown in Figure 9, to characterize the internal structure of the water phase in the hydrated membrane. The intensity of the pair correlation increases with increasing water content, as observed in previous simulation studies on Nafion[26] and Dendrion[29, 30].

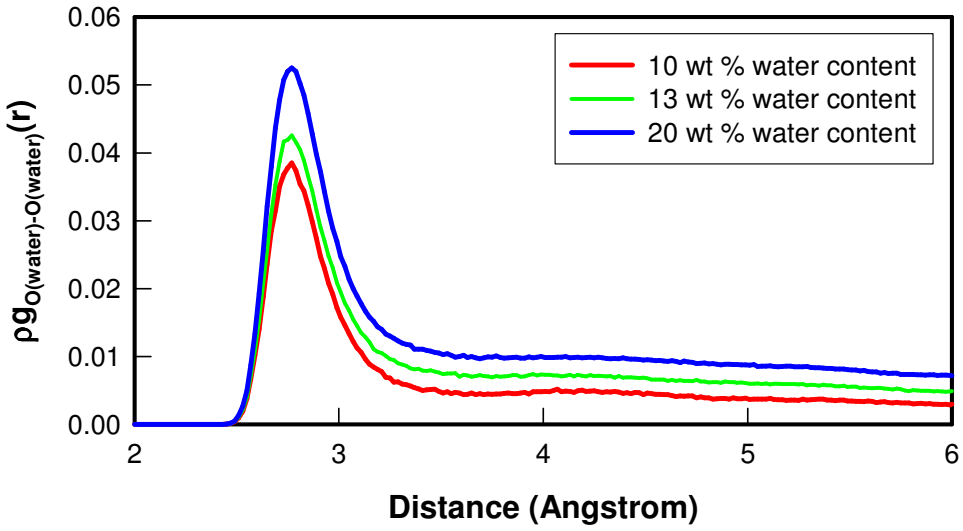

(a)

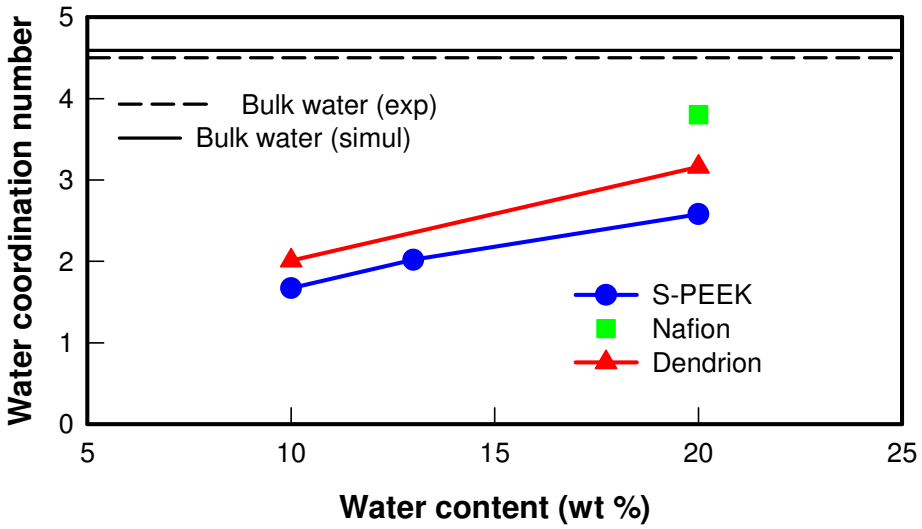

(b)

Figure 9: (a) Pair correlation function of oxygen (water)-oxygen (water), $\rho g_{O(water)-O(water)}(r)$ in the hydrated membranes. ρ indicates the number density of water; (b) Water coordination number of water of S-PEEK in comparison with that of Nafion[26] and Dendrion[30]. The solid and dashed black line is the water coordination number of bulk water from simulation and experiment, respectively [30].

This is because as the water content increases, the structure of the water phase develops more until it reaches the level of bulk water. Similar to our work with the sulfur-oxygen, we calculate the CN of water molecules surrounding each water molecule. Figure 9b shows the change of the water-water CN as a function of water content in comparison with Nafion[26] and Dendrion[29, 30] and bulk water[30, 86]. First, it is found that the water CN increases with increasing water content, since water molecules aggregate to form their own phase and therefore the portion of water molecules surrounded by neighboring water molecules increases.

Another point from Figure 9 is that the CN is larger for the Nafion and Dendrion membrane than for the S-PEEK, for equivalent water content. This indicates that hydrated membranes made of Nafion or Dendrions have a more bulk-like water phase than S-PEEK membranes. This is because the structural development of the water phase within a polymeric membrane is determined by the hydrophobic polymer backbone phase and the hydrophilic water phase being held close together at the nano scale by the sulfonate group. This stark contrast in hydrophobicity creates clearly delineated phases. Nano scale phase segregation occurs because the hydrophobic backbone is trying to expel the water, while the sulfonate group attached to the backbone is trying to attract it. Thus, more nanophase-segregation is achieved using more hydrophobic polymer such as PTFE because more water molecules gather together to form a bulk water-like structure. A less hydrophobic S-PEEK retains relatively more dispersed water in its less nanophase-segregated morphology, because the energy penalty for a water-backbone surface is smaller. This is consistent with the report from Kreuer.[55]

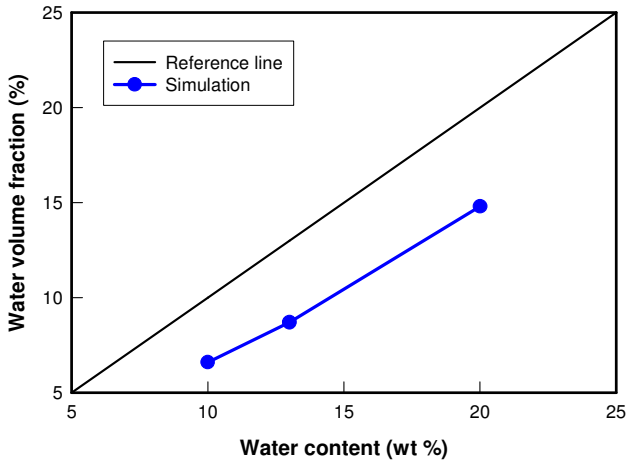

Figure 10: Change of volume fraction of water phase as a function of water content. The reference line is for eye guide whose slope is 1.0, assuming that the weight fraction and the volume fraction has one-to-one correspondence.

The volume fraction of the water phase in the membrane is further evidence of the development of the water phase's structure in the membrane. The volume fraction of the water phase in the membrane was calculated as follows.

$$Volume\ \ fraction\ \ of\ \ water\ (\%) = 100 \times (V_{free,\ no\ water} - V_{free,water}) / V_{total} \tag{3}$$

where $V_{free,\ no\ water}$ and $V_{free,water}$ are the free volumes of the membrane using a 1.4 Å probe radius before and after removing the water molecules, respectively. Figure 10 shows an increase of the volume fraction of the water phase in the membrane as a function of water content. Here it is noticed that the simulation trend in Figure 10 has a smaller slope than the reference line with 1.0 slope. The reference line with 1.0 slope is

the line representing no change in water's molar volume upon mixing. Therefore, it is noticed that there is a change of molar volume upon mixing. Thus, because the observed line has a smaller, but increasing, slope than the reference line, this means that the water phase becomes denser with increasing water content. This is also consistent with the previous analysis for water CN via $\rho g_{O(water)-O(water)}(r)$ that the water phase develops its structure more as the membrane uptakes more water.

Therefore, as the water content in hydrated S-PEEK membrane increases, the internal structure of the water phase becomes similar with that of bulk water, approaching bulk water's CN.

2-3.3 Water Transport

As addressed in previous experimental[55, 77, 87] and simulation studies[26, 29, 30] on transport in nanostructures, it has been found that water diffusion is greater in more phase-segregated structures because the phase-segregated water molecules in membranes achieve more bulk water-like structure. Also, bulk water has a higher proton diffusion rate than water in nanophase-segregated phases, correspondingly proton transport is higher in membranes that achieve more bulk like water. In this study, we investigated the water diffusion with various water contents in the hydrated S-PEEK membrane by comparing with the work done by Kreuer[55] reporting that the diffusion of water is more enhanced in Nafion than in sulfonated PEEK because of the wider water channels in Nafion.

Figure 11 and Table 3 summarize the mean square displacement (MSD) of water calculated from the final 5 ns of the 15 ns trajectories and the corresponding diffusion coefficients (*D*), respectively. The diffusion coefficient was calculated from the linear part of the MSD plot (black colored lines in Figure 11) by assuming that they follow Gaussian diffusion with the following equation as shown in Figure 11a. Figure 12 shows the alpha value of 0.82 for 20wt%, indicating the diffusion is almost Gaussian.

$$D = \lim_{t\to\infty} \frac{1}{6t} \left\langle \left(r(t) - r(0) \right)^2 \right\rangle \tag{4}$$

where r(t) and r(0) are the positions of water at a certain time (t) and at the beginning, respectively. First, as shown in Figure 11a, the diffusion of water is enhanced with increasing water content. This is consistent with previous simulation results with Dendrion and Nafion membranes, therefore we think it is a general feature of hydrated polymeric membranes the water diffusion increase with increasing hydration as the internal structure of water phase becomes more developed at higher water content. Then, we compared the simulated water diffusion coefficients with the available experimental values (Table 3). Although the available experimental S-PEEK data has a higher DS (~70 %) than our simulated one (40 %), this comparison was carried out using a similar water phase volume. For this comparison, we assume that a similar water amount should provide similar conditions.

Table 3: Diffusion coefficients (cm^2/s) of water at T=353.15 K

a. Reference [30, 88-90] b. Reference [55] c. Reference [26] d. Reference [91] e. References [29, 30]

Water content (wt %)	10	13	20
(λ)	(4.9)	(6.7)	(11.1)
Bulk water[a]		5.98×10^{-5} (exp. 6.48×10^{-5})[a]	
S-PEEK	0.07×10^{-5}	0.09×10^{-5} (exp. ~0.01×10^{-5})[b]	0.13×10^{-5} (exp. ~0.2×10^{-5})[b]
Nafion[c]			$1.43\text{-}1.62\times 10^{-5}$ (exp. 1.25×10^{-5})[d]
Dendrion[e]	$0.16\text{-}0.37\times 10^{-5}$		0.57×10^{-5}

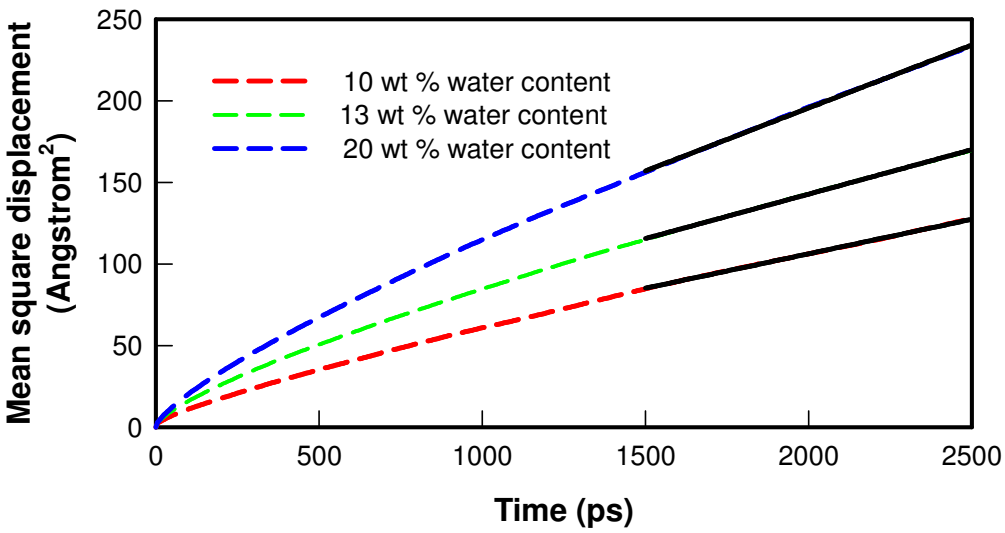

(a)

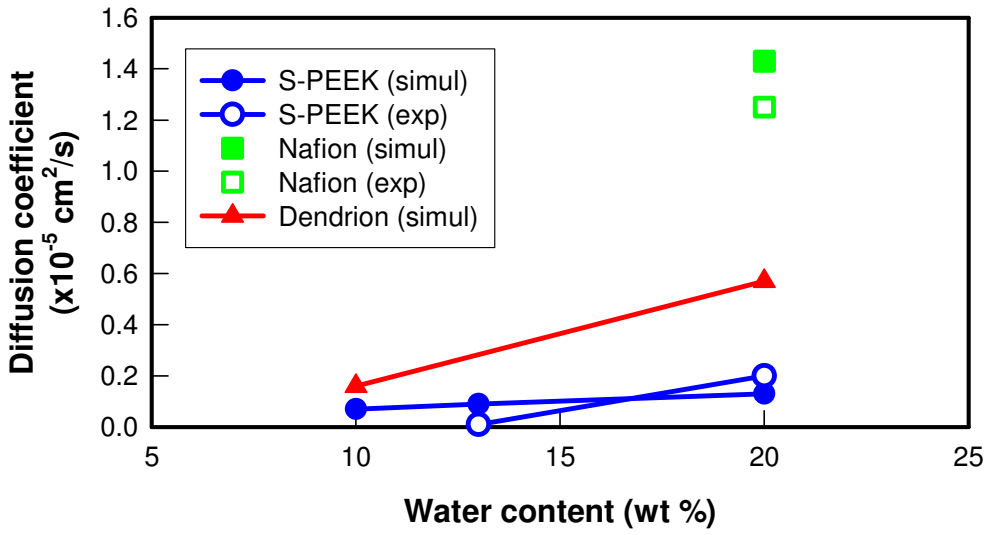

(b)

Figure 11: (a) change of mean square displacement of water as a function of time; (b) Water content dependency of water diffusion coefficients.

Table 3 shows that the simulated diffusion coefficients have the same order of magnitude with the experimental ones, indicating that our simulations described the water diffusion in the hydrated S-PEEK membrane well. However, it is observed that at lower water contents, the simulated value is nine times larger than the experimental value, whereas the values are in much better agreement for 20wt%. The reason for this could be that our simulation does not allow for bond breaking. However it is widely known that hydronium in water is in a dynamic equilibrium, with the proton hopping from one water molecule to the next or even, temporarily, to the sulfonate ion. At low levels of hydration, a given water molecule will spend more time as a hydronium ion and therefore attracted, or trapped, to the sulfonate ion. At high levels of hydration this effect would not be as significant.

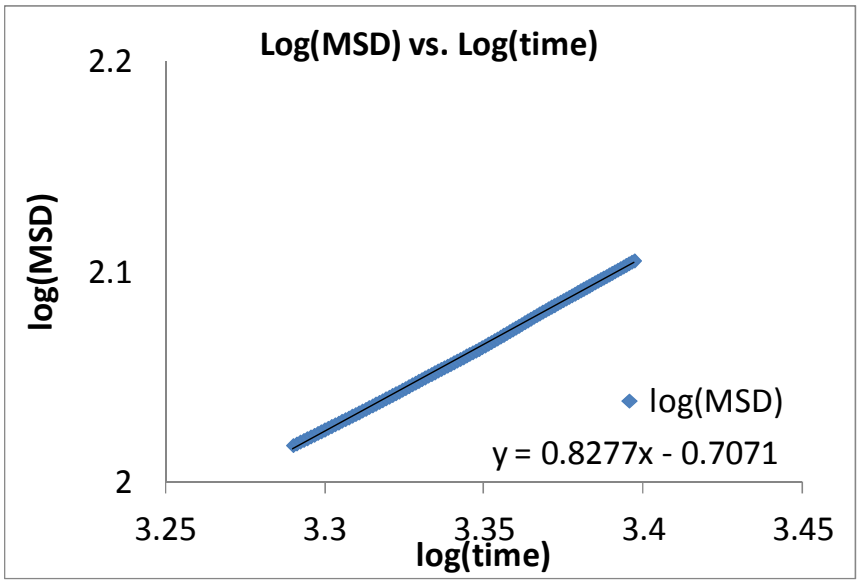

Figure 12: Log(MSD) vs. log(time) with a trendline showing the near Gaussian diffusion of our system.

Next, the water diffusion in the S-PEEK membrane is compared to the Nafion and the Dendrion membranes. It is clearly observed in Figure 11b that the simulated water diffusion coefficient in S-PEEK is smaller than that in the Nafion or Dendrion membrane at 20 wt % of water content. Especially, the water diffusion coefficient of the S-PEEK is smaller by one order of magnitude than the Nafion membrane. Since water diffusion is facilitated by a more nanophase-segregated structure, our diffusion coefficient is consistent with a picture of a more nanophase-segregated morphology between the water phase and the polymer phase in Nafion and the Dendrion membrane.

2-4. Conclusion

Using a full atomistic simulation, we investigated the S-PEEK (40 % of DS) with various water contents (10, 13 and 20 wt %) at 353.15 K. The equilibrated morphology of hydrated S-PEEK membrane was obtained through 15 ns NPT MD simulation after annealing simulations.

In order to characterize the nanostructure of such hydrated S-PEEK membranes, first, we calculated the pair correlation function for sulfur-sulfur pairs, $\rho g_{s\text{-}s}(r)$, showing that the position of the first peak is shifted from 4.4 Å at 10 wt % water content through 4.8 Å at 13 wt % to 5.4 Å at 20 wt % of water content, respectively. This result indicates that the sulfur-sulfur distance increases with increasing water content. By investigating the pair correlation function of sulfur-oxygen (water), $\rho g_{S-O(water)}(r)$, it was found that such

increase of sulfur-sulfur distance is due to the solvation of sulfonate group by water molecules as well as the volume expansion due to the hydration.

In addition, analyzing $\rho g_{S-O(water)}(r)$ and $\rho g_{S-O(hydronium)}(r)$, it is found that the water coordination number of sulfonate is increased from 2.8 to 4.6 with increasing water content, whereas the coordination number of hydronium for sulfonate decreased from 1.4 to 0.9. From these results, it is thought that the sulfonate groups and the hydroniums are solvated more by adding more water and thereby the distance between sulfonates groups is increased, making the number of partially shared hydronium smaller.

The $\rho g_{O(water)-O(water)}(r)$ was also analyzed as a function of water content, showing that the water coordination number for water increases with increasing water content. We think this is evidence that the water molecules form water phase instead of being spread though the membrane as the water content is increased. Thus, the structure of such water phase seems to approach the bulk-water like structure with more water. On the other hand, compared to the Nafion and Dendrion, it is found that the S-PEEK has less developed internal structure in the water phase, which is consistent with the previous study finding that the structural development in water phase depends on the nanophase-segregation.

The water diffusion coefficients were calculated from the final 5 ns part out of the 15 ns NPT MD simulations. It is found that the water diffusion is enhanced with increasing water content, which was consistently observed in the simulation study of hydrated Dendrion membranes.[29, 30] Besides, through comparing with Nafion[26, 29, 30] and Dendrion,[29, 30] the observation that the water diffusion coefficient in the hydrated S-PEEK is smaller than in the hydrated Nafion and Dendrion membrane, implying that the

nanophase-segregation in the hydrated S-PEEK membrane is less than in the Nafion and Dendrion membrane.

Chapter III

Effect of Water Weight and Temperature on the Structure and Water Transport of Hydrated Sulfonated Poly (Ether Ether Ketone)

The work presented here was published by the author in the Journal of Renewable and Sustainable Energy. [92]

Whereas in the previous chapter we were concerned with the effect of water content, in this chapter we discuss hydrated S-PEEK at various temperatures for 10 and 20 wt% water. Thus, we characterize the nanophase-segregated structures of the hydrated S-PEEK and its water transport property as a function of temperature by looking only at two water contents.

The effects of temperature on hydrated sulfonated poly(ether ether ketone) is studied using molecular dynamics. Three different temperature conditions (298K.15 K, 323.15 K, and 353.15 K) with two different water contents (10 wt % and 20 wt %) are simulated. Analyzing the pair correlation functions, it is found that there is limited temperature effects on the distribution and solvation of the sulfonate groups. The structure factor analysis shows that the temperature dependence of the nanophase-segregated morphology is not significant in the simulated temperature range. On the contrary, the structure factors $S(q)$ at ~30Å (q = ~0.2 $Å^{-1}$) and ~13Å (q = ~0.5 $Å^{-1}$) clearly increase, with water content indicating that the development of water channels is mostly affected by the water content. Within the water phase in the nanophase-segregated structure, the internal structure of water phase becomes more developed with decreasing temperature and

increasing water content. By analyzing the mean square displacement of the water molecules, it is also found that water's self diffusion is enhanced with increasing temperature. We observation that the activation energies calculated from such temperature dependency are very similar (E_a=25.7 kJ/mol and E_a=24.9 kJ/mol for 10 wt % and 20 wt %, respectively), displaying little water weight dependency. Compared to the bulk water (13.2 kJ/mol) and the water in Nafion (16.7-18.9 kJ/mol), S-PEEK's higher activation energy confirms that more nanophase-segregation enhances water transport through the membrane.

3-1. Introduction

In the field of polymer electrolyte membranes fuel cells (PEMFCs), the most popular polymeric material has been perfluorosulfonic acid (PFSA) polymers. Their advantages include good proton conductivity and excellent chemical stability.[93-97] However, they have significant drawbacks as well, such as high cost, unsuitability for direct methanol fuel cells and their drastic reduction of proton conductivity with dehydration. To overcome these obstacles in PEMFCs, lots of studies have been devoted to develop non-PFSA membrane materials, especially sulfonated hydrocarbon polymers.[52] The choice of polymer is very important since it determines the chemical resistance, and, through the resulting microstructure, the transport properties.[6, 98]

Amongst the candidate materials currently under investigation, attention to sulfonated poly (ether ether ketone), S-PEEK (**Figure 3**) has increased because of its several

advantages such as cost effectiveness, good mechanical properties and high thermo-oxidative stability. Here we point out from Figure 1 that S-PEEK has the sulfonate groups directly attached to the backbone compared to Nafion that has the sulfonate groups on its side chains. This is believed to be a key feature that determines the properties of S-PEEK, particularly its nanophase segregation. In addition to the chain rigidity of S-PEEK from the aromaticity of the chain backbone, such direct attachment of the sulfonate group onto the chain backbone results in a very distinct nanophase-segregation as reported in our previous study.[51]

In hydrated S-PEEK, two phases are developed – a hydrophobic and a hydrophilic phase. The polymer backbone is more likely to be in the hydrophobic phase, and water molecules and charged species in the hydrophilic one. The hydrophilic phase is not a large featureless region but rather a set of water-rich clusters connected together by smaller water-rich channels[55]. Therefore, added water will preferentially join the hydrophilic phase increasing the phase's concentration of water. Therefore we distinguish a well developed water phase from a less developed one by characterizing how closely the water molecules are packed in the hydrophilic phase, which should be directly related to the hydrogen bonding network. Therefore, we distinguish between S-PEEK and Nafion. Nafion has large water clusters with larger water channels, whereas S-PEEK (and similar polymers) have smaller ones that are not connected as well as the ones in Nafion.[55]

Kreuer found that a membrane made of S-PEEK has narrower and less connected hydrophilic channels compared with that of Nafion, which causes lower proton conductivity, but also a reduction of the electro-osmotic drag and S-PEEK's water

permeation compared to Nafion;[55] electroosmotic drag depends on the channel size, and also channel roughness, as reported by Liu et al[99]. In such a structure, Kobayashi[53] reported that S-PEEK can have high proton-conductivity of 10^{-4} – 10^{-2} S/cm at room temperature. Zaidi and his co-workers have observed an enhancement of proton conductivity from the composite membrane consisting of S-PEEK and solid heteropolyacids.[56] Recently, Kaliaguine et al.[57] reported that the proton conductivity and mechanical strength of S-PEEK membranes are affected by the casting solvent, which explains the reason for the broad range of experimental data on the membrane properties. This is important to keep in mind when comparing to simulation data. Xing and co-workers found that the proton conductivity of S-PEEK is increased with increasing degree of sulfonation (DS).[58]

Although increasing amount of attention is being paid to this material, and other aromatic backbone polymers[98, 100, 101], we still lack an atomistic level knowledge from simulation about its various properties such as its nanophase-segregated structure and water transport properties. Furthermore, the relationship between the nanophase-segregated structure and transport properties has not been thoroughly discussed at the molecular level since Kreuer[55] discussed that the S-PEEK membrane has less segregated morphology than Nafion.

In this context, molecular dynamics (MD) simulation techniques can provide detailed information on polymer membranes at the molecular level under various thermodynamic conditions. Indeed, a large amount of MD studies on materials for use in polymer membrane fuel cells have been published recently.[26-30, 59-69, 102] Such MD simulation techniques have been used successfully to investigate hydrated Nafion

membranes, especially focusing on nanophase-segregation and transport properties, and thus the simulated structures and properties have been widely taken into account to understand the underpinning physics of PEM fuel cells in collaboration with experimental observations. It should be noticed, however, that most of the MD simulation studies have been on the Nafion membrane system; by comparison few simulation studies have focused on S-PEEK, notably my previous study on the effect of water weight on S-PEEK using atomistic molecular dynamics and Mahajan et al. who studied the effect of different solvents, in the study they found that SPEEK was more rigid than Nafion resulting in less nanophase segregation[103, 104]. Also Lins et al. used classical MD to simulate phenylated sulfonated poly(ether ether ketone ketone) (S-PEEKK) at different water weights, λ. Using the pair correlation function they found that the number of hydrogen bonds the sulfonate is involved with depends on water content, but the average lifetime of the hydrogen bonds does not. They also found that water and ion diffusion dependance is lower than Nafion, except when the water content is higher than 25 water molecules per sulfonate ion.[105] Finally Tocci et al. simulated modified PEEK (PEEK-WC) using MD in conjunction with transition state theory to create a new simulation protocol that minimizes the scatter in the calculated diffusion coefficients.[106]

3-2. Computational Models and Simulations

Our simulations are full atomistic simulations. We studied two water contents and three temperatures for 10 wt % and 20 w % water content.

3-2.1 Force Field and Simulation Parameters

Our simulations in this chapter used the same simulation settings as in the previous chapter and the forcefields outlined in Chapter one. This time, however, we simulated the system at various temperatures, 298.15, 323.15 and 353.15K, at 10 and 20 wt% water content. We did not include the 13 wt% since it would require additional computation time and most of the analysis on the effect of water weight were covered in Chapter two.

3-2.2 Construction and Equilibration of the Amorphous Membrane

As summarized in , the simulated hydrated membrane systems consist of two chains of S-PEEK and water molecules for 10 and 20 wt % in a cubic simulation cell with the cell dimension of 47~49 Å. The actual dimension of the simulation cell fluctuates during NPT ensemble simulations due to thermal fluctuation. The contents of the system were the same as in the previous chapter to better compare results.

Table 4: Density (g/cm^3) of hydrated S-PEEK for the various temperatures and water contents. The uncertainties are calculated as the standard deviation of the quantities.

	Water content (wt %)			
	10		**20**	
Temperature(K)	**Density (g/cm^3)**	**Cell length (Å)**	**Density (g/cm^3)**	**Cell length (Å)**
298.15	1.097±0.0032	47.58	1.214±0.0037	47.83
323.15	1.094±0.0038	47.64	1.207±0.0038	47.93
353.15	1.070±0.0047	47.98	1.179±0.0041	48.31

3-3. Results and Discussion

3-3.1 Distribution and Solvation of Sulfonate Groups

In previous studies on Nafion and Dendrion[26, 29, 30] it was noticed that it is desirable that the water phase is well developed via nanophase-segregation since the proton transport takes place in the water phase. In nanophase-segregation, the strong hydrophilic sulfonate groups are solvated by the water molecules and are therefore in the water phase. Therefore, it is important to investigate the spatial distribution of the sulfonate groups under operating conditions, in order to understand the formation of the water phase. In

this section, we discuss the temperature dependency of the sulfonate distribution for 10 wt % and 20 wt % of water contents.

Figure 13 shows the pair correlation functions for sulfur-sulfur pairs, $\rho g_{s\text{-}s}(r)$ (again the radial distribution is multiplied by the number density ρ for direct comparison). First, it is found that $\rho g_{s\text{-}s}(r)$ does not change significantly as a function of temperature. This is consistent with the calculated thermal expansion coefficient of the simulated S-PEEK systems, as reported in Table 4. Therefore, we find just a small change in $\rho g_{s\text{-}s}(r)$. This is consistent with the fact that PEEK has excellent thermal stability as well as rigidity. Our coefficient of (volume) thermal expansion is $4x10^{-4}$/K and $5x10^{-4}$/K for the 10 and 20wt% respectively, compared to the non-sulfonated PEEK's CTE of $1.4x10^{-4}$ /K[107]. Therefore, increasing water content increases the CTE.

In contrast, as discussed in the previous chapter, the effect of water content on $\rho g_{s\text{-}s}(r)$ is clearly observed by comparing Figure 13a and Figure 13b. From our previous study on the hydrated S-PEEK,[51] this result was attributed that, in S-PEEK, the sulfonate groups are directly attached to the PEEK backbone chain. In other words, to accommodate a change in water content, S-PEEK backbone chains need to drastically change their conformations, while Nafion can just adjust the conformations of its side chains.

The trend observed in the distribution of the sulfonate groups is found in the solvation of the sulfonate ion by water molecules. As shown in Figure 14, the temperature dependency of the sulfur (sulfonate) - oxygen (water) pair correlation, $\rho g_{s\text{-}s}(r)$ is not significant, whereas the effect of water content is very clear. Thus, in this temperature range, the solvation of the sulfonate group is almost constant for a given water content.

The pair correlation of the sulfur (sulfonate) - oxygen (hydronium), $\rho g_{s\text{-}o(hydronium)}(r)$ is also shown in Figure 15. Again, only the water content affects the correlation between the sulfonate and hydronium ions.

3-3.2 Nanophase-Segregation: Structure Factor Analysis

It is anticipated that, in the presence of water molecules, S-PEEKs hydrophobic backbone with randomly attached hydrophilic sulfonate groups generates a unique nanophase-segregated morphology. Thus, in this study, we calculated the structure factor, $S(q)$, as outlined in Chapter 1. Our group has used it in previous studies to investigate the phase-segregation of hydrated membranes of Nafion[26] and Dendrion.[29, 30] These previous studies of Nafion [26] led to the discovery of a characteristic dimension of nanophase-segregation of 30 Å - 50 Å. Similar studies for the hydrated Dendrion membrane[29, 30] led to ~20 Å - 40 Å. We calculated the structure factor profiles as a function of scattering vector, q (Figure 16) for the hydrated S-PEEK membranes. In agreement with the discussion about the distribution and solvation of the sulfonate groups, we note that the nanophase-segregated morphology does not significantly change over the simulated temperature range.

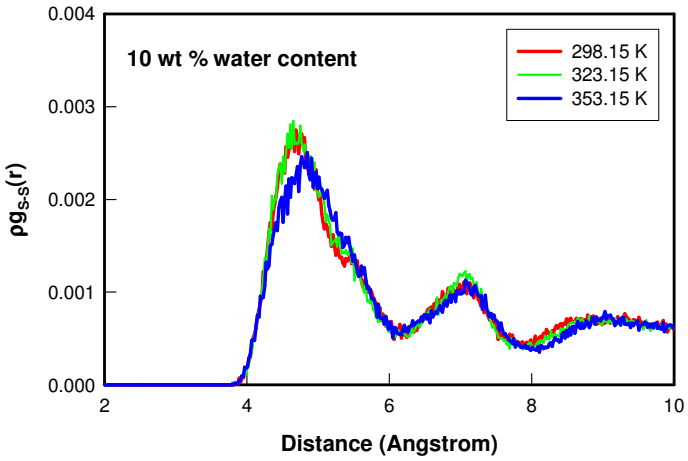

(a)

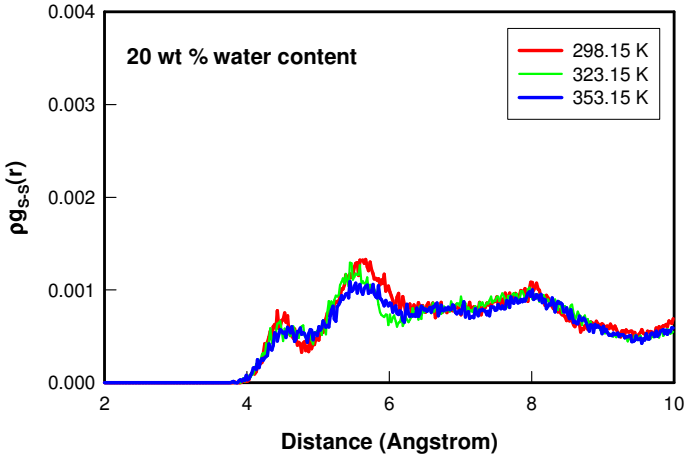

(b)

Figure 13: Pair correlation function of sulfur (sulfonate group) – sulfur (sulfonate group), $\rho g_{S-S}(r)$ in the hydrated membranes with (a) 10 wt % water content and (b) 20 wt % water content. ρ indicates the number density of sulfur.

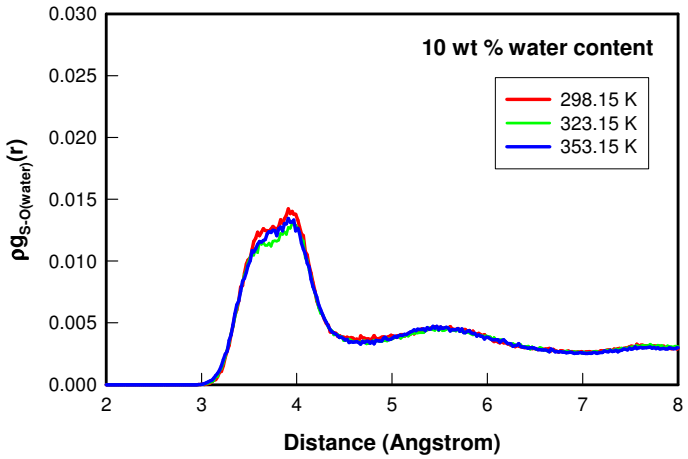

(a)

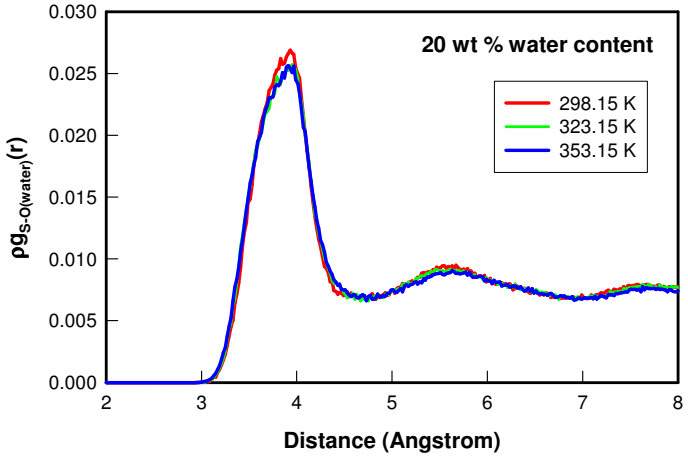

(b)

Figure 14: Pair correlation function of sulfur (sulfonate group) - oxygen (water), $\rho g_{S-O(water)}(r)$ in the hydrated membranes with (a) 10 wt % water content and (b) 20 wt % water content. ρ indicates the number density of water.

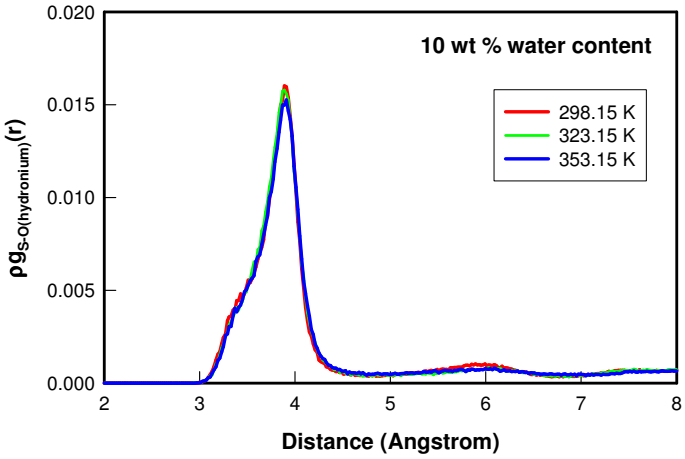

(a)

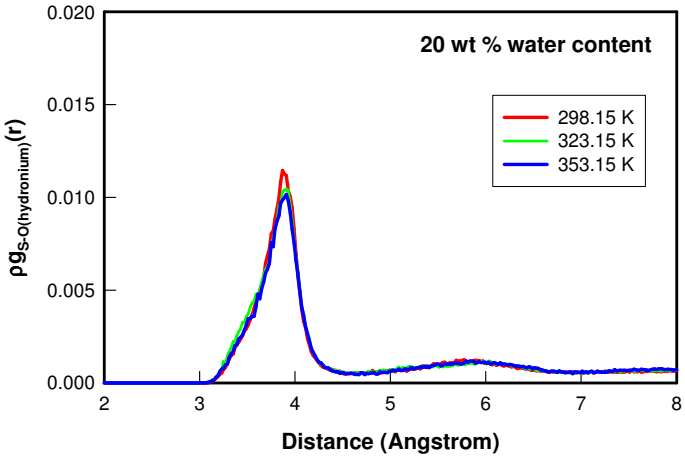

(b)

Figure 15: Pair correlation function of sulfur (sulfonate group) - oxygen (hydronium), $\rho g_{S-O(hydronium)}(r)$ in the hydrated membranes with (a) 10 wt % water content and (b) 20 wt % water content. ρ indicates the number density of hydronium.

On the other hand there is a clear dependence on water content on the structure factor: the intensity of $S(q)$ with 20 wt % water content is larger than that with 10 wt %. This implies that the contrast in concentration between the hydrophilic and the hydrophobic phases becomes larger with increasing water content. The hydrophobic phase is the S-PEEK backbone, therefore the backbone is more clearly segregated from the sulfonate and water. Both water contents' peaks are at similar peak positions, indicating that the characteristic dimensions of the nanophase-segregated morphologies are similar: the first peak at q = ~0.2 $Å^{-1}$ corresponds to ~30 Å and the second peak at q = ~0.5 $Å^{-1}$ corresponds to ~13 Å.

This implies that, instead of creating new features increased water reinforces existing features; the water phase develops from existing available sites, especially around the sulfonate groups. That is why the main characteristic dimension is similar regardless of the water contents. In addition, it should be noted from Figure 16 that the intensity of the second peak at q = ~0.5 $Å^{-}$ is more developed compared to the intensities of the first peak at q = ~0.2 $Å^{-1}$ for 10 wt % water content (Figure 16a). Therefore, a structure with a characteristic dimension of ~13 Å develops with increasing water content.

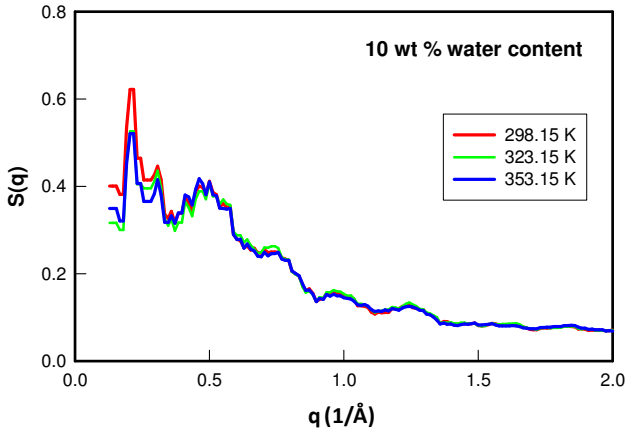

(a)

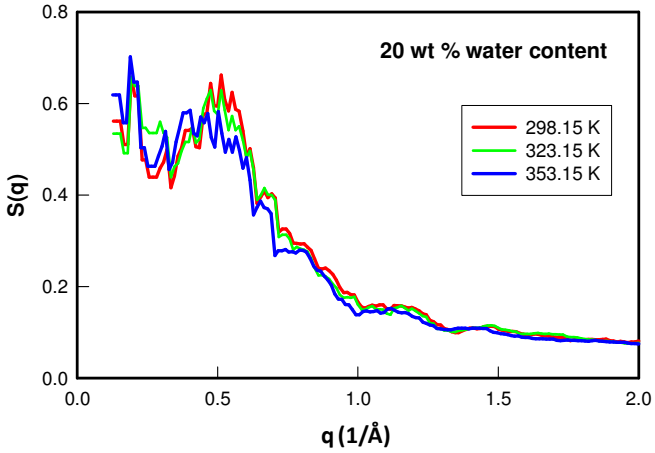

(b)

Figure 16: Structure factor profile with (a) 10 wt % water content and (b) 20 wt % water content.

Another point we need to stress here is the finite size effect. As shown in Table 4, the dimension of the simulation cell is 47-49 Å under various temperature conditions. Such dimension is just larger than the characteristic dimension of the simulated nanophase-segregation in the system. Considering the dimension of the simulation cell affects the density correlation of the system, it should be desirable that the dimension of the simulation cell is at least two times larger than the anticipated dimension of the simulated phase. However, this requires 8 times more atoms. Thus, it is very likely that the characteristic correlation length in our simulation is influenced by the finite size of the simulation cell. Therefore, it should be noted that we focus on the difference between the 10 wt % and the 20 wt % of water content rather than the absolute value of correlation lengths.

3-3.3 Internal Structure of Water Phase in Membrane

Transport properties of water and protons in the hydrated membranes depends on the shape, size and connectivity of the water channels. However, as noted in previous studies, [29, 30, 51] the transport properties also depends on the internal structure of the water; that is the position and orientation of the water molecules with each other. Therefore, transport properties should depend, not only on the larger scale structure of the phases but also on the atomic scale structure. Thus, we investigated the internal structure of the water phase, focusing on the water weight and temperature effect, by focusing on the water molecule's solvation shell and pair correlation function.

Figure 17 presents the pair correlation function of oxygen (water) - oxygen (water), $\rho g_{o(water)\text{-}o(water)}(r)$. Unlike the pair correlation functions of the sulfonate ion, the internal structure of the water phase is clearly dependent on the temperature, as well as water content.

First, the effect of changes in $\rho g_{o(water)\text{-}o(water)}(r)$ with water content is consistent with the observations of the structure factor in the previous section: as the membrane retains more water molecules, the water molecules themselves are more packed. Second, with increasing temperature, the intensity of the main peak (at ~2.7 Å) decreases, while the intensity of the trough (around ~3.5 Å) increases. Furthermore, the second solvation shell (~4.0 Å) becomes indistinct with increasing temperature. The loss of features in the pair correlation indicates that the water phase in the membrane looses the hydrogen-bond-mediated internal structure with increasing temperature.

To compare the internal structure of the water phase of S-PEEK with those of other polymeric membranes, we calculated the water coordination number (Table 5) by integrating the first solvation shell observed in Figure 17. The CN calculation shows that the overall packing of water molecules increases with increasing water content or decreasing temperature (with the exception of CN at 323.15 K). Compared to other polymeric membranes, such as Nafion and Dendrion, the CN of S-PEEK is lower, which indicates that the water molecules of S-PEEK are less packed than Nafion or Dendrion.

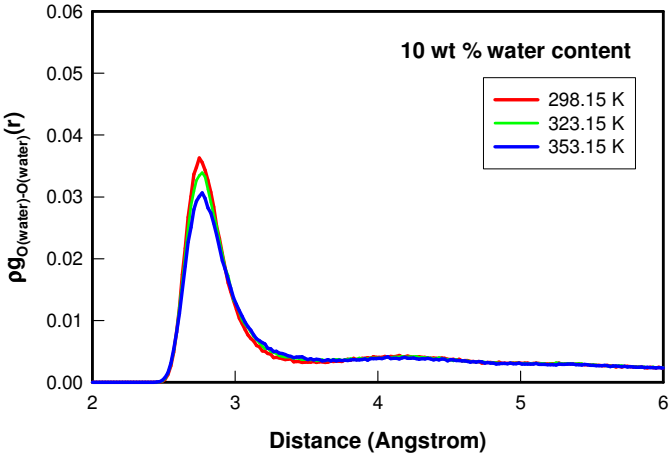

(a)

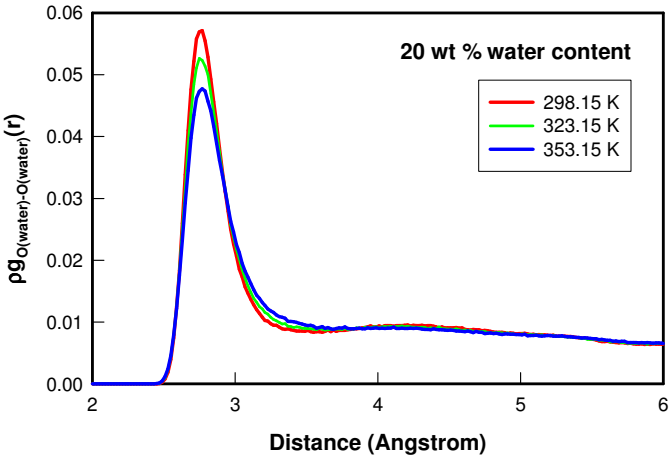

(b)

Figure 17: Pair correlation function of oxygen (water) - oxygen (water), $\rho g_{O(water)-O(water)}(r)$ in the hydrated membranes with (a) 10 wt % water content and (b) 20 wt % water content. ρ indicates the number density of water.

Table 5: Water coordination number (CN) for H_2O

		S-PEEK		Bulk Water*	Nafion[29]	Dendrion[30]	
Water Content (wt %)		**10**	**20**		**20**	**10**	**20**
	298.15	1.37	2.38	4.41			
T (K)	**323.15**	1.38	2.37	4.36			
	353.15	1.33	2.35	4.28	3.8	2.01	3.16

*CN = 4.5 from experiment [86]

This is due to the less pronounced nanophase-segregation in S-PEEK membranes. This is because, at a given water content, the water phase in a membrane material with a more hydrophobic backbone is more bulk like. Considering that hydrocarbon materials are less hydrophobic than fluorocarbon materials, our finding that S-PEEK's water phase is less structured than Nafion's or Dendrion's is consistent with the expectation that a less hydrophobicity polymer has less pronounced nanophase segregation. For comparison we've included the CN of bulk water simulated at the same temperatures as our S-PEEK systems. We note that S-PEEK and water's CN follow the same decreasing trend.

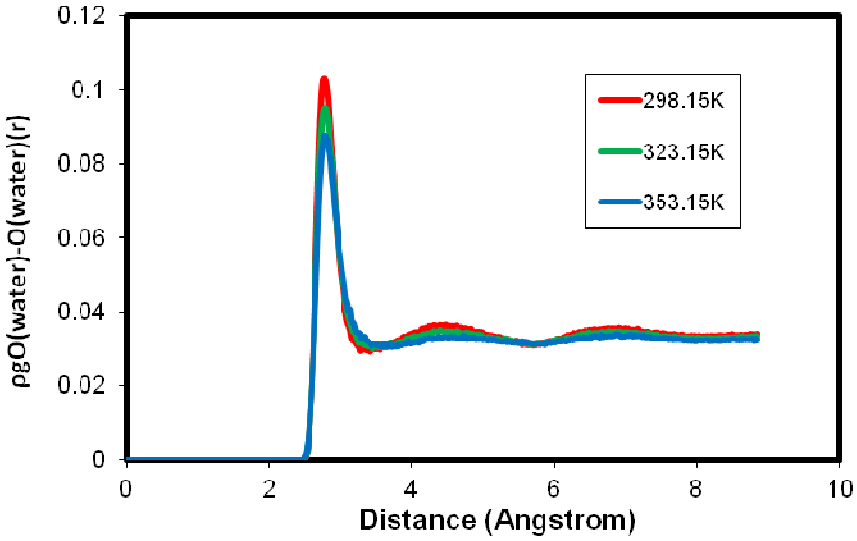

Figure 18: Pair correlation function of oxygen (water) - oxygen (water), $\rho g_{O(water)-O(water)}(r)$ for bulk water at different temperatures.

3-3.4 Water Transport

In previous experimental[55, 77, 87, 98] and simulation studies[26, 29, 30] on transport through nanophase-segregated structures, it was found that the diffusion of water is greater in more phase-segregated water phases that achieve a more bulk-water-like internal structure. In this section, the water diffusion in the hydrated S-PEEK membrane at various temperatures was investigated by comparing it with the work done by Kreuer[55] who reported that the diffusion of water is greater in Nafion than in sulfonated PEEK because of the wider water channels in Nafion.

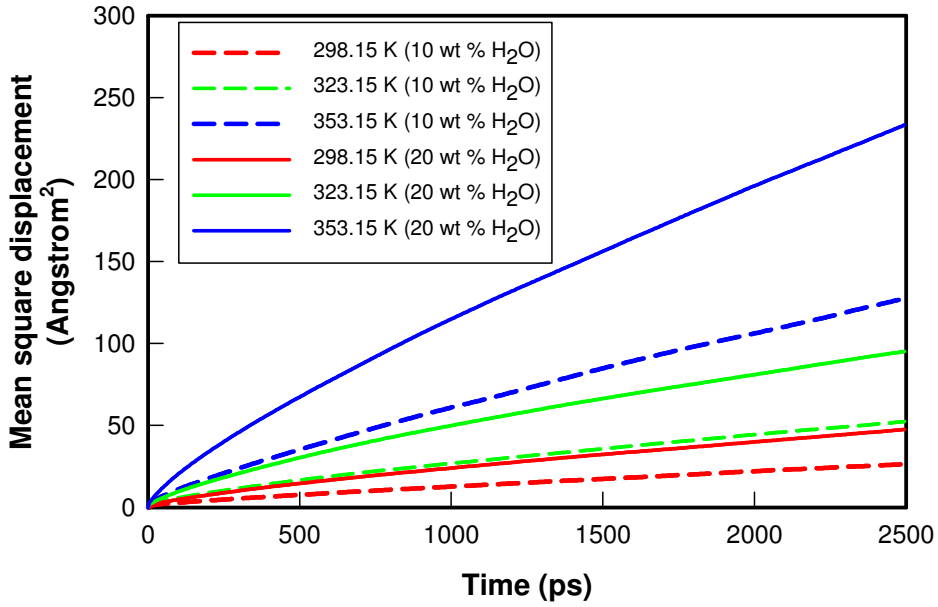

Figure 19: Change of mean square displacement of water as a function of time. The linear part of the graph, is used to extract the diffusion coefficient. See previous chapter for more details on extracting the diffusion from the MSD.

Figure 19 shows the monotonic increase of the mean square displacement (MSD), $\langle (r(t)-r(0))^2 \rangle$ as the simulation temperature water content is increased. The effect of water content is clearly observed. For any given temperature condition, the MSD of water in the 20 wt % water content is larger than that in the 10 wt % water content system. As summarized in Table **6** the water diffusion coefficient (D) is calculated from the MSD in Figure 19. Therefore, based on the change of D as a function of temperature, we calculated the activation energy (E_a) of water diffusion using the Arrhenius equation:

$$D = D_0 \exp(-E_a / RT) \tag{6}$$

where R is the gas constant, T is a absolute temperature and D_0 is a constant. E_a is calculated as 25.7 kJ/mol for the 10 wt % water content and 24.9 kJ/mol for the 20 wt % water content. Although E_a decreases with increasing water content, the reduction as a function of water content is not very significant. Similar activation energy for 10 wt % and 20 wt % of water content, and a nearly proportional diffusion rate with water content, suggests that the diffusion mechanism is not changed significantly and instead the diffusion coefficient is higher due to larger volume fraction available at higher water contents. We note in Figure 16 that the structure factor is more developed at ~13 Å. In other words, the water diffusion through the hydrated S-PEEK in our study is enhanced but by the more developed water channels in the nanophase-segregated morphology. Another point to note is that E_a for water diffusion in S-PEEK is larger than the activation energy for bulk water (13.2 kJ/mol) and for water in Nafion (16.7-18.9 kJ/mol). This indicates that water diffusion in S-PEEK needs more kinetic energy than in Nafion and bulk water. Again, this is consistent with our understanding of the relationship between water diffusion and the structure of water.[30]

Table 6: Diffusion coefficients (cm^2/s) of water
a. Reference [30, 88-90] b. Reference [55] c. Reference [26] d. Reference [91] e. References [29, 30] f. References [91, 95]

	Water content (wt %)	**Diffusion Coefficient ($\times 10^{-5}$ cm^2/s)**			**Activation Energy (kJ/mol) (E_a)**
		T=298.15 K	**T=323.15 K**	**T =353.15 K**	
Bulk water		2.69 [c] (exp. 2.30)[a]		5.98 [c] (exp. 6.48)[a]	13.2 (exp. 17.6-19.7)[a]
S-PEEK	**10**	0.015	0.028	0.074	25.7
	20	0.026	0.050	0.125 (exp. ~0.2)[b]	24.9
Nafion[c]	**20**	0.458-0.59 (exp. 0.5)[d]		1.43-1.62 (exp. 1.25)[d]	16.7-18.9 (exp. 11.6-0 20.08)[f]
Dendrion[e]	**10**			0.16-0.37	
	20			0.57	

3-4 Conclusions

In this study we investigated the effect of temperature on structure and water transport of hydrated S-PEEK with two different water contents (10wt% and 20wt%) using full-atomistic molecular dynamics simulation.

The pair correlations of sulfur - sulfur, sulfur - water and sulfur - hydronium pairs reveal very little changes as a function of temperature. We believe that this is attributed to the rigidity of the S-PEEK chain that has direct attachment of sulfonate groups. This also restricts the conformational change to accommodate the variation of water content. By calculating the structure factor, the nanophase-segregated structures of the hydrated S-PEEK membrane is characterized, showing that the characteristic dimension is not significantly changed as a function of temperature whereas the concentration contrast becomes greater with increasing water content. Particularly, from the increase of the structure factor at q = ~0.5 $Å^{-1}$, the water channel with ~13 Å of dimension is developed more with increasing water content from 10 wt % to 20 wt %.

By analyzing the pair correlation function of water – water pair, it is found that the internal structure of the water phase is more developed with decreasing temperature and increasing water content. Accordingly, the water coordination number is larger in the more developed internal structure of the water phase.

Within the water phase, the water molecules diffuse through the membrane as shown in the change of the mean square displacement of water molecules as a function of time. The diffusion coefficient of water is larger at higher temperatures and more water

content. From this temperature dependency, the activation energy of water diffusion is calculated: 25.7 kJ/mol and 24.9 kJ/mol for 10 wt % and 20 wt %, respectively. Although the activation energy is reduced as the water content is increased, their values are very similar, which imply that the diffusion mechanism is similar within the simulated water content range. Despite the similar activation energy for the water diffusion, the higher water diffusion coefficient is obtained at larger water content. This is because the more developed nanophase-segregated structure at larger water content.

Compared to bulk water (13.2 kJ/mol) and water in Nafion (16.7-18.9 kJ/mol), it is confirmed that the less nanophase-segregation in hydrated S-PEEK membrane is responsible for the larger activation energy for the water diffusion in the S-PEEK membrane.

Chapter IV

Aromatic Ionomers with Highly Acidic Sulfonate Groups: Acidity, Hydration, and Proton Conductivity

The work presented here was published by the author in Macromolecules.[108] This study was done as a joint study with an experimental partner at the University of Nevada. Our experimental partner provided the experimental results presented here and asked us to help explain the behavior of their newly synthesized polymer. Synthetic details not relevant to this work are in the appendix for completeness.

A novel sulfonation method that involves iridium-catalyzed aromatic C–H activation/borylation and subsequent Suzuki–Miyaura coupling with sulfonated phenyl bromides was developed by Dr. Bae to prepare aromatic ionomers. Superacidic fluoroalkyl sulfonic acid as well as less acidic aryl and alkyl sulfonic acids were incorporated into the aromatic ring of the model polystyrene, and the resulting sulfonated ionomers were characterized for their properties as proton-conducting membranes. The membrane properties of ionomers containing sulfonic acid groups with different acidity strengths were compared to study the effect of acidity on the water properties, proton conductivity, and morphology. The superacidic fluoroalkyl sulfonated ionomer (sPS-S_1) exhibited a significantly higher proton conductivity than that of the less acidic aryl and alkyl sulfonated ionomers (sPS-S_2 and sPS-S_3, respectively) at low relative humidity. This despite a lower ion exchange capacity and lower water uptake. Hydration behaviors of the ionomers as a function of relative humidity were studied to correlate the acid strength of the sulfonates and water uptake properties. Morphology studies of the

sulfonated ionomers show that sPS-S_1 has a larger hydrophilic domain than that of sPS-S_3. Molecular dynamics simulations were performed by myself to understand the origin of the improved proton conductivity of the superacidic ionomer at the molecular level. These simulations suggest that the enhanced proton conductivity of sPS-S_1 is due to the cumulative effect of higher acidity of the sulfonate. This leads to increased dissociation of the hydronium ions and a higher degree of ionic character in the sulfonate, and better solvation of the sulfonate with water molecules.

4-1 Introduction

Proton exchange membrane fuel cells (PEMFCs) are considered one of the most promising clean energy conversion technologies for alleviating environmental problems associated with burning fossil fuels.[109-113] The eponymous electrolyte functions as a proton conductor and separates hydrogen fuel from the oxidizer in PEMFCs. State-of-the-art PEMFC technology currently relies on perfluorosulfonic acid (PFSA) membranes, such as Nafion, due to their high proton conductivity.[114, 115] The high conductivity of PFSAs in PEMFCs is believed, especially at low relative humidity (RH), to be related to the strong acidity of their perfluorosulfonic acid groups. Also contributing to the proton conductivity is the distinct nanoscale phase-separated morphology due to the extremely hydrophobic perfluorinated polymer backbone and the flexible, hydrophilic fluoroalkyl sulfonic acid groups.[110, 111, 115, 116] Although Nafion has been the most commonly used PEM in recent decades, its properties could be improved for broader fuel cell applications. The drawbacks of Nafion include its high cost, the technical challenges of

the needed fluorine precursors, high methanol permeability in direct methanol fuel cells, and poor mechanical stability at high temperatures (>100 ºC). Furthermore, the lack of reactive sites in the perfluorinated structure of Nafion makes modifications to overcome these shortcomings difficult.

Compared with perfluorinated polymers, aromatic-based polymers are less expensive, more readily available, and easier to modify.[109] Considerable efforts have therefore been devoted to the development of aromatic PEMs as Nafion alternatives. Numerous examples of randomly sulfonated aromatic copolymers based on polybenzimidazoles,[117] poly(ether ether ketone)s,[118] poly(arylene ether sulfone)s,[119-121] polyimides,[122-124] and polyphenylenes[125] have been prepared. These were investigated as alternative PEM materials and some examples of aromatic PEMs show promise for fuel cell operations. However, these types of PEMs generally have achieved high proton conductivity only at fully hydrated conditions and their conductivities drop sharply if RH is lowered. Because increased system efficiency results from operating PEMFC's under reduced RH, development of PEMs that are highly conductive at reduced RH is critical for successful adoption of fuel cell technology in automobile transportation applications.[112]

Recently, studies of the relationship between morphology and proton conductivity have drawn considerable attention to the increase in proton conductivity at low RH in the design of new PEMs.[126-133] Accordingly, sulfonated multiblock copolymers composed of hydrophilic and hydrophobic aromatic units have been investigated to provide continuous proton conduction pathways. Although multiblock copolymer ionomers can achieve enhanced proton conductivity at low RH in comparison to

randomly sulfonated ionomers, the conductivity at low RH has not reached the level needed for practical low RH PEMFC operations.

In addition to their nanoscale phase separation, another characteristic feature of PFSA ionomers is their strong acidity. Owing to the strong electron-withdrawing effect of fluorine, the fluorinated sulfonic acid in PFSA is an extremely acidic group (also called a superacid). Although accurate measurement of the strength of this group is difficult, the acidity range is expected to be similar to that of perfluoroalkyl sulfonic acid (approximate $pK_a = -14.1$).[134] Unlike PFSAs, there are few aromatic ionomers with super acid groups.[135-142] Although these perfluoroalkyl-sulfonated (superacidic) aromatic ionomers have exhibited better proton conductivity at reduced RH compared to typical sulfonated aromatic PEMs, most superacidic ionomers are still restricted by synthetic considerations; when less efficient Ullmann coupling is used, low ion-exchange capacity (IEC; <1.5 meq/g) is obtained.[135-138, 143] Importantly, there have been no comprehensive studies exploring the effect of acidity on fuel cell membrane properties, such as how increased acidity affects proton conductivity, morphology, and water transport behavior within a PEM.

Our experimental partners, therefore, synthesized three different ionomer materials made of a polystyrene backbone with a sulfonate group attached. The strength of the acid group was modified by attaching it to the backbone through different sidechains. This is shown in Figure 20. The three side chains are fluoroalkyl, aryl and alkyl groups that have different electron withdrawing effect on the attached sulfonate, and therefore acid strength. In particular the fluoroalkyl group has a strong electron withdrawal effect due to the fluorine atoms.

By comparing the properties of aromatic PEMs with different acid strengths, we sought to understand the relationship between the chemical structures of ionic groups and the property of PEMs at the molecular level. To this end, I conducted molecular dynamics studies of the synthesized PEMs to more fully understand the mechanism underlying acid group interactions with water molecules within the membrane. The simulation was a full atomistic simulation were I investigate the nanophase-segregated structure and transport properties of the hydrated sulfonated syndiotactic polystyrene membrane with 10 and 20 wt% water contents at 353.15 K.

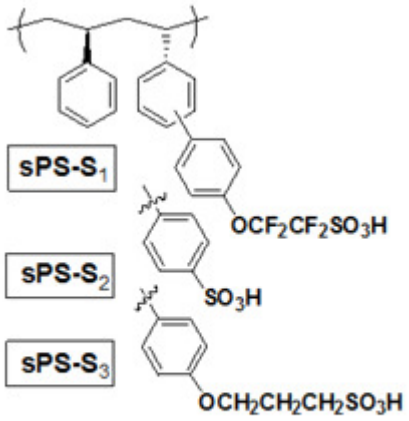

Figure 20:The ionomer studied has a polystyrene backbone with three different side chains attached to the sulfonate group. The S_1 has a perfluorinated sidechain, while the S_3 is an alkyl group. S_2 is attached though a much shorter aryl group. For the computational part of this study we focused on S_1 and S_3 because their sidechains are very similar and allow for a more direct comparison on the effect of acid strength.

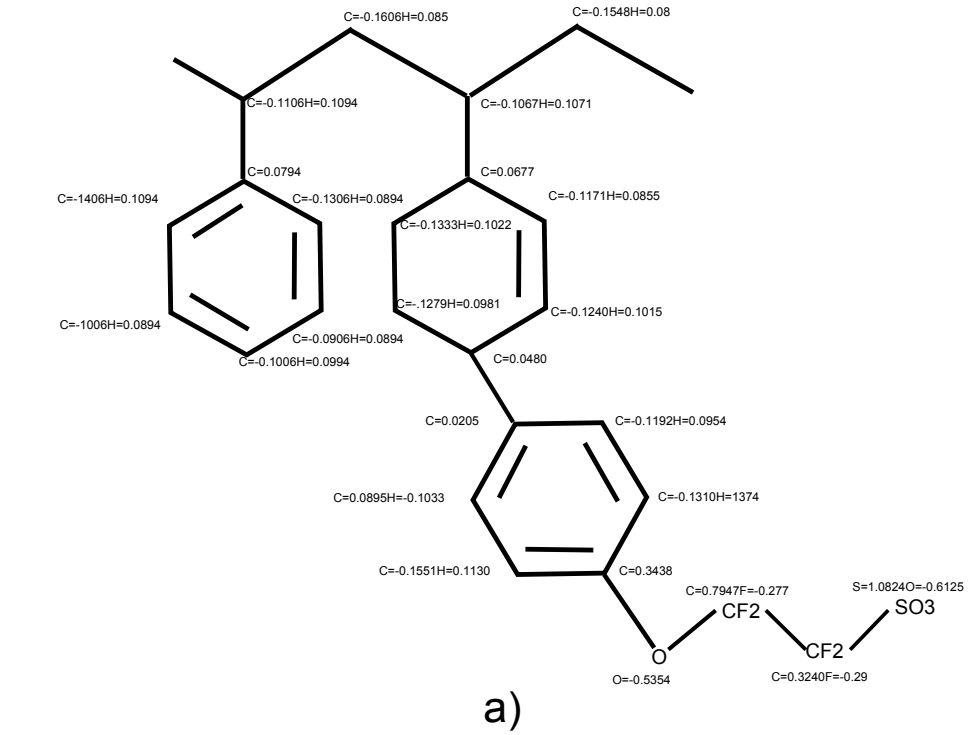

a)

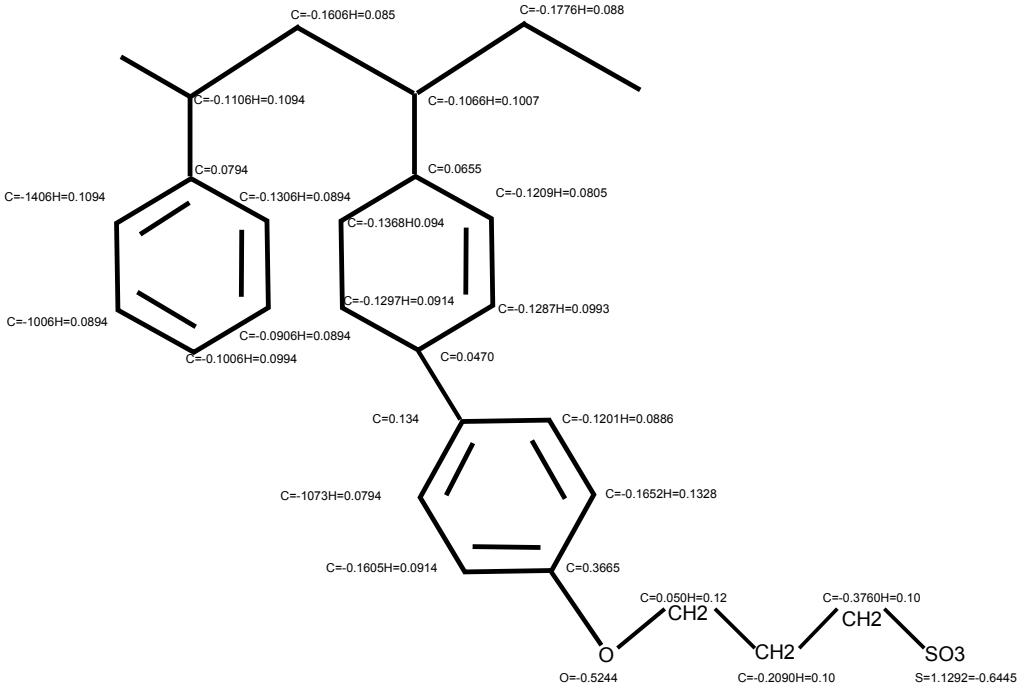

b)

Figure 21: The charge scheme used in our simulation for a) perfluorinated backbone b) alkyl backbone

4-2 Computational Models and Methods

4-2.1 Force Field and Simulation Parameters.

To perform molecular dynamics (MD) simulations, I used the DREIDING[144] force field which has been used for other fuel cell studies such as Nafion,[145] Dendrion[146, 147] and sulfonated poly(ether ether ketone)[51] as well as for various molecular systems such as hydrogels,[31, 148] liquid-liquid and liquid-air interfaces,[33, 149] and molecular self-assembly.[150, 151] The F3C force field was employed to describe the water molecules.[152] These force field parameters are described in the original paper and a previous study on hydrated Nafion.[145] The form of the potential energy used, therefore, is:

$$E_{total} = E_{vdW} + E_{Q} + E_{bond} + E_{angle} + E_{torsion} + E_{inversion} \quad (6)$$

where E_{total}, E_{vdW}, E_{Q}, E_{bond}, E_{angle}, $E_{torsion}$ and $E_{inversion}$ are total energies, van der Waals, electrostatic, bond stretching, angle bending, torsion and inversion components, respectively. The individual atomic charges of the copolymer were assigned by Mulliken population analysis using the B3LYP functional and 6-31G** basis set. The atomic charges of the water molecule were from the F3C water model.[151] The Particle-Particle Particle-Mesh (PPPM) method[43] was used to calculate the electrostatic interactions.

The annealing MD and equilibrium MD simulations were performed using the MD code LAMMPS (Large-scale Atomic/Molecular Massively Parallel Simulator) from Plimpton

at Sandia[153] with modifications to handle our force fields.[145] The equations of motion were integrated using the velocity Verlet algorithm[20] with a time step of 1.0 fs. The Nose-Hoover temperature thermostat[44, 45] for the NVT and NPT MD simulations used a damping relaxation time of 0.1 ps and the dimensionless cell mass factor of 1.0.

4-2.2 Construction and Equilibration of the Amorphous Membrane.

The simulated hydrated membrane systems consist of four chains of sPS ionomers and water molecules with 10 and 20 wt% as summarized in Table 7. The degree of polymerization and the degree of sulfonation were set to 35 and 40, respectively. Thus, the number of sulfonate group per chain is 14. The sulfonated units were selected randomly from 35 repeating units in the backbone and all of the sulfonic acid groups are assumed to be ionized as assumed in the previous studies.[145-147] The initial amorphous structures of hydrated sPS ionomers were constructed using the Amorphous Builder of Cerius2.[72] Since such initial structures of polymeric materials may include unstable conformations, they were equilibrated using the annealing procedure as used in the previous studies of Nafion,[145] Dendrion[146, 147] and sulfonated poly(ether ether ketone)[51] membranes. This process accelerates the attainment of equilibrium by driving the system repeatedly through 5 cycles of thermal and volume annealing (between 300 and 600 K and between densities of 0.5 to 1.1 times the expected density).

Table 7: Composition of hydrated sPS membranes and simulation conditions.

Ionomers	sPS-S_1	sPS-S_3
Molecular weight per chain (Daltons)	7756	6624
Equivalent weight (g/mmol)	554	473
Degree of polymerization	35	35
Degree of sulfonation	40	40
Number of polymer chains	4	4
Total number of sulfonate groups	56	56

The aim of this procedure is to help the system escape from various local minima and promote the migration of species required for phase-segregation in heterogeneous systems. Details of these steps are found in the previous publications.[51, 145-147] After finishing the annealing cycles, a 100 ps NVT MD simulation and a subsequent 5 ns NPT MD simulation were performed at 353.15 K. This finalizes the annealing procedure. Then, I performed another 15 ns NPT simulations at 353.15 K for data collection.

4-2 Results and Discussion

4-2.1 Experimental Results of Hydrocarbon Ionomers

All sPS ionomers (–SO_3Na forms) prepared by Dr. Bae using this method had a good solubility in polar aprotic solvents, such as dimethylsulfoxide (DMSO) and high molecular weights, as reflected in their intrinsic viscosities (Table 8). Their membranes were readily prepared as transparent films using a solution casting method and further acidified with 1 M H_2SO_4 to yield their acid forms. The Nevada group measured the IECs of the sPS ionomers with titration and compared to the calculated values determined from ^1H NMR. At a given degree of sulfonation, the IEC values decreased in the order of sPS-S_2 > sPS-S_3 > sPS-S_1 because of the increasing sizes of the pendant sulfonate tethers.

Proton conductivity (σ_{H+}) is the primary property that determines PEM performance, and high proton conductivity at low RH is highly desired for vehicle applications. The proton conductivity of sPS-S_2 followed the typical proton conductivity pattern of aromatic PEMs;

although it exhibited high proton conductivity when fully hydrated, its conductivity dropped sharply at lower RH. In contrast, sPS-S_1 demonstrated higher proton conductivity than sPS-S_2 with an RH below 90%. This, despite sPS-S_1 lower water uptake, lower IEC, and similar hydration number. Notably, the relative slope of the conductivity (on a log scale) vs. RH of the superacidic sPS-S_1 was less steep than those of sPS-S_2 and sPS-S_3. It was almost parallel to that of Nafion: 0.020 for Nation, 0.022 for sPS-S_1, 0.029 for sPS-S_2, and 0.030 for sPS-S_3 (see Figure 22a). This conductivity behavior is unique when compared with typical aromatic PEMs. The order of the proton conductivities at reduced RH follows the same order of the acidities of the pendant sulfonic acid groups: $–CF_2CF_2SO_3H$ (estimated $pK_a = –14$)[133, 154] > $–C_6H_4–SO_3H$ (estimated $pK_a = –2.5$)[135, 155] > $–(CH_2)_3SO_3H$ (estimated $pK_a = –0.6$).[154, 156] Among the sPS ionomers studied, sPS-S_3 had the lowest conductivity across the entire RH range, possibly resulting from the combined effect of the weaker acidity of the sulfonic acid and lower WU.

The water uptake (WU) properties of PEMs has a strong influence on their proton conductivity. The WU of sPS-S_2 is greatest among the samples studied due to its high IEC (Figure 22 b). Also, it is interesting to note that sPS-S_1 has a bulk WU similar to sPS-S_3, even though the IEC of sPS-S_3 is 20% greater than that of sPS-S_1. This difference in the WU of the fluoroalkyl sulfonate sample compared to the alkyl sample can be attributed to the increased hydration of the superacid as discussed later. The λ of the alkyl sulfonate sample is lower than those of two other ionomers, likely due to its lower acidity and a hydrophobic effect of the alkyl tether (Figure 22c).

Table 8: Properties of sPS ionomers and Nafion.
[a]All sPS ionomers contain 40 mol% sulfonate in the repeating unit based on the ^{1}H NMR spectra of 3,5-dimethylphenol-protected sulfonate group. [b]IEC (meq/g) measured by titration. Calculated IEC values are shown in parenthesis. [c]Intrinsic viscosity of sodium salt form ionomer in 0.1 M NaI/DMSO at 30 ºC. [d]Water uptake (%) = $(W_{wet}-W_{dry})/W_{dry}$ measured at 98% RH and 30 ºC during dynamic RH scans used for conductivity. [e]Number of water molecules per sulfonic acid moiety (hydration number).

Ionomer[a]	IEC[b]	IV[c]	Water uptake[d]	λ[e]
sPS-S_1	1.64 (1.87)	1.41	22	7.5
sPS-S_2	2.29 (2.39)	1.01	32	7.8
sPS-S_3	2.01 (2.10)	0.85	21	5.8
Nafion 112	0.86 (0.90)	—	16	9.6

Interestingly, sPS-S_1 and sPS-S_2 had similar hydration numbers, but clearly the sulfonate moiety of the former is more effective in promoting conductivity, even at equivalent hydration. Nafion which has the same fluoroalkyl sulfonate group as sPS-S_1 shows the highest λ across all RHs, which suggests that other factors such as backbone structure may impact the hydration of the ionic groups.

The morphological characteristics of sulfonated sPS ionomers were investigated Dr. Bae by using tapping-mode AFM after exposure of the PEMs to ambient conditions for more than 6 h. In the AFM images, domains having a higher phase lag angle appear as dark areas (hydrophilic domains) and domains having lower phase lag angle appear as bright areas (hydrophobic domains). All three sPS ionomers exhibited a phase separated morphology with slightly different hydrophilic and hydrophobic domain sizes, but no obvious connectivity among the hydrophilic domains was observed. The hydrophilic domain size of sPS–S_1 was ~10 nm which was larger than that of sPS-S_2 (~8 nm) and sPS-S_3 (~6 nm).

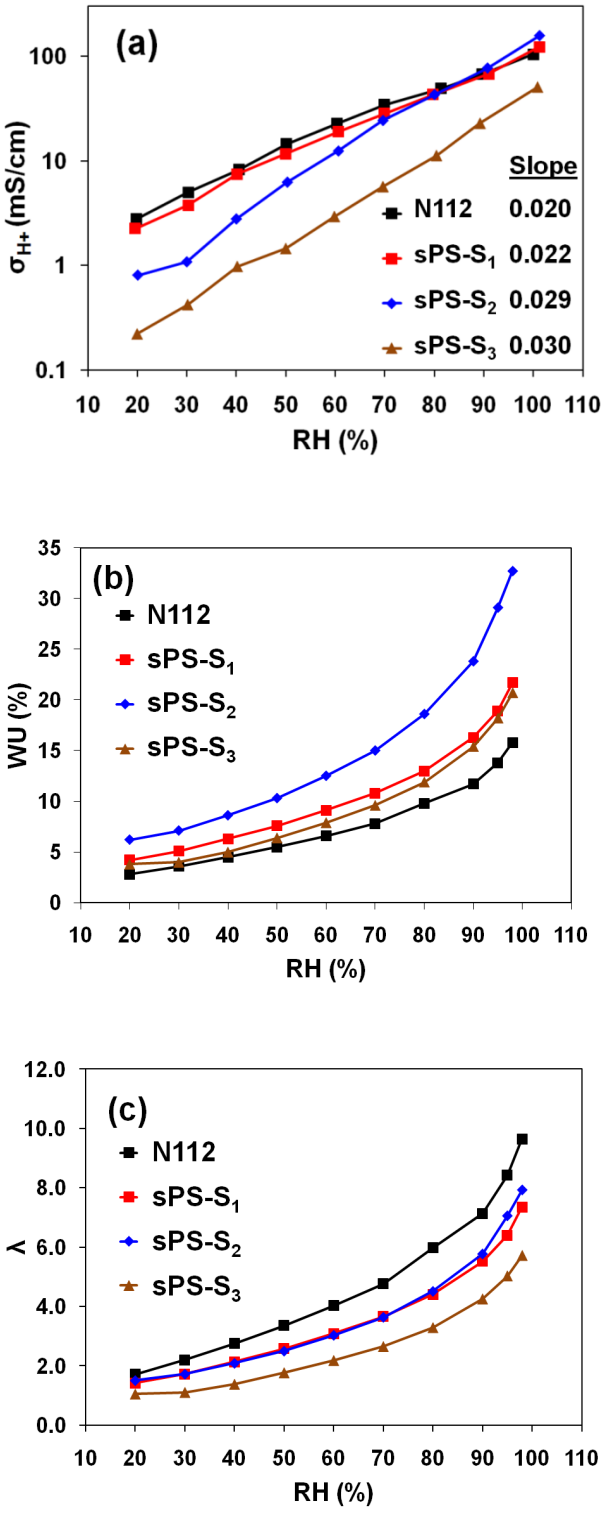

Figure 22: (a) Proton conductivity (σH+), (b) water uptake (WU), and (c) hydration number (λ) of Nafion and sPS ionomers under different relative humidity conditions.

The hydrophilic domain size does not seem to be strongly related to the acid strength of sulfonated group: superacidic fluoroalkyl sPS-S_1 has a similar domain size as the aryl sulfonated sPS-S_2. This observation is also supported by the fact that other random sulfonated poly(arylene ether sulfone)s with a similar IEC (1.5-2.2 meq/g) have a significantly greater hydrophilic domain size.[157, 158] Compared to Nafion, all three sPS ionomers demonstrated a lower degree of phase separation with smaller isolated hydrophilic domains. Of the sPS ionomers, the AFM image of sPS-S_2 exhibited a somewhat higher degree of phase mixing between the hydrophobic and hydrophilic domains. By introducing a sulfonic acid group at the terminal position of flexible pendant side chains (i.e. sPS-S_1 and sPS-S_3), improved phase separation was achieved.

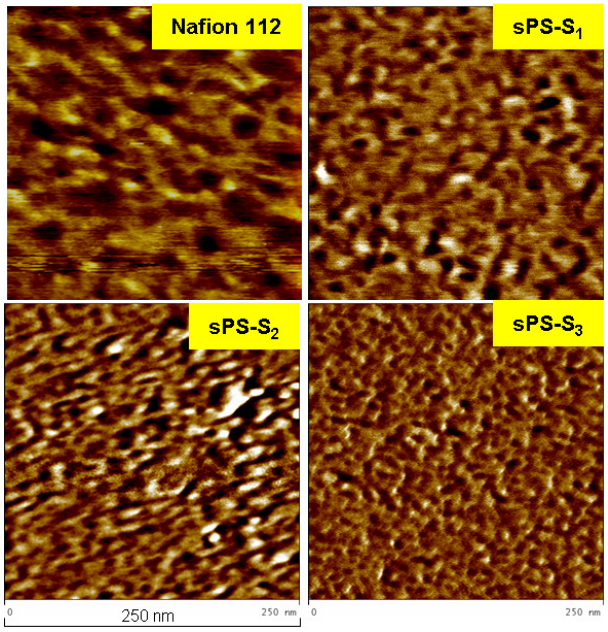

Figure 23: Morphology of Nafion and sPS ionomers studied by AFM.

The TEM images of the sPS ionomers showed morphological features similar to those observed with AFM (Figure 24): indistinct phase separation with poor connectivity

among hydrophilic domains. Because the TEM images were obtained under vacuum and there are no tip sharpness artifacts as with AFM, the hydrophilic domains of the PEMs were observed to be much smaller with TEM than what was obtained using AFM. While sPS ionomers demonstrated a low level of phase separation with significantly smaller isolated hydrophilic domains, Nafion showed distinctive nanoscale phase-separated hydrophilic domains (2–4 nm in TEM). Considering that Nafion and sPS-S_1 have a terminal sulfonate group with the same acid strength, the larger size and better continuity of the hydrophilic domains in Nafion strongly suggest that other structural differences (i.e., more hydrophobic polymer backbone, longer and more flexible side chain of Nafion) might play critical roles in enhancing the aggregation of ionic groups and formation of water channels within the PEM.

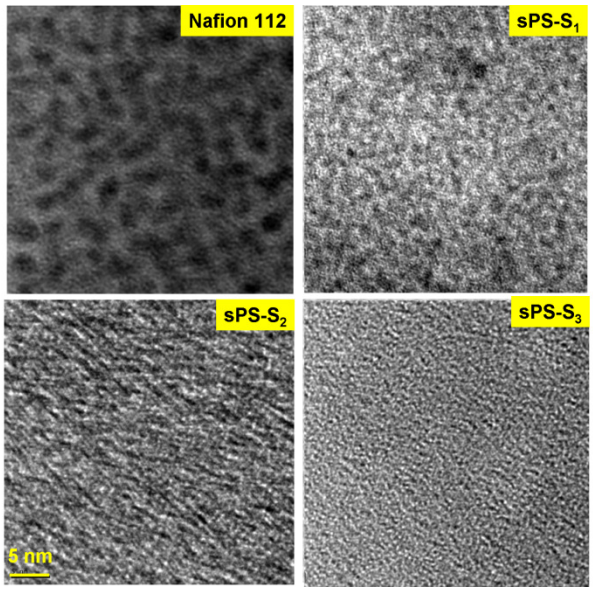

Figure 24: Morphology of Nafion and sPS ionomers studied by TEM.

The morphological study by AFM and TEM confirmed that the hydrophilic and hydrophobic domain structures depend on several other factors besides acidity, such as polymer architecture, concentration and distribution of sulfonated groups, and backbone/side chain stiffness. It is difficult to completely decouple the acidity effect from other factors in the model polymer systems we used. However, it is interesting to note that sPS-S_1 exhibited high proton conductivity at low RH even with somewhat undesirable domain structure (i.e. little observed domain connectivity), which is in stark contrast with previous multiblock copolymer approach that endeavored to form highly connected hydrophilic domains to improve low RH conductivity.

4-2.2 Simulation Results of sPS Ionomers

The experimental data above demonstrates differences in membrane properties but provides no mechanistic insight into their cause. Thus, I investigated the effect of acid strength on proton conductivity and water properties using molecular dynamics simulations. I selected two sulfonated sPS ionomers containing short side chains, sPS-S_1 and sPS-S_3, as model polymers. Because these ionomers have an identical polymer backbone structure, an identical concentration of sulfonic acid groups, and a similar flexibility along their side chains, a comparison of their properties provides a theoretical understanding of the acidity effect on PEM properties. All calculations were conducted for hydrated membranes with 10 and 20 wt% water contents at 80 ℃. The molecular parameters of the computational simulation are listed in Table 7.

Previous theoretical studies on PEM such as Nafion,[145] dendrion,[146, 147] and sulfonated poly(ether ether ketone)[51] suggest that nanoscale phase-segregation of hydrated PEMs can form well-connected water phases within the PEM. This process requires the solvation of the hydrophilic sulfonate groups by water molecules.

To investigate the relationship between acidity and interactions of the sulfonate with water molecules, I analyzed the pair correlations of sulfonate–hydronium pair, $\rho g_{\text{S-O (hydronium)}}$, and sulfonate–water pair, $\rho g_{\text{S-O (water)}}$, for sPS-$S_1$ and sPS-S_3 for 10 and 20 wt% water contents. The definition of pair correlation function, $g_{A\text{-}B}(r)$, is the probability density of finding B atoms at a distance r from A atoms averaged over the equilibrium trajectory as shown in equation (1):

$$g_{A-B}(r) = \left(\frac{n_B}{4\pi r^2 \Delta r}\right) / \left(\frac{N_B}{V}\right) \tag{1}$$

where n_B is the number of B particles located at a distance r in a shell of thickness Δr from particle A, N_B is the number of B particles in the system, and V is the total volume of the system..

The pair correlation function for the sulfonate–hydronium pair clearly shows an effect due to acidify (Figure 25a). The stronger acid group of sPS-S_1 can more readily dissociate into the ionized form and has a lower pair correlation intensity. This is because sPS-S_1 can stabilize the ionized sulfonate form due to the adjacent electron-withdrawing

CF_2 group, whereas sPS-S_3 does not have this strong electron-withdrawing group for stabilizing the negative charge on the sulfonate.

As shown in Figure 25, the intensity of [$\rho g_{S\text{-}O(water)}(r)$] increased with increasing water content for both ionomers, indicating that more water molecules gathered around the hydrophilic sulfonate groups. Amongst the two sPS ionomers, sPS-S_1 had a higher pair correlation intensity than sPS-S_3 at both water contents. To quantitatively assess the difference in pair correlation, we calculated the average number of water molecules that surround each sulfonate group, or the hydration number (λ), by integrating the first peak in Figure 25b.

The hydration numbers for sPS-S_1 were 1.78 and 3.91 at 10 and 20 wt% water content, respectively, and the corresponding hydration numbers for sPS-S_3 were 1.35 and 3.61. These results indicate that the sulfonate groups in sPS-S_1 attracts more water molecules than those of sPS-S_3. This is explained by the stronger acid group having a greater tendency to exist in an ionized form and requires solvation by more water molecules. Overall, the data of Figure 25 suggest that because of sPS-S_1 stronger acidity, and the resulting higher degree of ionic character of the sulfonate group, it attracts more water molecules for solvation. The superior solvation of the sulfonate groups in sPS-S_1 compared with that of sPS-S_3 accounts for the slightly larger hydrophilic domains of the former observed on the AFM images and contributes to its enhanced proton conductivity at low RH. This phenomenon is also observed in the hydration data where sPS-S_1 absorbs more water molecules per sulfonic acid group than sPS-S_3.

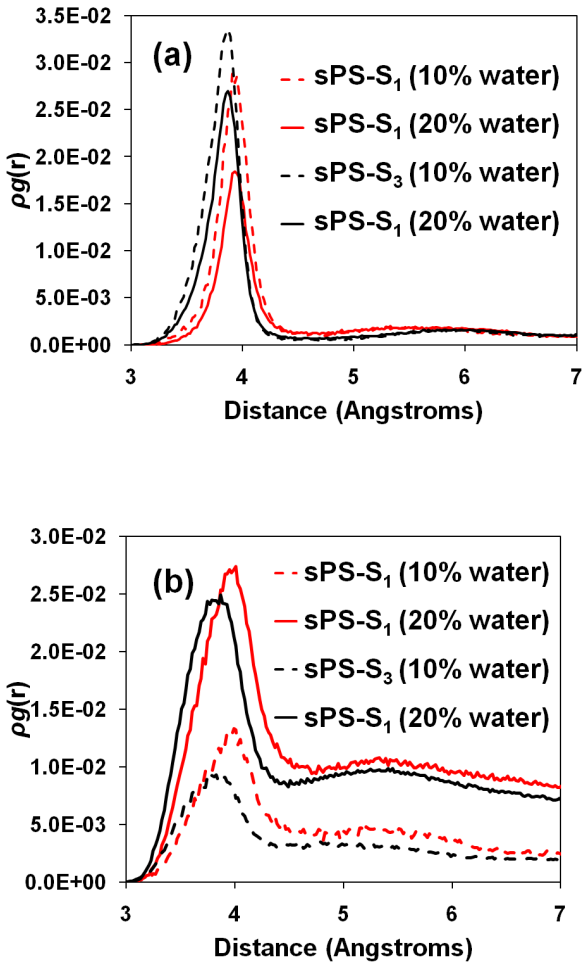

Figure 25: Calculated pair correlation functions of (a) sulfonate–hydronium ion and (b) sulfonate–water in hydrated sPS ionomers.

I also investigated the transport properties of water molecules and protons within the sPS ionomer membranes. The water diffusion coefficient (D_{water}) was calculated from the mean squared displacement of water using the following equation:

$$D_{water} = \lim_{t \to \infty} \frac{1}{6t} \left\langle \left(r(t) - r(0) \right)^2 \right\rangle \tag{2}$$

where r(t) and r(0) are the positions of water at a certain time (t) and at the beginning (t = 0), respectively. The results shown in Table 9 suggest that water diffusion increases with increasing water content. This relationship is attributed to the better development of the water phase in hydrophilic domains. As the sulfonate groups become surrounded by more water molecules, the local water concentration increases and eventually these water domains coalesce and enhance water transport. Comparison of sPS-S_1 and sPS-S_3 showed that the former achieved greater water diffusion. This result can be understood by considering the discussion of $\rho g_{S\text{-}O(water)}(r)$: more water molecules are attracted to the acid groups of sPS-S_1 and enhance the possibility of better solvated sulfonate groups and facilitate water transport in the hydrophilic phase.

I also investigated the proton diffusion of sPS-S_1 and sPS-S_3 under 10 and 20 wt% water contents. Proton diffusion can occur via two mechanisms: vehicular diffusion and hopping. The vehicular diffusion mechanism is when protons are transported as hydronium molecules diffuse through the material, whereas in the hopping mechanism protons are transported by transferring from one water molecule (proton donor) to

another (proton acceptor). The proton diffusion coefficient under the vehicular mechanism ($D_{vehicular}$) can be described by classical molecular dynamics simulation shown in equation 2. However, calculating the proton diffusion coefficient from the hopping mechanism ($D_{hopping}$) requires a quantum mechanical treatment to model the energy landscape. This is because the intermolecular distances between water molecules changes dynamically during the proton conduction. Therefore, I applied quantum mechanical transition state theory using equation 3 as described in previous studies:[147, 159, 160]

$$k_{ij}(r) = \kappa(T, r)\frac{k_B T}{h}\exp\left(-\frac{E_{ij}(r) - 1/2h\omega(r)}{RT}\right) \quad (3)$$

where κ(T,r) and ω(r) are the tunneling factor and the frequency for the zero point energy correction (adopted from literature[159, 160]), respectively, and *E*(r) is the energy barrier for a proton to be transferred from a donor to an acceptor in water at a distance of r. I first calculated the proton hopping energy barrier, *E*(r), for fixed distances between donor and acceptor oxygen atoms using DFT (B3LYP with the 6-311G** basis) to obtain how the energy varies as a function of the distance between the proton and the donor oxygen. I then used the Poisson–Boltzmann self-consistent reaction field model[161, 162] to correct the solvent effect along the reaction path, and I recalculated the energy barrier. From the results obtained from equation 3 and the distances between all the donors and

acceptors pairs determined with the equilibrium molecular dynamics trajectory, we calculated the proton hopping diffusion coefficient as follows:

$$D_{hopping} = \frac{1}{6Nt} \int_0^{t\to\infty} \sum_i^N \sum_j^M k_{ij} r_{ij}^2 P_{ij} dt \tag{4}$$

where N is the number of protons and P_{ij} is the probability that a proton will jump from hydronium i to water j defined as $P_{ij} = k_{ij} / \sum_j k_{ij}$. Here r_{ij} is the distance between all pairs of donors and acceptors measured from the equilibrium molecular dynamics trajectory. Table 9 summarizes the calculated proton diffusion coefficients of hydrated sPS ionomers. Similar to water diffusion, proton diffusion increases as water content increases, and sPS-S_1 has a proton diffusion coefficient higher than that of sPS-S_3 under both mechanisms. Particularly interesting, at 10 wt% water content, the proton diffusion coefficient of sPS-S_1 is almost three times larger than that of sPS-S_3. At 20 wt% water content, however, the proton diffusion coefficient of sPS-S_1 is only 1.3 times larger than that of sPS-S_3. Thus, the computational results strongly suggest that the effect of strong acidity on proton conduction is more significant at lower water content.

Lastly, I calculated proton conductivity (σ) based on the proton diffusion coefficient ($D_{proton,total}=D_{vehicular}+D_{hopping}$) using the Nernst-Einstein equation as follows:

$$\sigma = \frac{D_{proton,total} c z^2 F^2}{RT} \tag{5}$$

where c and z denote the proton concentration and the charge carried by the proton, respectively, and F and R denote the Faraday constant and the gas constant, respectively. T is temperature in Kelvin. The computed proton conductivity results are summarized in Table 10. The difference in computed proton conductivities between sPS-S_1 and sPS-S_3 becomes larger as the water content decreases, which is consistent with the results of proton diffusion coefficient calculations: the ratio of the calculated proton conductivities of sPS-S_1 and sPS-S_3 increased from 1.3 to 3.1 as the water content decreased from 20 wt% to 10 wt%. Therefore, more robust proton conductivity of sPS-S_1 compared to the other sPS ionomers at low RH is due primarily to the stronger acidity of the superacidic ionomer and its resulting higher diffusions of water and protons within the membrane.

Table 9: Calculated diffusion coefficients of water and protons of sPS ionomers at 80ºC.

Ionomer	Water content (wt%)	Water diffusion D_{water} ($\times 10^{-5}$ cm^2/s)	Proton diffusion	
			Vehicular $D_{vehicular}$ ($\times 10^{-5}$ cm^2/s)	Hopping $D_{hopping}$ ($\times 10^{-5}$ cm^2/s)
sPS-S_1	10	0.091	0.0029	0.25
	20	0.44	0.022	0.42
sPS-S_3	10	0.058	0.0012	0.082
	20	0.26	0.021	0.33

Table 10: Computed proton conductivity of sPS ionomers at 80 ºC.

Ionomer	Water content (wt%)	Proton conductivity (σ) (mS/cm)
sPS-S_1	10	14.4
	20	24.6
sPS-S_3	10	4.7
	20	19.5

4-3 Conclusion

A novel, efficient sulfonation method for aromatic polymers using a combination of transition metal-catalyzed borylation of aromatic C–H bonds and Suzuki–Miyaura coupling reactions was developed by Dr. Bae and his group in the University of Nevada. The new polymer functionalization method allows for convenient attachment of a variety of sulfonate groups with different acidities onto the aromatic polymer. The synthesised polymers were a polystyrene-based sulfonate ionomers by attachment of superacidic fluoroalkyl sulfonic acid and less acidic aryl sulfonic and alkyl sulfonic acids to the backbone. Then the membrane materials were evaluated for their fuel cell membrane properties. With this set of polymers, Dr. Bae performed a comprehensive study on the effect of acid strength on the proton conductivity of the sulfonated ionomers. Despite its lower water uptake and IEC, the fluoroalkyl sulfonated superacidic ionomer (sPS-S_1) maintained higher proton conductivity at low RH compared with the less acidic aryl and alkyl sulfonated ionomers (sPS-S_2 and sPS-S_3), and this difference in proton conductivity gradually increased as the RH decreased. The water uptake behavior as a function of RH and the morphology studies show that compared to less acidic ionomers sPS-S_3, the superacidic sulfonate groups of sPS-S_1 attract more water and creates enlarged hydrophilic domains. These could provide easier transport of hydronium ions and water and therefore higher proton conductivity.

I conducted comparative computational studies of sPS-S_1 and sPS-S_3 under hydrated conditions to investigate acidity effects at a molecular level. By analyzing the solvation of sulfonate groups with water in each system, I confirmed that the sulfonate groups in

sPS-S_1 are better solvated than those in sPS-S_3. Thus, the acidity effect not only induces more effective dissociation of protons (in the form of hydronium ion) from the sulfonate but also develops better solvated sulfonate groups by surrounding them with more water molecules. Due to the superacid solvation effect, sPS-S_1 has a higher calculated water diffusion coefficient and proton diffusion coefficient (under both vehicular and hopping mechanisms) than sPS-S_3. Furthermore their difference in proton diffusion was greatest at lower water content.

Overall, our studies on the effect of acid strength on fuel cell membrane properties suggest a clear relationship between acid strength and proton conductivity. The enhanced proton conductivity of the more acidic ionomer is due to the cumulative effects of better dissociation of the superacidic sulfonic acid to hydronium ion as well as the better solvation of the sulfonates. We believe that the results reported herein are a significant step toward the development of highly conductive hydrocarbon-based ionomers.

Chapter V

Interaction of Pt Nanoparticle with Molecular Components in a Three-Phase System

In the three phase boundary region of Polymer Electrolyte Membrane Fuel Cells (PEMFC), the electrolyte, catalyst and electrode work in concert to ensure operation. Technical challenges in developing a simulation study of this region are numerous; the first step in developing a model is a quantum mechanical study of the materials and their interaction. To this end, we preformed various Density Functional Theory simulations of platinum clusters and their interaction with various moieties. We developed a DFT simulation protocol, a model for the cohesive energy of Pt clusters and found the binding energy curves for various moieties on Pt, which will allow us to develop an MD model of the three phase region. To validate our simulations we compared our results with others and their methods. Having developed the protocol, we developed a cohesive energy model that uses the coordination model of the Pt atoms in the cluster. From this we determine which Pt atoms are least tightly bound to the cluster and the energy and shape distribution. Finally our adsorption simulations gave us the binding energy curves for the Pt clusters with adsorbed moieties.

5-1. Introduction

There has been a significant amount of interest in metal particles with small sizes down to the nanometer scale. This is due to their engineering importance[163-166] since the

property of materials with size below a certain length scale is distinctly different from that from the bulk phase.[167, 168] This is true for transition metals, as quantum effects are more prominent as the surface-volume ratio increases. [169, 170] In particular, platinum nanoparticles, despite their high price, are considered as the catalyst of choice for fuel cell technology due to their excellent catalytic abilities. Therefore, theoretical and computational[171-177] investigations as well as experimental approaches[178-180] have been performed extensively to understand this material. The aim of this research is the maximizing of the benefit from the use of such precious metal and also understand the underpinning fundamentals of the observed properties.

There have been many experimental studies on Pt nanoparticles as well as theoretical work. The experimental research has investigated crystallographic changes of structures through spectroscopic study. At the same time, theoretical studies were trying to explain the shape of clusters while overcoming artifacts of DFT in describing heavy metal atoms by considering various electronic correlations.

In experiments it was found that the metallic character depends on the size of the cluster; Eberhart et al. [178] were able to create metal clusters of 1-6 atoms and found using photoemission spectroscopy that such metal clusters did not have metallic character. Also, the Pt dimer was found to have a different bond length than the bulk. Airola[180] and Morse studied the Pt dimer using fluorescence spectroscopy and obtained the bond length of 2.33Å for the ground state, compared to the bulk length of 2.774 Å. Given how different these clusters are, the smallest Pt clusters might not be representative of a catalytic material. Wang and his coworkers[179] reported that Pt clusters of tetrahedral symmetry maintain their shape up to 350 - 450 °C beyond which Pt clusters tend to

become spherical. They also found that the melting temperature of the clusters is significantly lower than the bulk melting temperature.

Compared to experimental characterization, the theoretical and computational approaches may have distinct advantages in tackling small systems with nano scale dimensions by directly investigating the atomic structures and the corresponding properties. To improve DFT calculations, various theoretical aspects were introduced. To obtain better energy and geometrical results, dynamical and non-dynamic electron correlation was considered by Lee et al, [177] to obtain reliable spectroscopic data relativistic effects for binding energy for heavy metals were introduced by Varga et al, [171] and Grönbeck and Andreoni[172] studied neutral and anion various shapes to Pt_5 using SLDA and BLYP. Their calculations found that 3-D geometries are not favoured up to Pt_5 clusters. Through a DFT study on large size of Pt clusters shapes using PW91 and plane wave basis set, however, Xiao and Wang[175] found that the planar shape is preferred for small clusters up to 9 atoms, because the layered Pt clusters are very stable compared to closed-packed spherical shapes. This is in agreement with other research groups.[176, 181, 182] However, a hybrid functional DFT study using B3LYP by Sebetci [183] showed contradictory results reporting that 3-D geometries are energetically preferred on Pt_n (n = 4 - 6). It is thought that small size clusters show their peculiar energy state due their size and energy state. The quantum mechanical properties of confined electrons on small clusters is not fully understood, but it is known that change in geometry also leads to specific stabilized electronic energy states even for an equal number of electrons. To avoid problems with shape and spin dependency when studying small-size clusters, it is required to research on various size clusters, DFT functionals and spin multiplicity of the

cluster. Apra and Fortunelli [174] reported that Pt_n (n=13, 38 and 55) start developing metallic characteristics already, especially Pt_{55} favors the icosahedral geometry (I_h) whereas Pt_{13} favors the D_{4h} geometry. In addition, Chepulskii and Curtarolo[184] calculated the energy of various common Pt nanoparticle shapes as a function of size up to 400 atoms using various GGA functionals and plane wave basis set. From such large cluster calculations, they found that the surface energy depends on the lattice parameter and the bulk surface energies are only valid for nanoparticles with the diameter greater than 1.46~1.57 nm.

Our work on platinum nanocluster uses DFT to model the energy of a large set of clusters. From this we build an energy model of the platinum nanocluster similar to cluster expansion models.[185-189] From this we obtain the cluster size distribution for a given number of atoms.

Fuel cell molecular species are also present on the catalyst surfaces. Investigating the interaction of Pt with molecular species is difficult. Work on Pt-water interaction includes work by Langenbach et al.[190] who used via IR-reflection and UV-photoemission and found that water molecules are adsorbed on the Pt (111) surface via its oxygen atom. Michaelides et al.[191] confirmed the water adsorption on the on-top site of Pt (111) surface using DFT. DFT studies agree that water's oxygen atom is positioned on the on-top position of Pt nearly parallel to the surface. There is also agreement on the binding energy of water on a plane (111) surface, but there is no such consensus for the binding energy of water on a Pt cluster. [191-206]

Oxygen adsorption on Pt 111 has also been studied, both experimentally[207-210] and computationally[211-214], and it is found that oxygen can be in many different states. Chemisorbed molecular oxygen can be in both paramagnetic (top-bridge-top) and nonmagnetic state (tilted bridge on the fcc and hcp sites). Experiment and computation agree on the preferred configuration for the molecular physisorbed state, the top-brdige-top configuration, however most computation find an adsorption of around 0.7 eV, whereas the experimental results are 0.38 eV[209] and 0.5 eV. However, Ohma et al. obtained a binding energy of 0.39 eV for the oxygen molecule adsorbed in the bridge site using DFT.[215]

Little research has been done on Nafion adsorbed on Pt with DFT. Of note, Kendrick et al. used DFT to confirm his experimental work suggesting that the sulfonate group is strongly bound to the Pt surface. He also found that the CF3CF3 groups are also strongly bound.[216] In this study we studied various adsorbed species on Pt, including water, oxygen, hydronium, and various Nafion fragments. From these simulations, we built a computational system to study the three phase interface of a PEMFC. To this end we have probed the phase space of these moieties on the Pt surface to obtain the strength of their interaction, the position and conformation of the adsorbed species. From this we developed a force field for use in a molecular dynamics study of the three phase interface of the PEMFC system.

5-2. Computational Methods

In order to investigate electronic structure and energies from various Pt nanoparticles, we used spin-unrestricted Density Functional Theory (DFT) through Jaguar.[217] By employing three widely used functionals M06,[218, 219] PBE[220, 221] and B3LYP[222, 223] with LACVP** basis set containing 6-31G** and LANL2DZ effective core basis set,[224] we attempted to compare the electronic structures and interactions of Pt nanoparticles of various shape and size (Figure 30) which have up to three layers.

For our larger systems, we also used spin-unrestricted periodic DFT through CASTEP[225] implemented in Materials Studio[226] with PBE functional and a plane wave basis set, to compare to our non-periodic DFT calculations with the local basis set. By design, some functionals are more suited for certain materials than others and users must select the appropriate one suited for their study. In particular, PBE is widely used for metallic studies, and B3LYP is widely used for organic systems.

The electronic structure of platinum particles depends on both on the size and shape of the particle. Consequently, different clusters have different minimum energy multiplicities. To perform our jaguar calculations we started with a guess of the initial spin states, using the interstitial electron model described by McAdon and Goddard and as used by Kua and Goddard.[227, 228] This method identifies the location, and therefore number, of the interstitial electrons. From this the number of unpaired electrons is obtained. By having a good guess of the initial spin state, the amount of work required to get the correct spin state is reduced. Then we simulated different multiplicities around

this initial guess until we arrived at the lowest energy one. We verified that the various functionals agree on the lowest energy multiplicity.

5-2.1 Building our cluster models

We built clusters of different shape and size. The smallest clusters, (up to 5 atoms) were carved from the crystal structure by trying to exhaustively obtain all of the combinations. Due to their small size, these structures carved from the crystal structure are not expected to be the lowest possible energy. This is because the crystal lattice is for an infinite bulk having, therefore, insignificant surface energy.

In addition to small clusters, we also investigated medium sized clusters (up to n =35). Our method for making medium sized clusters is different from the method to build small clusters. Whereas the small clusters were built trying to exhaust all possible shapes within our constraint of being on lattice, this is no longer possible, for large n, because the number of possible shapes increases greatly as the number of atoms is increased. Instead, our clusters were built by carving out the crystal structure of platinum into various shapes. Shapes chosen include highly symmetric shapes, as well as random shapes (see below). As the number of atoms is increased clusters become more bulk-like.

The set of clusters built by carving out the crystal structure introduces some bias because they were built by the user carving them out from the lattice. These clusters were usually very symmetric. To eliminate this bias, we sought to add clusters without this systematic bias. These clusters are of random shape and were built by a computer program.

This program was a Monte Carlo program that used Boltzmann sampling to generate different shapes constrained to the Pt crystal lattice and also constrained to be a connected graph (a move is allowed only if the cluster remains whole). After inserting n atoms during the initialization, the program randomly picks an atom and attempts to move it according to the move's resulting change in energy and the simulated temperature. The energy model used for these MC calculations was from the preliminary results from the coordination-model developed in the course of the study. Since we wanted to sample a large portion of phase space, we annealed the clusters by bringing the temperature up to 5eV. We then added these clusters to our energy model and generated new ones to validate it.

5-2.2 Interaction with Water and Hydronium

To describe the interaction of water (H_2O) and hydronium (H_3O^+) molecules with Pt (111) surface, we obtained the adsorptive binding energy using M06 functional with LACVP** basis set. For this purpose, the structure of H_2O -$Pt_{14\text{-}13\text{-}8}$ and H_3O^+-$Pt_{12\text{-}7}$ nanoparticle was optimized (a and b) and then, the binding energy was calculated as a function of phase space. This is done by moving the molecules in many directions, especially along the direction normal to the surface. Usually the direction normal to the surface had the strongest change in energy, however, in the case of the water molecule we found that to obtain a good force field we had to change it's orientation extensively along two angles as well. c shows that the binding energies are 15.01 kcal/mol at the distance of 2.411 Å and ~ -40.43 kcal/mol at the distance of 2.899 Å for water and hydronium, respectively. Due to the magnitude of the binding energy, and no spin

change, it is clear that the water molecule is physisorbed on the Pt (111) surface. On the other hand, we observe that the binding of hydronium with Pt surface is much stronger than that of water due to the charge. This type of strong adsorption of the charged molecular species onto the metal surface is due to the polarization of the metal surface induced by the charges in the molecule; that is, the positive H_3O^+ molecules changes the available energy states on the Pt surface near the hydronium. As a consequence, there are more electrons occupying states on the platinum atoms near the H_3O^+ than there otherwise would be. This can also be explained succinctly with the classical electromagnetism results of a charge near a conductor surface: an opposite "mirror" charge is induced. The charge-charge interaction between the positive hydronium and the excess electrons cause the strong observed binding energy. Thus, these results indicate that the hydronium molecule are preferable on the Pt nanoparticle.

5-2.3 Interaction with Oxygen Molecule

Currently experimental [207-210] and computational [211-214] studies agree that the lowest physisorbed state for molecular oxygen is along the Pt-Pt bond. However most computation find an adsorption of around 0.7 eV, whereas the experimental results are 0.38 eV[209] and 0.5 eV, although Ohma et al. in 2010 found a binding energy of 0.39 eV using DFT.[215]

In our study we started by geometrically optimizing various configuration of the oxygen (O_2) molecule adsorbed on the Pt (111) with DFT. Many different starting configuration are needed because there are many local minima in the Pt-molecular oxygen energy phase space. The initial states used are reproduced in Figure 26. We found that an oxygen

(O_2) molecule lies along the Pt-Pt bond on Pt (111) surface (a),in agreement with previous studies. Furthermore, many of oxygen molecules in the various initial configurations ended up along the Pt bond. For the geometric optimization we tried six different initial positions because the O_2-Pt interaction is very complex. For thoroughness, we also tried many different spin states. By analyzing the change of the binding energy as a function of the distance from the Pt surface, the O_2 adsorption on Pt (111) surface takes place through two mechanisms, chemisorption or physisorption. As shown in b, through chemisorption, O_2 molecule is adsorbed at 2.12 Å of the distance from the Pt surface with -7.71 kcal/mol of the binding energy (S=11 where S is spin multiplicity). On the other hand, the physisorption occurs at 2.72 Å of the distance with a smaller binding energy (-7.07 kcal/mol or 0.31 eV) (S=13). Our physisorbed result is closer than most other DFT results. Also, it is observed that the physisorption has a longer distance from the Pt surface compared to the chemisorption. c shows that, after O_2 physisorbed Pt surface at 2.72 Å, can form a chemisorbed state by overcoming the energy barrier at ~2.5 Å. This is a first step towards the oxygen reduction reaction which is not within the scope of this study since the oxygen reduction reaction has been studied very intensively.

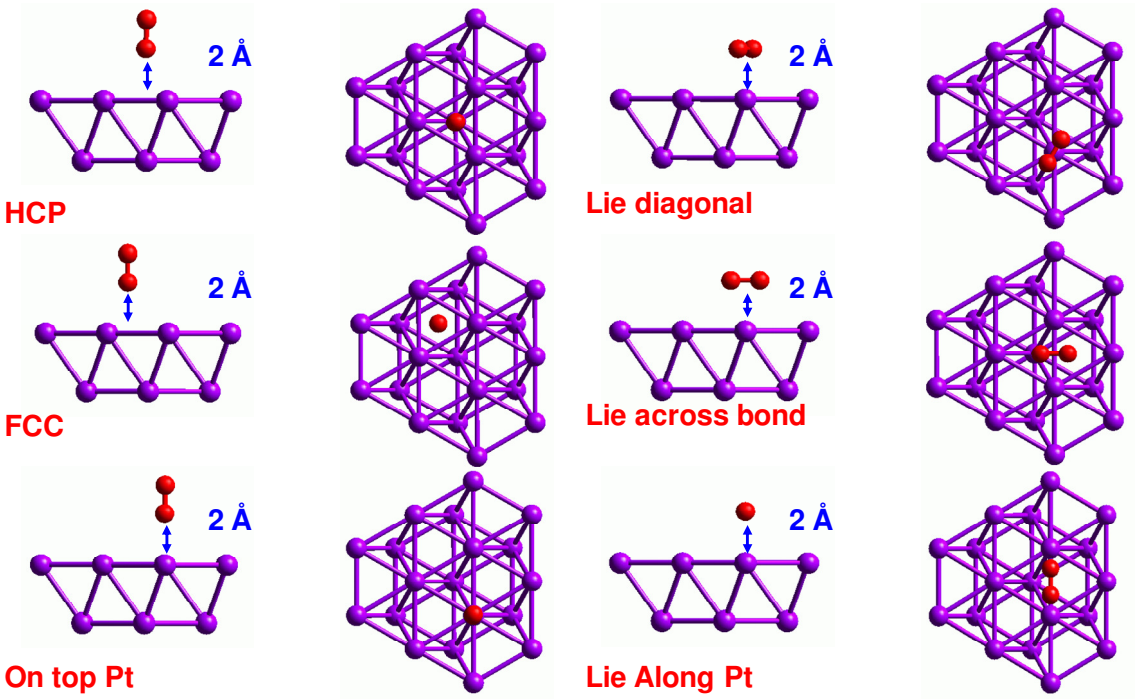

Figure 26: Side and top views of the six initial configurations before geometrically optimizing molecular oxygen on the Pt surface.

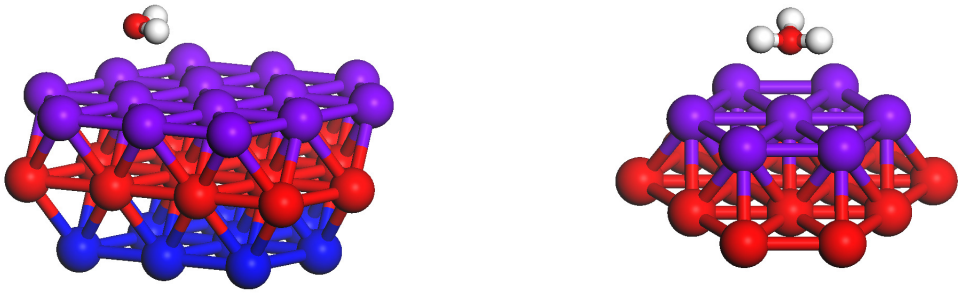

(a) (b)

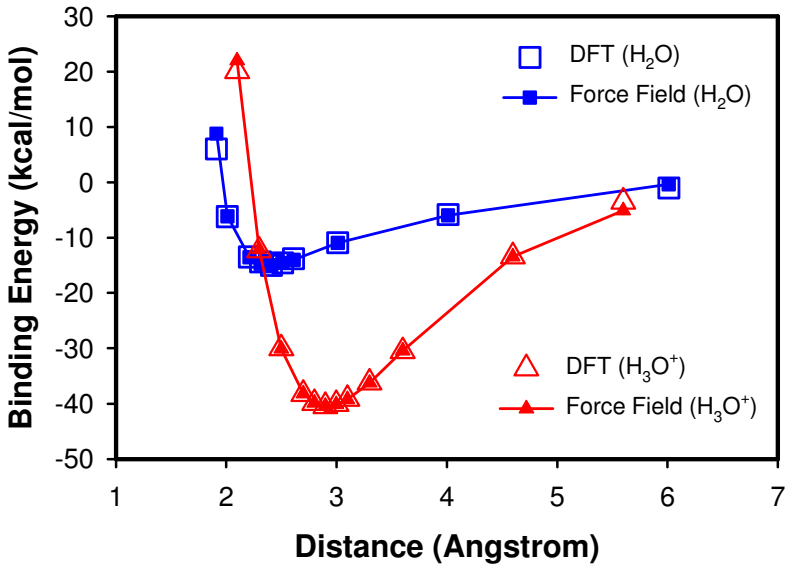

(c)

Figure 27: Adsorptive binding energy of H_2O (water) and H_3O^+(hydronium) molecule on Pt (111) surface: (a) optimized geometry of H_2O-$Pt_{14\text{-}13\text{-}8}$; (b) optimized geometry of H_3O^+-$Pt_{12\text{-}7}$; (c) change of binding energy of H_2O and H_3O^+ on Pt (111) surface as a function of distance from the surface along the surface normal. For DFT calculations, M06 functional is used with LACVP** basis set. For force field calculations, Morse potential function is used with newly optimized off-diagonal van der Waals parameters.

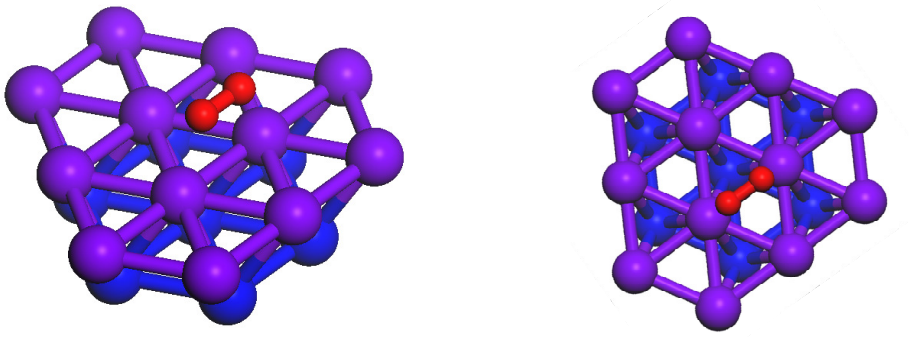

(a) (b)

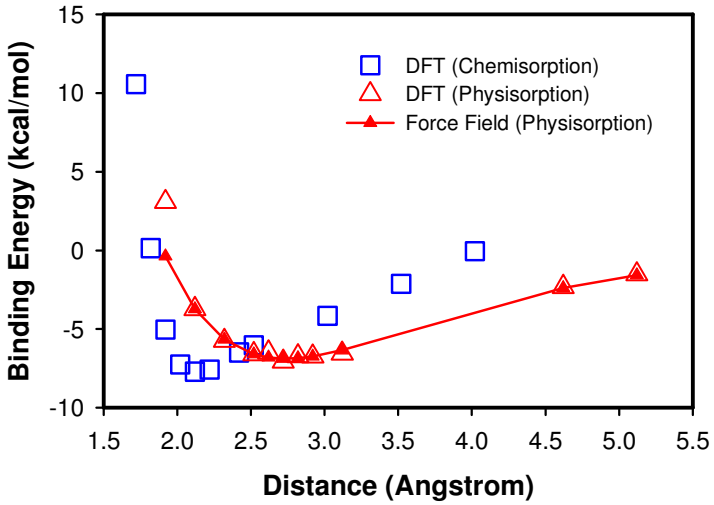

(b)

Figure 28: Adsorptive binding energy of O_2 (oxygen) molecule on Pt (111) surface: (a) tile view of optimized geometry of O_2-$Pt_{14\text{-}13\text{-}8}$; (b) top view of optimized geometry; (c) change of binding energy of O_2 on Pt (111) surface as a function of distance from the surface along the surface normal. For DFT calculations, M06 functional is used with LACVP** basis set. For force field calculations, Morse potential function is used with newly optimized off-diagonal van der Waals parameters.

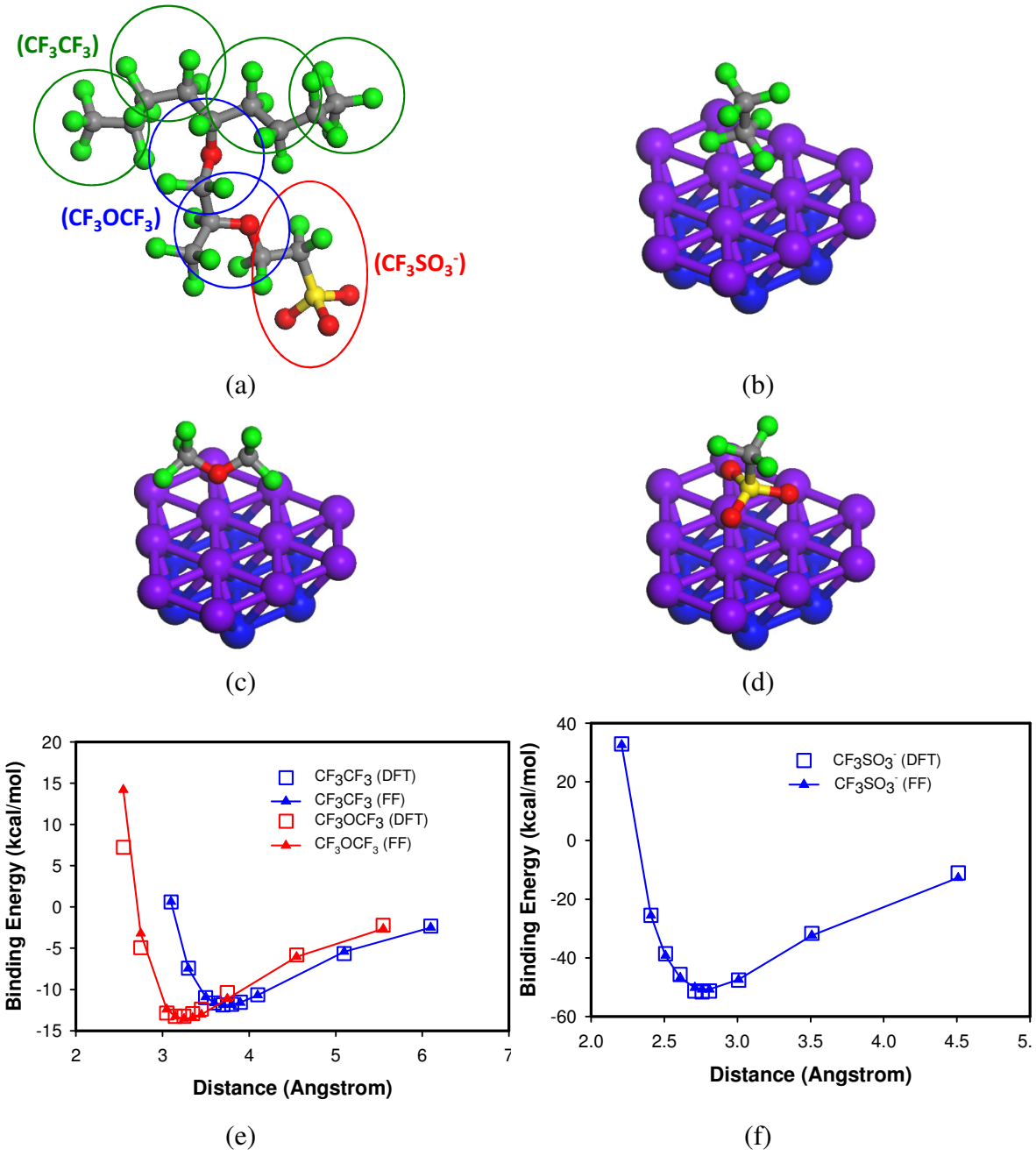

Figure 29: Adsorptive binding energy of fragments of polymer electrolyte (Nafion) on Pt (111) surface: (a) fragments of Nafion; (b) optimized geometry of CF_3CF_3-Pt_{12-7}; (c) optimized geometry of CF_3OCF_3-Pt_{12-7}; (d) optimized geometry of $CF_3SO_3^-$-Pt_{12-7}; (e) change of binding energy for CF_3CF_3-Pt_{12-7} and CF_3OCF_3-Pt_{12-7} vs. distance from the surface along the surface normal; (f) change of binding energy for $CF_3SO_3^-$-Pt_{12-7} vs. distance from the surface along the surface normal. For DFT calculations, M06 functional is used with LACVP** basis set. For force field calculations, Morse potential function is used with newly optimized off-diagonal van der Waals parameters.

5-2.4 Interaction with Polymer Electrolyte (Nafion)

Although the surface of the electrode is coated by an ionomer, its interaction with the Pt catalyst is not thoroughly understood In order to investigate the Nafion-Pt interaction, first, we prepared three small model molecules by segmenting the Nafion unit structure (a) such as perfluorinate (CF_3CF_3), perfluorodimethyl ether (CF_3OCF_3), and perfluoromethyl sulfonate ($CF_3SO_3^-$). CF_3CF_3, CF_3OCF_3 and $CF_3SO_3^-$ represent the backbone chain, the side chain ether and the sulfonate group of side chain in Nafion, respectively. This division of the polymer chain is inspired, and justified, by the common abstraction in polymer science that treats a polymer chain like a chain of beads. In this abstraction model, the polymer chain is treated like linked beads. Likewise we divide our Nafion chain into smaller segments and assume that each atom type's interaction with the platinum does not change if they are in a representative segment or the polymer.

We performed a DFT geometry-optimization of these model molecules on the Pt (111) surface as presented in b, c and d. For each system we tried several initial positions since the geometric optimizer cannot guarantee global minimization. Our computation resulted in the following binding energies: -11.88 kcal/mol at 3.70 Å, -13.25 kcal/mol at 3.25 Å, and -51.33 kcal/mol at 2.71 Å for CF_3CF_3-Pt_{12-7} (b), CF_3OCF_3-Pt_{12-7} (c) and $CF_3SO_3^-$-Pt_{12-7} (d), respectively. All the distance are from the surface along the surface normal. The size of the binding energy indicates that CF_3CF_3 and CF_3OCF_3 are physisorbed, and no change in optimal spin state was found. Like the H_3O^+, the CF_3SO3^+ charged nature causes significant changes in the metals' electronic state resulting in a large binding energy. From the binding energies of these model molecules, it is inferred that the surface

of Pt nanoparticle is occupied by the sulfonate groups of Nafion, hydronium, and water molecules while CF_3CF_3 and CF_3OCF_3 may not be able to occupy the surface of Pt nanoparticle. However, these segments must be near the catalyst since the sulfonate group is attached to the backbone through these segments.

5-2.5 Three Phase Molecular Dynamics Model

Having developed a force field for Nafion-Pt interaction we built a MD model of the three phase region of the fuel cell using. This model contains the electrolyte, the electrode and the catalyst at the cathode region. Furthermore, a vacuum layer was added. This vacuum layer is the channel by which gaseous molecules are introduced or removed from the electrolyte. During the simulation, therefore, we find that water and oxygen molecules leave the electrolyte and establish a gas phase.

Like in previous chapters, we utilized the DREIDING force field[21] and the F3C water model.[41] These force field parameters are described in the original papers[21, 41, 42] Our force field has the form:

$$E_{total} = E_{vdW} + E_Q + E_{bond} + E_{angle} + E_{torsion} + E_{inversion} \quad (1)$$

where E_{total}, E_{vdW}, E_Q, E_{bond}, E_{angle}, $E_{torsion}$ and $E_{inversion}$ are total energies, van der Waals, electrostatic, bond stretching, angle bending, torsion and inversion components, respectively.

The charge equilibration (QEq) method[70] optimized to reproduce the Mulliken charges of small molecules. The atomic charges of water molecule were from the F3C water model.[41]

For this study, the annealing and MD simulations were performed using the MD code LAMMPS (Large-scale Atomic/Molecular Massively Parallel Simulator) from Plimpton at Sandia[47, 48]. The equations of motion were integrated using the velocity Verlet algorithm[20] with a time step of 1.0 fs. The Nose-Hoover temperature thermostat[45, 46, 71] for the NVT and NPT MD simulations used a damping relaxation time of 0.1 ps and the dimensionless cell mass factor of 1.0. We annealed the system and allowed 5 ns of equilibration time. Then we collected the data from another 5 ns run.

Due to the large size and simulation time of system, our simulations were preformed at Keeneland at the Oak Ridge National Labs, a supercomputer cluster of GPU machines. Therefore, we used the CUDA modules of LAMMPS to exploit this architecture.

Our simulation box size was 51.3x51.91x509 Angstroms. The simulation box size was chosen so that a graphite sheet can fit unstrained in the x and y direction. For the z direction, our Nafion ionomer was around 100 angstroms thick, and the graphite layer was around 9 Å (0.335nm x 3). The remaining 400 Å were free volume. The electrode was a four layers of graphite, the bottom most layer being fixed and the topmost layer had a vacancy defect on it. The graphite had no charge on it. Then we placed a platinum cluster of 170 atoms, all with zero charge, on top of the defect on the top most layer of graphite. We found that a defect is necessary to anchor the Pt nanoparticle onto the graphite surface otherwise the particle drifts away from the electrode.

The amorphous hydrated Nafion was built in a separate simulation box and equilibrated for 5 ns. Then we copied it to our new simulation box. This was done to speed up the equilibration of the amorphous Nafion. The hydrated ionomer we introduced had a λ of 14. There were 16 Nafion chains, with a molecular mass of 11468 Da and ten sulfonate groups per chain. Our Nafion chains, therefore, have a similar equivalent weight to the commonly used Nafion 117 material (equivalent weight 1100g).

5-3. Results and Discussion

5-3.1 Analysis of Pt Nanoclusters.

We evaluated the energy of the Pt nanoparticles shown in Figure 30. In order to obtain their most probable energy state, we performed the spin-unrestricted calculations with various spin multiplicities. Some of the calculations are presented in Figure 31 in which the relative energies are calculated as the energy difference from the minimum energy and the optimal spin state. The optimal spin state is defined as a physically possible spin state which gives the lowest energy. After specifying the minimum energy value of Pt nanoparticle with the optimal spin state, we calculated the normalized cohesive energy (NCE) defined as:

$$NCE = \left[E\left(Pt_{X-Y-Z}[m]\right) - n \times E\left(Pt\right)\right] / n \quad (1)$$

where m and n denote the spin multiplicity and the total number of Pt atoms in the nanoparticle, and X, Y and Z denote the number of Pt atoms in the first, the second and the third layer of the nanoparticle, respectively. The sum of X, Y and Z is equal to n. $E(Pt_{X-Y-Z}[m])$ and $E(Pt)$ are the energies of the Pt nanoparticle and the single Pt atom, respectively.

In Figure 32, we summarize the NCEs calculated from the Pt nanoparticles shown in Figure 30. First, it is observed that the NCE decreases as a function of the number of Pt atoms in a nanoparticle, approaching the experimental value of NCE for bulk Pt (-5.8 eV).[229] As expected, the stability of the Pt nanoparticle increases with increasing particle size and the three different functionals converge to the asymptote in a similar manner.

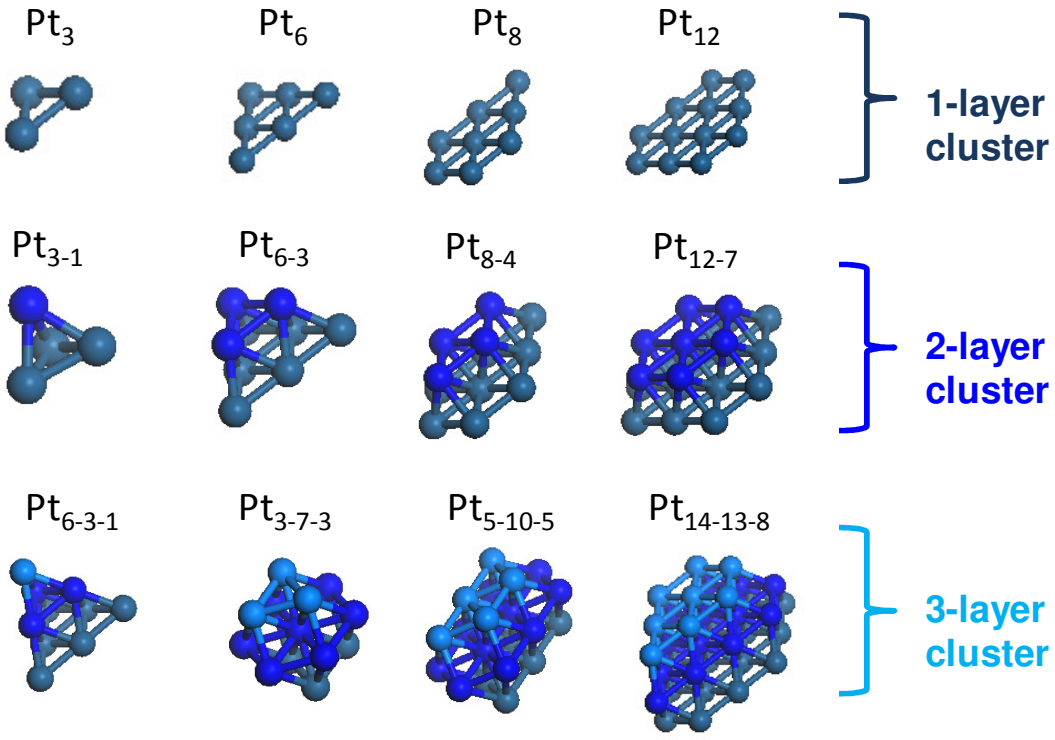

Figure 30: Various Pt nanoparticles ($Pt_{X\text{-}Y\text{-}Z}$) calculated in this study. X, Y and Z denote the number of Pt atoms in the first, the second and the third layer, respectively, of the nanoparticles. If the number of Pt in the layer is zero, it is not shown.

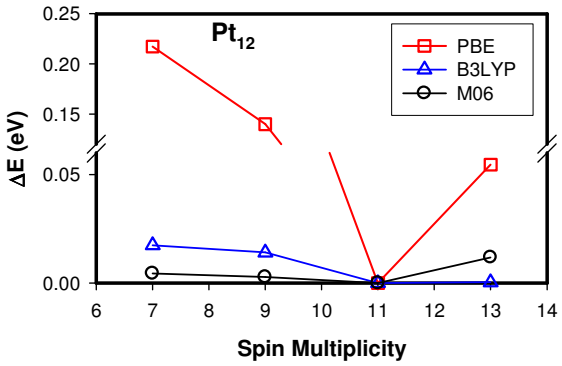

(a)

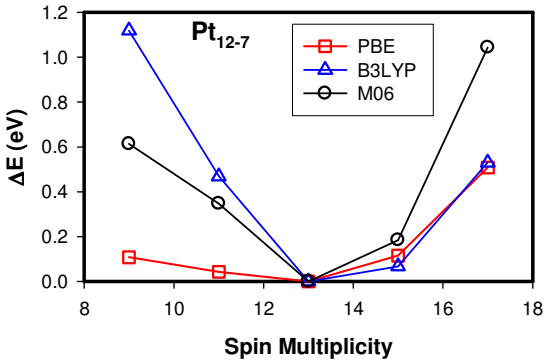

(b)

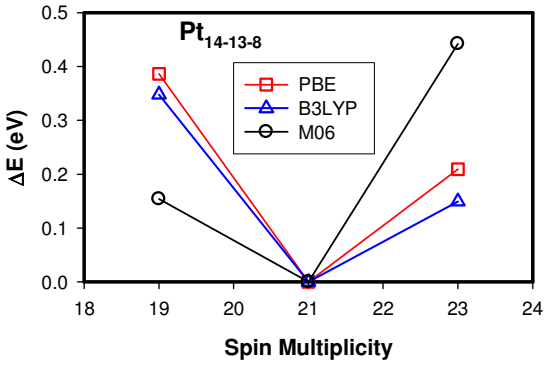

(c)

Figure 31: Change in relative energy of Pt nanoparticle as a function of spin multiplicity. The relative energy is the energy difference from the minimum energy with a optimal spin multiplicity. Other cases are not presented due to their similarity.

Although the general trend of the NCE is the same for all functionals we used in this study, it should be noted that the values of NCE are different depending on the functionals: NCE (PBE) < NCE (M06) < NCE (B3LYP). This indicates that PBE predicts the largest stabilization energy for the Pt nanoparticle, whereas B3LYP gives the lowest stability for the same Pt nanoparticle.

Binding energy differences amongst the functionals is expected since, so far, no functional fully describes the energy for a quantum system. Instead, functionals are built to describe certain systems well. PBE is widely used for metallic studies, and B3LYP is widely used for organic systems. M06, on the other hand, was designed specifically to describe the interaction between organic and metallic systems, including the dispersion energy. For purely metallic systems, therefore, we trust the PBE functional most, but we use M06 to describe the adsorption. Another point in Figure 32 is that the 2-layer and 3-layer Pt nanoparticles have nearly the same stability and the data points from these nanoparticles seem to be on an identical line for each functional, while the 1-layer nanoparticles are less stable with higher NCE since the Pt atoms in the 1-layer model lack the higher coordination with neighboring atoms. Our results agree with Sebetci's finding. [183]

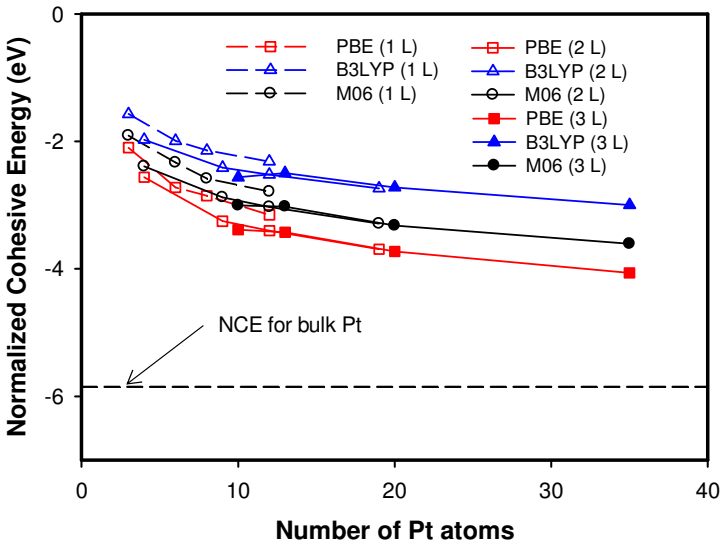

Figure 32: Change of atomic cohesive energy (ACE) with various layers as a function of the number of Pt atoms in a cluster. The ACE values of Pt clusters are higher than that of Pt in bulk Phase.

5-3.2 Coordination Number (CN) Model for Pt Nanoparticles.

Based on our DFT calculations for various Pt nanoparticles, we developed a model to evaluate the energy of Pt nanoparticle from its size and shape. The CN model is to predict the energetically stable state based on shape and size. It is an on-lattice model with constant bond lengths. It can be used to predict the formation energy of these types of clusters.

In general, however, the smallest clusters (few atoms) have the strongest and shortest bonds than the larger clusters and geometrically optimized larger structures provide more reasonable energy states for the clusters; however, considering off lattice geometries considerably increases the search space. Furthermore, since Pt clusters asymptotically approach the crystal lattice an on lattice model should describe most features.

Our model of the cluster energy classifies each atom according to the number of nearest neighbors. For example, a platinum atom inside a crystalline bulk has a CN of 12, while an atom on the (111) surface has a CN of 9. In our model, the energy of a cluster is the sum of the contribution of each atom. Each atom's contribution is determined uniquely by its CN.

For this purpose, we counted the CN of each atom for all the Pt nanoparticles (Figure 30 shows some of the 52 different clusters). An example in Figure 33a shows that $Pt_{6\text{-}3\text{-}1}$ nanoparticle has four Pt atoms with CN=3, three Pt atoms with CN=6, and three Pt atoms with CN=4. The atomic cohesive energy, $(ACE)_{CN}$, is determined by least squares fit of Eq (2) to the DFT CE.

$$CE = \sum_{CN=1}^{12} (ACE)_{CN} N_{CN}$$

(2)

where CE and N_{CN} denote the cohesive energy and the number of Pt atoms for each CN, respectively. A similar, but not identical, model for metallic clusters is known as the cluster expansion model, derived from the Ising spin model, and widely used especially for alloy systems. [185-189] The governing equation is shown in (3):

$$E_{CE}(\sigma) = N_{sites} + J_p \sum_i \sigma_i + \sum_{i,j} J_{ij} \sigma_i \sigma_j + \sum_{i,j,k} J_{ijk} \sigma_i \sigma_j \sigma_k + ...$$

(3)

Where E_{CE} is the cluster energy, N_{sites} is the number of available sites, the J terms are energy contribution terms and the σ, with a +1 or -1 value, represents the Ising spin state. In equation (3) we see that the cluster expansion model is a sum over all pairs in a cluster. By contrast our coordination number only considers the energy of the nearest neighbor, but considers the number of nearest neighbors.

In Figure 33b, we observe that the determined $(ACE)_{CN}$ decreases with increasing CN, along the line connecting two reference points (zero for CN=0 and 5.8eV for CN=12 whish is the experimentally reported formation energy [229]), which means that the stability of Pt atom in the nanoparticle increases with increasing the number of bonds (or the number of bonded neighboring atoms).

However, it should also be noted in Figure 33b that $(ACE)_{CN}$ has deviation from the line to have more negative numbers, which seems more distinct for lower CN. Considering that the dashed line between CN=0 and CN=12 predicts the stability of Pt atom increases

linearly as a function of CN by assuming that each bond has the constant strength regardless of the number of bonds, such negative deviation indicates that the bond strength is not constant, but decreases as a function of CN. In other words, the bond characteristics of a Pt with neighboring Pt atoms depends on the number of the neighboring Pt atoms. This interpretation could be clearly confirmed by displaying ACE/CN as a function of CN as also shown in Figure 33b: the contribution of individual Pt-Pt bond to ACE is the most significant for CN=1 and becomes weaker with increasing CN.

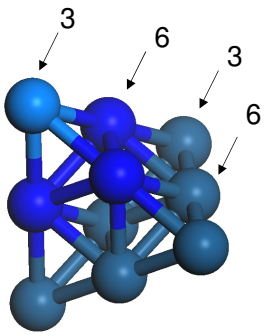

(a)

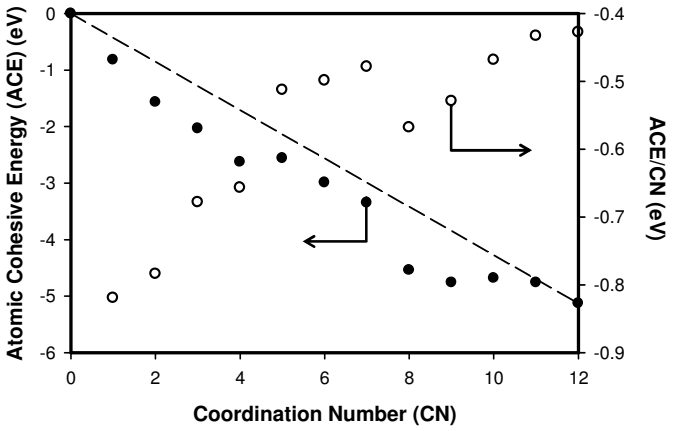

(b)

Figure 33: A Pt nanoparticle has atoms of various coordination number (CN): (a) For example, $Pt_{6\text{-}3\text{-}1}$ has 4 Pt atoms with CN=3 and 6 Pt atoms with CN=6; (b) Change in atomic cohesive energy of Pt as a function of coordination number (CN) reported in Table 11.

In order to validate our CN model in Eq. (2) with the atomic cohesive energy contributions of each CN in Table 11, we calculated the CE of new Pt nanoparticles that were not used in developing the CN model presented in Figure 34. As shown in Figure 34, the CN model predicts to at most 12% the correct cohesive energy. Note that the NCE, or CE divided by the number of atoms, is less than Pt's formation energy, as predicted by the simulation and the clusters system. This is reasonable since the particle is very small; only the first two Pt_{21} clusters have any CN=12 atoms. The remaining atoms are under coordinated surface and vertex atoms. As the clusters become larger, the proportion of bulk atoms increases and the NCE will approach Pt's formation energy.

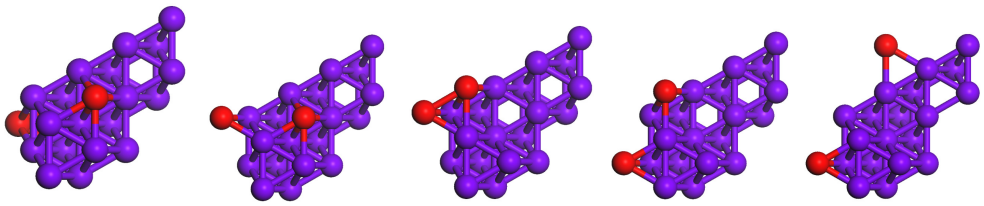

(a) (b) (c) d) (e)

Figure 34: Pt nanoparticles used to validate the CN model in Eq. (2). The number of Pt atoms are 21 for all cases, and the positions of the two red colored Pt atoms are determined to generate different CN.

In addition, we compared the surface energies calculated using the CN model with the value reported from literature. [184, 230-234] For this, we investigated several different facets such as (111), and (100) as shown in Figure 36.

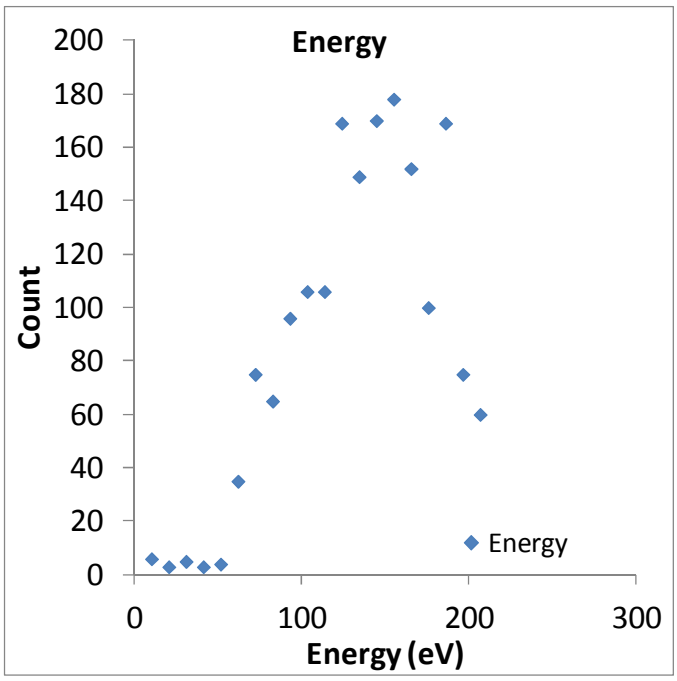

(a)

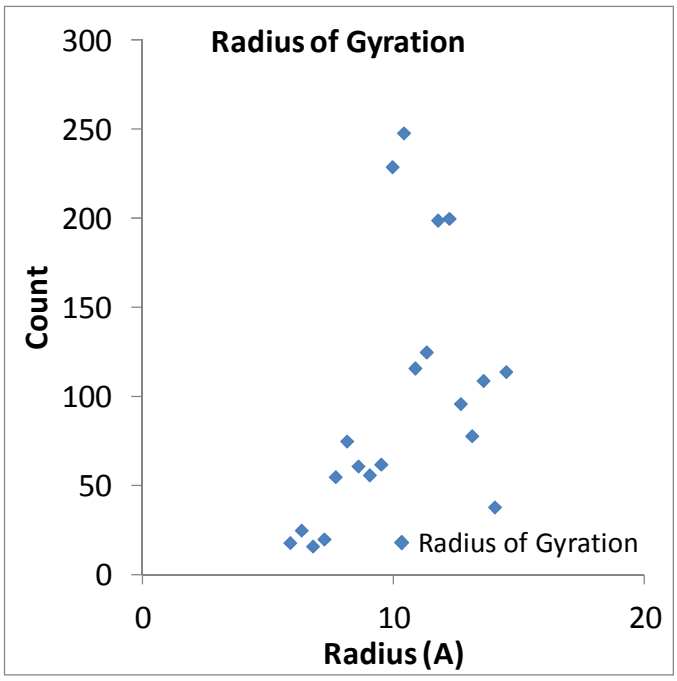

(b)

Figure 35: (a) Energy and (b) radius of gyration of a Pt cluster vs count from a MC simulation of a 95 atom cluster

Table 11: The atomic cohesive energy with respect to the coordination number. As expected, more coordinated atoms contribute more to form more stable Pt nanoparticles by lowering its cohesive energy

CN	1	2	3	4	5	6
Energy (eV)	-0.82	-1.57	-2.03	-2.63	-2.56	-2.99
CN	7	8	9	10	11	12
Energy (eV)	-3.35	-4.54	-4.76	-4.69	-4.76	-5.13

Table 12: Performance of CN model to predict surface energies and cluster CE

Surfaces	**CN bond model ($meV/Å^2$)**	**References ($meV/Å^2$)**
(111)	95.9	93,[184] 95,[230] 96,[231] 124,[232] 104,[233] 97[234]
(100)	129.2	116,[184] 114,[230]116,[231] 147[232]
Cluster	**CN bond model (eV/atom)**	**DFT (eV/atom)**
$Pt21_1$	-3.30	-3.04
$Pt21_2$	-3.25	-2.96
$Pt21_3$	-3.25	-2.95
$Pt21_4$	-3.25	-2.91
$Pt21_5$	-3.19	-2.85

These surface energies were obtained by characterizing the (111) and the (100) surfaces using our CN model. Therefore, a (111) surface is a surface of CN = 9 atoms, the (100) surface is a surface of CN = 8 atoms. Therefore, for the (111) surface we calculate the energy required to create a surface of CN =9 from a bulk of CN = 12 atoms. Although the CN model results are a little off from the reported DFT surface energies of the (100) surfaces, respectively, it seems that the CN model captures the surface energy reasonably well, especially for the (111) surface (Table 12), further validating our model.

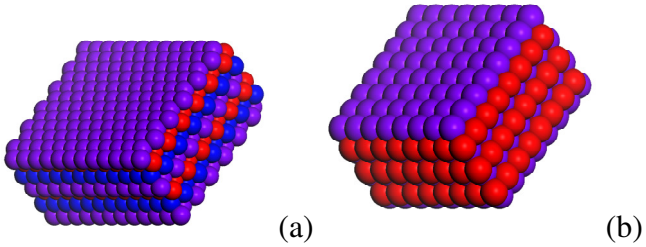

Figure 36: Pt surfaces with various facets.: (a) (111) direction; (b) (100) direction. The colors are introduced to clarify the structural repetition of the atomic layers.

In Figure 35, we show the results of using our model to generate the energy distribution and radius of gyration of a platinum cluster with 95 atoms. These are the results from a 10^7 step monte carlo simulation at T=0.025eV after several annealing steps. Only 1900 moves were accepted. From this data we calculated the mean radius of gyration of particle of 95 atoms as 6.2 Å. This calculation, needing 10 million steps to obtain a mere 1900 accepted states would be difficult using DFT with 95 atoms. Conversely, surface approaches are not accurate enough to properly describe the energy of such small cluster.

Finally, we used our model for purpose it was not intended for – to identify the most loosely . The DFT results for this calculation and the methodology to train our CN model were very different. In this calculation, we allowed the clusters to relax (geometric optimization), and we had graphite with a defect. All these features are absent in the CN model. However, as can be seen, the model still identifies the most loosely held atom, and the subsequent order of most tightly held atom. The model is even able to distinguish between two corner atoms who are formed by the intersection of the same planes. This is possible because the two atom's nearest neighbors' are different. Note that the energy predicted is not accurate, as expected since the cluster in our model is not allowed to relax.

Table 13: Energy of loosing an atom and the relative order.

	DFT (eV)	Order	CN model (eV)	Order
Lower corner	-2.46	1	-4.38	1
Lower edge	-3.02	2	-4.49	2
Top corner	-3.08	3	-5.16	3
Along edge	-3.61	4	-5.91	4
Top	-4.09	5	-7.97	6
Side face	-4.27	6	-7.55	5

5-3.3 Force Field Development

From the results above we used the Morse potential to obtain force fields of the interaction of the above molecular species with platinum. The form of the Morse potential is:

$$V(r) = D_e(1 - e^{-\alpha(r-r_e)})^2 \quad (4)$$

where D_e is the depth of the potential, α is the width and r_e is the equilibrium distance. The resulting force field fits are shown in the figures above. The parameters obtained are shown in Table 14. These parameters were developed with a pragmatic approach in mind, namely that the force field would include all the DFT interaction energy. To avoid the problems of mirror charges on the platinum surface moving as the charged atoms move, we set the charges of Pt to be fixed and equal to zero. The strong binding energy between platinum and the sulfonate and hydronium ions was absorbed into Morse Potential.

The resulting fits for all the species are well within a kT of the original DFT points on the graphs. For O_2 we did not fit the chemisorbed oxygen, just the physisorbed one. However, for completeness, in we report the physisorbed, the chemisorbed and the resulting fit to the physisorbed state.

Table 14: Force Field parameters for the ionomer moieties interacting with platinum using the Morse Potential function. The parameter α is unitless.

Pair	Depth (kcal/mol)	Re (Å)	α
Pt-C	0.34	4.48	1.54
Pt-F	0.204	3.67	5.99
Pt-S	3.04	3.41	2.15
Pt-O_{SO3}	2.35	2.51	1.02
Pt-O_{ether}	3.45	2.79	2.55
Pt-O_{O2}	0.430	3.47	1.01
Pt-O_{H2O}	2.50	2.416	2.40
Pt-H_{H2O}	1.36	3.05	1.60
Pt-$O_{hydronium}$	6.43	3.47	1.12
Pt-$H_{hydronium}$	0.24	1.61	3.73

5-3.4 Platinum Surface Analysis

The surface of the platinum nanocluster in our molecular dynamics simulation was characterized to measure what was on its surface. Specifically, we measured the percentage that each moiety in our MD simulation occupies on the Pt surface.

The measurement was done using the Connolly surface method.[235] This method uses a probe to measure the surface area of a molecule that is accessible to a sphere of radius r. For our purposes we used a 1.4 Å probe radius since this is the radius of a water

molecule. Water is the smallest molecule in our system that is electrochemically relevant, therefore, any space the water can access is electrochemically important. Using the Connolly surface method, we measure the contact area of a molecule on Pt. This area was defined as the area on the Pt surface that is no longer accessible by the probe due to another molecule on top of it. The results are shown in Figure 37 as percentages of the exposed Pt area. That is, we do not consider the area that is in contact with the electrode.

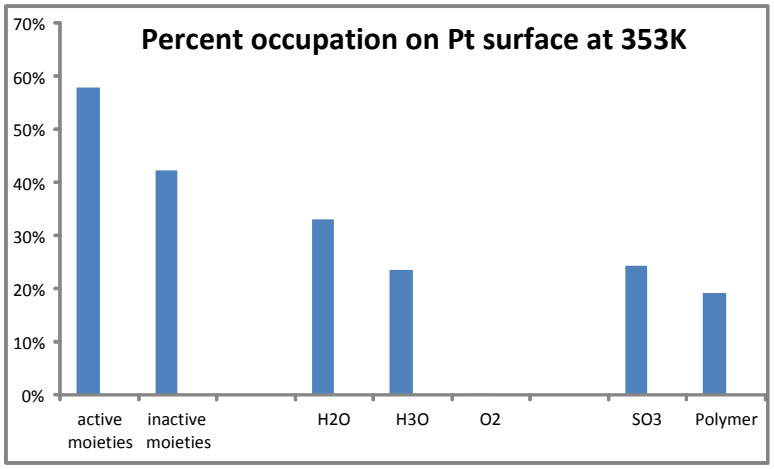

Figure 37: Percent occupation on the Pt170 surface

In the above graph, area occupied by water, hydronium and oxygen are considered electrochemically active, while the polymer segments are not. The measured electrochemically active area is 58% of the exposed Pt surface area. Experimentally reported values are very variable as it depends on many factors, and our value fits within the range of the reported values.[236-239] It must be kept in mind that the experimental value and our own value are very dependant on how the system is made. These differences can cause very large changes in the amount of surface area that a moiety occupies. Also, there is an error of around 5% in our measurement due to how the surface

area is assigned. Specifically, at the seams between two different moiety types, we measure an overlap in the surface area occupied by each moiety on the Pt surface. This is purely a measurement error, and the overlapped area is being double counted. To correct for this we assign the overlapping area proportionally. The overlap area is around 5% of any measurement. Finally, there is another source of area from the sulfonate ion. It is known that the sulfonate ion affects an area on the Pt surface larger than its Van der Waals radius. However, this is not captured in a classical MD simulation so it is not reflected here.

Our method can also measure the individual contributions from each moiety. Here we see that water occupies the largest share of the surface area. This is due to several factors including the strong dipole interaction with the surface, the water molecule's small size enabling it to occupy areas inaccessible to other moieties, and most significantly the larger number of water molecules in the system. Water's high occupancy is followed by the sulfonate ion and the hydronium ion. They are on the surface mostly due to their strong interaction with the Pt surface. The percentage they occupy is similar, probably due to the fact that they are counter-ions. The ionomer backbone occupies some area, despite it's weak interactions, probably due to sulfonate ions attached to it. Finally, there was no measured O_2 on the surface. Since oxygen molecules are present in small concentration, it is very expensive to add a significant amount of oxygen molecules to the simulation, therefore this last results is due to simulation error on account of the few oxygen molecules in the simulation system and subsequent high error of measurement.

5-4. Conclusion

Our overall goal is to study the role of Pt in the three phase region. Given the relative size of the three phase region, multiscale tools are required. That is, depending of the phenomenon and the size of the system, different tools should be employed. Therefore, DFT is suited for cluster stability, force field development and chemical dissolution studies. Molecular Dynamics, on the other hand, is more suited to investigate how all three phases of the catalyst layer interact with each other. In this study we presented our work on Pt cluster stability, developed a model to predict the energy of a cluster and predict which atoms in a cluster are more loosely held, and finally developed the force field for ionomer-Pt interaction. From this force field we created an MD simulation. Our coordination number model of cluster stability is used in our work to predict likely candidates for Pt dissolution, successfully. Our model is a consistent way to predict the atomic cohesive energy of an arbitrary Pt cluster of n atoms, constrained to the crystal structure. This model does not take lattice relaxation into account explicitly. It successfully predicts energies and likely atoms for dissolution.

The force field we developed was used to create a MD simulation to study the three phase region. In particular, we found the species that occupy the surface of a platinum cluster. Namely water occupies a plurality of the surface followed by the hydronium and sulfonate ions. These two occupy roughly the same amount of surface area since they are together.

Chapter VI

Conclusion

In our work the MD studies were used to investigate the structure of the membrane materials, the transport properties of the moieties, and the effect of acid strength of the membrane materials. Our density functional theory computations were used to solve the electron density and the energy of a set of Pt atoms. The energy obtained was used to obtain the binding energy to build a system and we used it to study the stability of the cluster models, and developed an energy model to accurately and quickly predict the energy of a cluster. Finally we studied the interaction between adsorbed species and a platinum cluster, developed a force field and found the amount of adsorbed species on a Pt cluster.

The issues that we wanted to understand is how the difference between different ionomers influence their properties; in particular their operating temperature, possible fuels, and the effect of acid strength. Also, we were interested in the catalyst due to its high cost and strong influence in the PEMFC's overall performance. In particular we wanted to develop a model of its stability and also its interaction with other species in the PEMFC.

6-1. Behaviour of S-PEEK at different water contents

Our first investigations were on S-PEEK (40 % of DS) with various water contents (10, 13 and 20 wt %) at 353.15 K. Although polymeric materials have a significant relaxation time, we equilibrated the S-PEEK membrane by using an annealing technique that gives the polymeric material the volume and kinetic energy to relax.

To characterize the nanostructure of S-PEEK, first, we calculated the pair correlation function for sulfur-sulfur pairs, $\rho g_{s\text{-}s}(r)$. This showed that the position of the first peak shifts from 4.4 Å at 10 wt % water content to 4.8 Å at 13 wt % to 5.4 Å at 20 wt % of water content, respectively. This result indicates that the sulfur-sulfur distance increases with increasing water content. By comparing the pair correlation function of sulfur-oxygen (water), $\rho g_{S-O(water)}(r)$, it was found that such increase in the sulfur-sulfur distance is due to the solvation of sulfonate groups by water molecules, and not just because of the overall swelling of the membrane. Added water preferentially surrounded the sulfonate ion.

Analyzing $\rho g_{S-O(water)}(r)$ and $\rho g_{S-O(hydronium)}(r)$, we found that the water coordination number of sulfonate increases from 2.8 to 4.6 with increasing water content, whereas the coordination number of hydronium for sulfonate decreased from 1.4 to 0.9. We noted if the coordination number of hydronium surrounding sulfonate is greater than one this implies that sulfonate group share hydroniums. By increasing the water content, the sulfonate groups move further apart (as evidenced by the S-S $g_{s\text{-}s}(r)$), and this eliminates the possibility of hydronium sharing by the sulfonates. Although higher water content

improves proton conductivity, this separation of the sulfonate groups and drop in the CN must have negative implications for proton transport. If sulfonates are far apart, protons will be in a high potential energy region when going from one sulfonate to the next. This is because the H_3O^+ needs to close to a counter ion due to their charge-charge interaction.

The $\rho g_{O(water)-O(water)}(r)$ was also analyzed as a function of water content. By increasing the water wt%, the CN of water increases getting closer to the bulk value. Therefore, the water in the water phase becomes more bulk-like. However, this is not as pronounced as Nafion; this is because the S-PEEK backbone is more rigid and, most importantly, significantly less hydrophobic than the perfluorinated Nafion backbone.

The water diffusion coefficients were calculated from the final 5 ns of our NPT simulations. We found that water diffusion increases with increasing water content, which was observed in previous simulations of hydrated Dendrion membranes. The water weight dependence of diffusion is consistent with our findings found using pair correlation. There we proved that added water goes to the existing water channels and around the sulfonate groups. There the added water molecules screen the sulfonate and hydronium interaction with other water molecules allowing them more freedom to move.

6-2. Behaviour of S-PEEK at different temperatures

We also investigated the effect of temperature on the structure and water transport of S-PEEK. We limited ourselves to two different water contents (10wt% and 20wt%) and three temperatures.

Unlike for changes in water content, the pair correlations for sulfur - sulfur, sulfur - water and sulfur - hydronium pairs did not change as a function of temperature. This is attributed to the rigidity of the S-PEEK chain and that it has a direct attachment of its sulfonate groups. By calculating the structure factor, the nanophase-segregated structures of the hydrated S-PEEK membrane was found. This showed that while characteristic dimension does not significantly changed as a function of temperature, the concentration contrast between the hydrophilic and hydrophobic moieties becomes greater with increasing water content. This confirms our result that added water preferentially goes to the water phase near the sulfonates.

While the previous metrics did not have a strong temperature effect, we found a stronger effect of temperature on the pair correlation of water – water. We found that the internal structure of the water phase is more bulk like with decreasing temperature and increasing water content. This is evidenced by the water coordination number becoming larger. This has implications for proton transport since closely packed water molecules are a better path for proton conduction.

The diffusion coefficient of water is larger at higher temperatures and follows the Arrhenius equation. Also, it increases with increasing water content. The calculated

activation energy of water diffusion was obtained: 25.7 kJ/mol and 24.9 kJ/mol for 10 wt % and 20 wt %, respectively. The activation energy is only slightly reduced with increasing water content. This implies that the diffusion mechanism is similar with changes in water content: the disruption that a diffusing water molecule causes to the water bonding network is similar with different water contents. Despite the similar activation energy for water diffusion, an overall higher water diffusion coefficient is obtained for larger water content, implying that D_o is higher. Compared to bulk water (13.2 kJ/mol) and water in Nafion (16.7-18.9 kJ/mol), we found that less phase segregated S-PEEK has a higher activation energy.

6-3. Effect of acid strength on sPS

A polystyrene-based sulfonate ionomers was prepared by attaching a superacidic fluoroalkyl sulfonic acid, a less acidic aryl sulfonic, and a alkyl sulfonic acids to the backbone. With this set of polymers, a comprehensive study on the effect of acid strength on the proton conductivity of the sulfonated ionomers was prepared. Despite its lower water uptake and IEC, the fluoroalkyl sulfonated superacidic ionomer (sPS-S_1) maintained higher proton conductivity at low RH compared with the less acidic aryl and alkyl sulfonated ionomers (sPS-S_2 and sPS-S_3), and this difference in proton conductivity gradually increased as the RH decreased. The water uptake behavior as a function of RH and the morphology studies show that, compared to the less acidic ionomers sPS-S_3, the superacidic sulfonate groups of sPS-S_1 attract more water and creates enlarged hydrophilic domains.

To understand this we conducted a comparative computational studies of sPS-S_1 and sPS-S_3 under hydrated conditions to investigate the effects of acidity at a molecular level. By analyzing the solvation of the sulfonate groups with water in each system, we confirmed that the sulfonate groups in sPS-S_1 are better solvated than those in sPS-S_3. Thus, the acidity effect not only increases the dissociation of protons from the sulfonate, but also causes more solvated sulfonate groups as seen by the large number of water surrounding the sulfonate groups. Due to the superacid solvation effect, sPS-S_1 has a higher calculated water diffusion coefficient and proton diffusion coefficient than sPS-S_3. Furthermore their difference in proton diffusion was greatest at lower water content.

Overall, our studies on the effect of acid strength on fuel cell membrane properties suggest a clear relationship between acid strength and proton conductivity. The enhanced proton conductivity of the more acidic ionomer is due, not only to the higher dissociation of the super acid, but also to the better solvation of the sulfonates.

Compared to S-PEEK, the results of s-PS are very interesting because of the observed good proton conductivity of the (sP-S_1) even at low levels of hydration. This implies that membranes can have good proton conductivity at low hydration. While S-PEEK's proton transport is poor compared to Nafion, this is because the water channel is not developed enough.

Our previous S-PEEK study demonstrated the differences in morphology and therefore properties with Nafion. In general we found that added water aids proton transport, but in our s-PS study we see that similar effects are obtained by having a stronger acid. In general it is possible to achieve many of the improvements generally seen with increased

water weight by using a stronger acid instead. By using a stronger acid in lieu of increased water weight, the operating temperatures and fuel characteristics of the membrane should improve.

6-4. Interaction of Platinum Nanoparticles in a Three Phase System

DFT is suited to study cluster stability, force field development and chemical dissolution studies. Molecular Dynamics, on the other hand, is more suited to investigate how all three phases of the catalyst layer interact with each other. Here, we presented our work on Pt cluster stability, developed a model to predict the energy of a cluster and predict which atoms in a cluster are more loosely held, and finally developed the force field for ionomer-Pt interaction.

Our coordination number model is an on lattice model that models the cohesive energy of a particle by considering only each atom's nearest neighbors. It is similar to cluster expansion models that have been used by other researchers. It found that the bond of low coordinated atoms are stronger, but because there are less of them overall the atom, is more loosely held.

The coordination model was built to predict the energies of various clusters. This model is needed because for larger cluster QM takes a significant amount of time. Our model provides a quick, high quality, estimate of the energy and, there, identify the most loosely held atoms.

Finally, the interaction energy and nature of their bond of various moieties of an ionomer system were found. In particular we found that H22o and SO2 are strongly bound to the catalyst surface due to changes in the metal's surface electronic state. Therefore, we developed a force field of these interaction that can be used in future MD simulations.

Using this work we built a molecular dynamics simulation of the three phase region between the graphite, catalyst and electrolyte. The catalyst was built using the CN model developed. Since the CN model predicts the energy of a cluster, it can be used in a Monte Carlo simulation to generate a set of clusters belonging to the desired thermodynamic ensemble. The interaction between the cluster and the various moieties in the electrolyte were then modeled with the force field developed.

Questions that can be answered with these simulations include confirmation of how the electrolyte binds to the catalyst. Using cyclic voltametry there has been recent work indicating that the sulfonate binds to the catalyst, but there had been no clear picture of how the rest of the ionomer interacts. In particular the perfluorinated part of the Nafion chain is of interest to researchers. Also, due to the large size of the sulfonate group, it is interesting to study how much surface area on the catalyst the sulfonate occupies. This picture is complicated by the presence of water which allows hydroniums to reach the catalyst surface. By performing an MD simulation we showed that water occupies most of a Pt surface, followed by the sulfonate and hydronium ions. The backbone occupies a small amount of surface area, due to its link to the sulfonate group

Finally, this work could also be used to study the diffusion of platinum oxides in the electrolyte region. Although there is some debate as to the nature of the oxide, both likely

candidates, PtO_2 and $Pt(OH)_2$ can be added to the simulation cell. The transport properties of the dissolved platinum can be used understand how to limit the dissolution of platinum.

Appendix A

Experimental details of the sPS synthesis

The following explains the procedures used by our experimental partner in the synthesis of the polymer used in Chapter 4. It is included for completeness and was previously published by our partner in the paper we co-wrote. [108]

Materials and Methods. 4,4'-Di-*tert*-butyl-2,2'-dipyridyl (d*t*bpy), chloro-1,5-cyclooctadiene iridium(I) dimer ($[IrCl(COD)]_2$), tetrakis(triphenylphosphine)palladium(0) ($Pd(PPh_3)_4$), 4-dimethylaminopyridine (DMAP), $Na_2S_2O_4$, 3,5-dimethylphenol, and 4-bromobenzenesulfonyl chloride were reagent grade and used without further purification. Bis(pinacolato)diboron (B_2pin_2) from Frontier Scientific Co., ICF_2CF_2I from Oakwood Products, Inc, $BrCF_2CF_2Br$ from SynQuest Labs, Inc., Chlorine gas from Praxair Inc., CFC-113 from ChemNet were used as received. Cyclooctane was dried using sodium and benzophenone, distilled under vacuum, and stored in a nitrogen-filled glove box. sPS (M_w = 140.9 kg/mol with M_w/M_n = 2.90) was obtained from LG Chemical Ltd., Daejeon, S. Korea and used as received. Anhydrous tetrahydrofuran (THF) was obtained from EMD Chemicals and collected from the container using a positive pressure of nitrogen.

^1H, ^{19}F, and ^{13}C NMR spectra were obtained using a Varian NMR spectrometer (400 MHz for ^1H, 376 MHz for ^{19}F, and 100 MHz for ^{13}C) at room temperature and chemical shifts were referenced to TMS (^1H and ^{13}C) and $CFCl_3$ (^{19}F). GC/MS analysis was conducted using a Shimadzu QP2010S equipped with a 30 m × 0.25 mm SHR-XLB GC

column and an EI ionization MS detector. FT-IR spectra were recorded on a Shimadzu IR Prestige-21.

Ion Exchange Capacity (IEC). The calculated IECs of sPS ionomers were estimated from the mol% of 3,5-dimethylphenol protected sulfonated sPS in the ^{1}H NMR spectra. The experimental IECs of sPS ionomers were determined using a titration method. Membranes were equilibrated in 2 M NaCl solution at room temperature for 3 days before titration. The protons released into the aqueous solution were titrated with 0.025 M NaOH solution using phenolphthalein as an indicator. The experimental IEC values of the sPS ionomer membranes were calculated according to the equation below:

$$\text{IEC (meq/g)} = M_{\text{NaOH}} \times V_{\text{NaOH}} / W_{\text{dry}} \tag{1}$$

where M_{NaOH} and V_{NaOH} are the molar concentration and volume (mL) of the aqueous NaOH solution used in titration, W_{dry} (g) is the weight of dry membrane.

Water Uptake and Hydration Number (λ). Water uptake was measured as a function of relative humidity at 30 ºC using a TA Instruments Q5000SA dynamic vapor sorption analyzer. The relative humidity steps and equilibration times were the same those used in the conductivity experiments. Hydration number (λ) was calculated from:

$$\lambda = \left(\frac{W_{RH} - W_{dry}}{18.01} \right) \left(\frac{1000}{W_{dry} \cdot IEC} \right)$$

(2)

where W_{RH} is the sample mass at a given RH, W_{dry} is the dry mass of the sample, and IEC is the ion exchange capacity of the sample in milliequivalents of sulfonate group per gram of polymer.

Proton Conductivity. To measure proton conductivity of sPS ionomers, the membrane in sulfonic acid form was immersed in deionized water for at least 24 h. The proton conductivity of the membrane was measured using a four-electrode method with a BT-512 membrane conductivity test system (BekkTech LLC). The proton conductivity was measured by changing the relative humidity from 20 to 100% at 80 ^{o}C. RH control started from 70%, stabilized for 2 hr, decreased to 20% at a rate of 10% RH/20 min, then increase to 100% at a rate of 10% RH/20 min. The proton conductivity data was collected from the cycle of 20% RH to 100% RH. The proton conductivity was calculated according to the following equation:

$$\sigma\ (\text{mS/cm}) = \frac{L}{R \times W \times T}\frac{1}{\rho} = \frac{\text{L}}{\text{RQUOT}}$$

(3)

where L is the distance between the two inner platinum wires (0.425 cm), R is the resistance of the membrane, W and T are the width and the thickness of the membrane in centimeters, respectively.

Membrane Morphology. Membranes in acid form were stained by soaking in 0.5 M lead acetate solution at room temperature for 1 day, then rinsed with deionized water and dried under vacuum at room temperature overnight. The stained membranes were cut into small pieces and embedded in Spurr's epoxy resin and cured overnight at 70 ^{o}C. The samples were sectioned to yield slices of 100 nm thick using Leica EM UC6 ultramicrotome and placed on copper grids. Transmission electron microscopy images were taken by TECNAI-F30 Super-twin TEM using an accelerating voltage of 300 kV. The phase segregation of membranes was characterized by AFM. Acid form of membranes were soaked in water for 12 hr, dried at 60 ^{o}C for 30 min, then exposed to ambient conditions for > 6 hr before the characterization. A Veeco Metrology D3000 microscope with a Nanoscepe IIIa controller with standard commercially available SFM 125 micron long silicon cantilevers with a spring constant of about 40 N/m was used to obtain all images. Identical operating conditions, i.e. cantilever drive amplitude and set point were employed for all aromatic membranes.

Synthesis of 3,5-dimethylphenyl 2-(4-bromophenoxy)tetrafluoroethanesulfonate ester (S_1). 3,5-Dimethylphenol (3.10 g, 25.4 mmol, 1.1 equiv) and CH_2Cl_2 (70 mL) were added to a 250 mL two-neck flask filled with nitrogen and was cooled to 0 ^{o}C. 2-(4-Bromophenoxy)tetrafluoroethanesulfonyl chloride (8.57 g, 23.1 mmol), which was prepared from 4-bromophenol in 61% overall yield using literature method,[240] and DMAP (3.38 g, 27.7 mmol, 1.2 equiv) were added in sequence and the mixture was stirred at 0 ^{o}C for 2 h and room temperature for 12 h. The reaction mixture was diluted with CH_2Cl_2 (80 mL), washed with 2 M HCl (40 mL × 3), saturated $NaHCO_3$ (40 mL) and brine (30 mL), and combined organic layer was dried over $MgSO_4$. After evaporation

of solvent, resulting crude product was purified by column chromatography (hexane/ethyl acetate=10:1) to give 9.66 g of S_1 as an yellowish oil (92% yield). ^{1}H NMR ($CDCl_3$): δ 7.52 (d, J = 8.8 Hz, 2H), 7.13 (d, J = 8.8 Hz, 2H), 6.99 (s, 1H), 6.92 (s, 2H), 2.25 (s, 6H). ^{19}F NMR ($CDCl_3$): δ –81.4 (t, J = 4.3 Hz, O$\underline{CF_2}$), –112.5 (t, J = 4.3 Hz, $\underline{CF_2}SO_3$). ^{13}C NMR ($CDCl_3$): δ 150.0, 147.5, 140.4, 133.1, 129.9, 123.8, 120.7, 119.2, 115.8 (tt, $^1J_{CF}$ = 277 Hz, $^2J_{CF}$ = 28.6 Hz), 113.9 (tt, $^1J_{CF}$ = 298 Hz, $^2J_{CF}$ = 39.1 Hz), 21.4. GC/MS: 458, 456, 392, 192, 143, 121 (100%), 91, 77. HRMS (*m/z*) (CI, NH_3): calc. for $C_{16}H_{13}O_4BrF_4S$ $(M+NH_4)^+$ 473.9992, found 473.9996.

Synthesis of 3,5-dimethylphenyl 4-bromobenzenesulfonate ester (S_2). 4-Bromobenzenesulfonyl chloride (20.0 g, 78.3 mmol), 3,5-dimethylphenol (9.56 g, 78.3 mmol), and DMAP (10.5 g, 86.1 mmol, 1.1 eq) were placed in a 500 mL two-neck flask under nitrogen. CH_2Cl_2 (250 mL) was added and the resulting mixture was stirred overnight at room temperature. The reaction solution was washed with 2 M HCl solution (50 mL × 2), saturated $NaHCO_3$ solution (50 mL) and brine (50 mL), dried over Na_2SO_4, and evaporated. Crude product was purified by column chromatography (ethyl acetate/hexane: 1/10 to 3/10) to give 26.4 g of S_2 as an off-white solid product (94% yield). ^{1}H NMR ($CDCl_3$): δ 7.69 (distorted doublet, J = 8.0 Hz, 2H), 7.58 (distorted doublet, J = 8.0 Hz, 2H), 6.89 (s, 2H), 6.61 (s, 1 H), 2.25 (s, 6H). ^{13}C NMR ($CDCl_3$): δ 149.3, 139.7, 134.7, 132.3, 129.9, 128.3, 128.9, 119.6, 21.1. GC/MS: 342, 340, 248, 221, 155, 121 (100%), 109, 91, 77, 65, 50, 41. HRMS (*m/z*) (CI, NH_3): calc. for $C_{14}H_{13}O_3BrS$ $(M+NH_4)^+$ 358.0107, found 358.0115.

Preparation of 3,5-dimethylphenyl 3-(4-bromophenoxy)propanesulfonate ester (S_3). 4-Bromophenol (5.0 g, 28.9 mmol) and K_2CO_3 (12.0 g, 86.7 mmol, 3 equiv) were placed in

a 100 mL two-neck flask under nitrogen, and DMF (50 mL) and 1,3-propanesultone (4.59 g, 37.6 mmol, 1.3 equiv) were added. The mixture was stirred at 110 ^{o}C overnight and cooled to room temperature, and the resulting precipitate was filtered. The filtered solid was stirred with water (200 mL) for 1 h at room temperature, filtered and dried in air to give 5.83 g of potassium 3-(4-bromophenoxy)propanesulfonate as a white solid (61% yield). ^{1}H NMR (DMSO-d_6): δ 7.42 (d, J = 8.8 Hz, 2H), 6.89 (d, J = 8.8 Hz, 2H), 4.04 (t, J = 6.6 Hz, 2H), 2.53 (t, J = 7.2 Hz, 2H), 1.98 (m, 2H). ^{13}C NMR (DMSO-d_6): δ 157.9, 132.1, 116.8, 111.7, 67.0, 47.8, 25.1. Potassium 3-(4-bromophenoxy)propanesulfonate (1.73 g, 5.46 mmol) was added to a 50 mL two-neck flask under nitrogen, and acetonitrile (17 mL) and phosphorus oxychloride (4.18 g, 27.3 mmol, 5 equiv) were added subsequently. The reaction mixture was stirred at 85 ^{o}C overnight, cooled to room temperature, poured into ice water (~60 g), and extracted with CH_2Cl_2 (30 mL × 3). Combined organic layer was dried over Na_2SO_4, and evaporation of solvent gave 1.45 g of 3-(4-bromophenoxy)propanesulfonyl chloride as an off-white solid (85% yield). ^{1}H NMR (DMSO-d_6): δ 7.42 (d, J = 9.2 Hz, 2H), 6.89 (d, J = 8.8 Hz, 2H), 4.04 (t, J = 6.4 Hz, 2H), 2.64 (t, J = 7.6 Hz, 2H), 2.00 (m, 2H). ^{13}C NMR (DMSO-d_6): δ 158.0, 132.2, 116.9, 111.9, 66.7, 48.0, 24.9. 3-(4-Bromophenoxy)propanesulfonyl chloride (1.44 g, 4.59 mmol) and 3,5-dimethylphenol (0.51 g, 4.17 mmol, 0.91 equiv) were added to a 50 mL two-neck flask under nitrogen and CH_2Cl_2 (15 mL) and DMAP (0.56 g, 4.59 mmol, 1 equiv) were added in sequence. The resulting solution was stirred overnight at room temperature, diluted with CH_2Cl_2 (50 mL), washed with 2 M HCl (20 mL × 2), and dried over Na_2SO_4. After evaporation of solvent, crude product was purified by column chromatography (ethyl acetate/hexane: 1/10 to 2/10) to give 1.65 g of S_3 as a white solid

(99% yield). ^{1}H NMR ($CDCl_3$): δ 7.39 (d, *J* = 8.8 Hz, 2H), 6.94 (s, 1H), 6.88 (s, 2H), 6.77 (d, *J* = 8.8 Hz, 2H), 4.11 (t, *J* = 5.6 Hz, 2H), 3.47 (t, *J* = 7.6 Hz, 2H), 2.45 (m, 2H), 2.32 (s, 6H). ^{13}C NMR ($CDCl_3$): δ 157.6, 149.2, 140.2, 132.6, 129.2, 119.6, 116.4, 113.6, 65.5, 47.4, 24.1, 21.4. GC/MS: 400, 398, 227, 185, 174, 157, 134, 121 (100%), 105, 91, 77, 65, 41.

Preparation of sPS-Bpin (40 mol%). In a nitrogen-filled glove box, sPS (700 mg, 6.73 mmol polystyrene repeating unit), B_2pin_2 (1.37 g, 5.38 mmol, 0.8 equiv), $[IrCl(COD)]_2$ (54.2 mg, 3 mol% iridium based on the amount of B_2pin_2), d*t*bpy (43.3 mg, 3 mol% based on the amount of B_2pin_2), cyclooctane (4.30 g, 0.40 mol, 60 equiv), and a magnetic stirring bar were placed into a 30 mL vial and capped with a Teflon-lined septum. The vial was removed from the glove box and placed in an oil bath at 150 ºC for 6 h. After cooling to room temperature, the solution was diluted with chloroform (60 mL) and filtered through a short plug of silica gel to remove the catalyst. The filtrate was concentrated by a rotary evaporator to about 10 mL, and cold methanol (100 mL) was added to precipitate polymer. The dissolution and precipitation process was repeated one more time. The borylated polymer was isolated as a white solid and dried under vacuum at 80 ºC (1.04 g, 148% yield based on polymer weight). ^{1}H NMR (benzene-d_6): δ 8.00 (H_{arom} from C_6H_4-Bpin), 7.73 (H_{arom} from C_6H_4-Bpin), 7.08 (H_{arom}), 6.71 (H_{arom}), 2.09 (CH of sPS backbone), 1.49 (CH_2 of sPS backbone), 1.16 (CH_3 of Bpin). Based on analysis of ^{1}H NMR spectrum, an average of 40% of polymer repeating unit contains Bpin group.

Preparation of 3,5-dimethylphenyl protected sulfonate of sPS-S_1, sPS-S_2, and sPS-S_3. sPS-Bpin (100 mg of 40 mol% Bpin functionalized sPS, 0.250 mmol Bpin) and K_3PO_4

(0.240 g, 1.13 mmol, 4.5 equiv) were placed in a 25 mL vial and capped with a Teflon-lined septum. Tetrakis(triphenylphosphine)palladium (11.6 mg, 0.01 mmol, 4 mol%) and THF (4 mL) were added to the vial in a nitrogen-filled glove box and the vial was removed from the glove box. Compound S_1 (230 mg, 0.50 mmol, 2 equiv) and water (0.4 mL) were added using syringes. The solution was stirred at 80 ^{o}C for 12 h, cooled to room temperature, diluted with chloroform (40 mL), and filtered through a short pad of silica gel. The filtrate was concentrated to about 3 mL and cold methanol (10 mL) was added to precipitate the polymer. Another cycle of dissolution in chloroform and precipitation with cold methanol provided 140 mg of 3,5-dimethylphenol protected sulfonate form of sPS-S_1 as a white solid. ^{1}H NMR (benzene-d_6): δ 6.62–7.20 (multiple H_{arom}), 2.18 (CH of sPS backbone), 1.97 (CH_3), 1.59 (CH_2 of sPS backbone). ^{19}F NMR (benzene-d_6): δ –80.3 (s, 2F, –O$\underline{CF_2}$), –111.9 (s, 2F, $\underline{CF_2}SO_3$–)

The same procedure above with compound S_2 produced sPS-S_2 in 3,5-dimethylphenol protected sulfonate form. ^{1}H NMR (benzene-d_6): δ 6.56–8.00 (multiple H_{arom}), 2.03 (CH of sPS backbone), 1.93 (CH_3), 1.55 (CH_2 of sPS backbone).

The same procedure above with compound S_3 produced sPS-S_3 in 3,5-dimethylphenol protected sulfonate form. ^{1}H NMR (benzene-d_6): δ 6.56–7.50 (multiple H_{arom}), 3.53 (O$\underline{CH_2}CH_2CH_2SO_3$), 3.09 ($OCH_2CH_2\underline{CH_2}SO_3$), 2.12 (CH of sPS backbone and $OCH_2\underline{CH_2}CH_2SO_3$), 1.97 ($CH_3$), 1.52 ($CH_2$ of sPS backbone).

Preparation of sodium sulfonate form of sPS-S_1, sPS-S_2, and sPS-S_3. Above 3,5-dimethylphenol protected sulfonate form of sPS-S_1 (100 mg of 40 mol% sulfonated sPS; 0.158 mmol sulfonate) was dissolved in dioxane (4 mL) with gentle heating and NaOH

(50.6 mg, 1.26 mmol, 8 equiv) and H_2O (40 μL) were added. The resulting solution was stirred at 100 °C for 4 h. After cooling to room temperature, solvent was evaporated and residue was dissolved in methanol, filtered through a short plug of silica gel. After concentration of the filtrate, addition of H_2O (20 mL) caused precipitation of polymer which was filtered and washed with a refluxing solution of water/methanol (3/1, v/v) for 2 h. Drying under vacuum at 80 °C for 12 h gave 87 mg of polymer product. ^{1}H NMR (DMSO-d_6) δ: 6.80–8.10 (multiple H_{arom}), 1.61 (CH of sPS backbone), 1.23 (CH_2 of sPS backbone). ^{19}F NMR (DMSO-d_6) δ: –80.4 (s, O$\underline{CF_2}$), –116.2(s, $\underline{CF_2}SO_3$).

The above procedure was used for preparation of sodium salt form of sPS-S_2. The obtained polymer product was purified by stirring in hot methanol for 2 h. Yield: 87 % based on recovered polymer weight. ^{1}H NMR (DMSO-d_6): δ 6.43–7.64 (multiple H_{arom}), 1.63 (CH of sPS backbone), 1.28 (CH_2 of sPS backbone).

The above procedure was used for preparation of sodium salt form of sPS-S_3. The obtained polymer product was purified by stirring in hot methanol for 2 h. Yield: 86 % based on recovered polymer weight. ^{1}H NMR (DMSO-d_6): δ 6.30–7.50 (multiple H_{arom}), 4.00 (O$\underline{CH_2}CH_2CH_2SO_3$), 2.54 ($OCH_2CH_2\underline{CH_2}SO_3$), 1.98 ($OCH_2\underline{CH_2}CH_2SO_3$), 1.62 (CH of sPS backbone), 1.22 (CH_2 of sPS backbone).

Acid form membrane preparation of sPS-S_1, sPS-S_2, and sPS-S_3. Sodium sulfonate form of sPS ionomers (300 mg) was dissolved in DMSO (3 mL) and casted on a glass plate. The film was dried at 40 °C under a positive air flow for 24 h and then at 80 °C under vacuum for 12 h. The acid form membrane was obtained by immersing the membrane in 1 M H_2SO_4 for 3 days (during which time the solution was changed every

day) at room temperature, followed by immersing in deionized water for 1 day (water was changed several times).

Synthesis of Ionomers

Synthetic Strategy for Sulfonated Ionomers. The synthesis of sulfonated sPS ionomers functionalized with different sulfonic acid groups is summarized in Scheme 1, Figure 38. The synthetic strategy is based on sequential reactions of (i) iridium-catalyzed borylation of the aromatic C–H bonds of sPS, (ii) palladium-catalyzed Suzuki–Miyaura cross-coupling reactions of borylated sPS (sPS-Bpin) with phenyl bromides that contain different sulfonate precursor groups (S_1, S_2, S_3 in Scheme 1), and (iii) removal of the protecting group from the sulfonates and subsequent acidification.

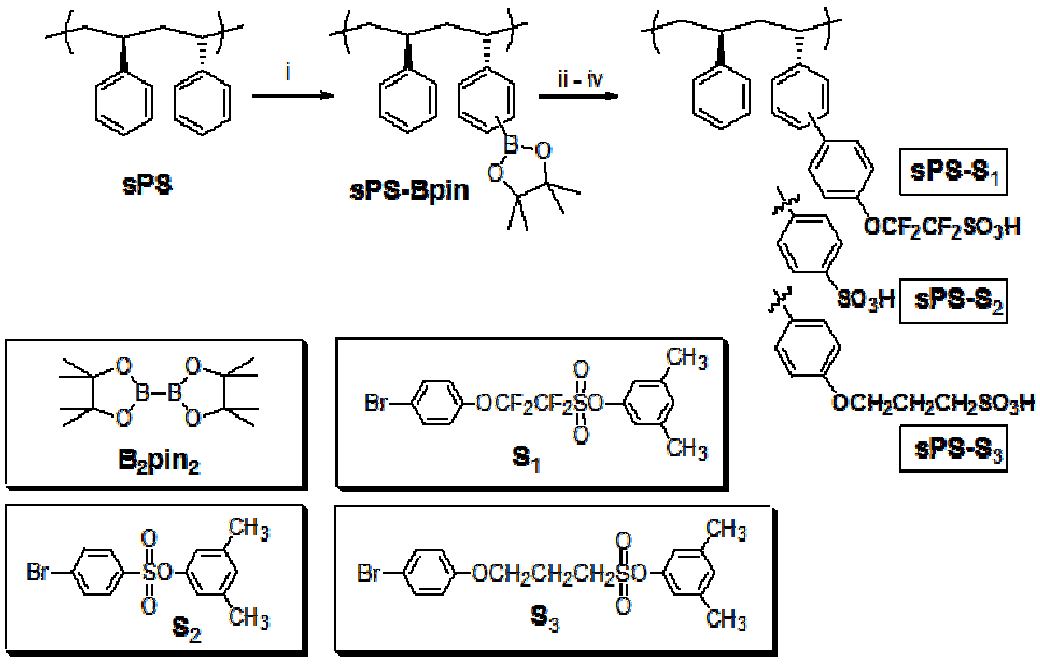

Figure 38: Scheme 1. Synthesis of syndiotactic polystyrene ionomers functionalized with different sulfonic acid groups.[a]

[a]Reagents and conditions: (i) B_2pin_2, $[IrCl(COD)]_2$ (1.5 mol%), d*t*bpy (3 mol%), cyclooctane, 150 ºC, 6 h; (ii) S_1, S_2, or S_3 (2 equiv), $Pd(PPh_3)_4$ (4 mol%), K_3PO_4 (4.5 equiv), THF/H_2O (10/1), 80 ºC, 12 h; (iii) NaOH (8 equiv), dioxane/H_2O, 100 ºC, 4 h; and (iv) 1 M H_2SO_4.

Three examples of sulfonated sPS ionomers containing fluoroalkyl sulfonic acid (sPS-S_1), aryl sulfonic acid (sPS-S_2), and alkyl sulfonic acid (sPS-S_3) were prepared using this synthetic method. Detailed synthetic procedures for ionomers and sulfonated phenyl bromides are described in the experimental section and the supporting information.

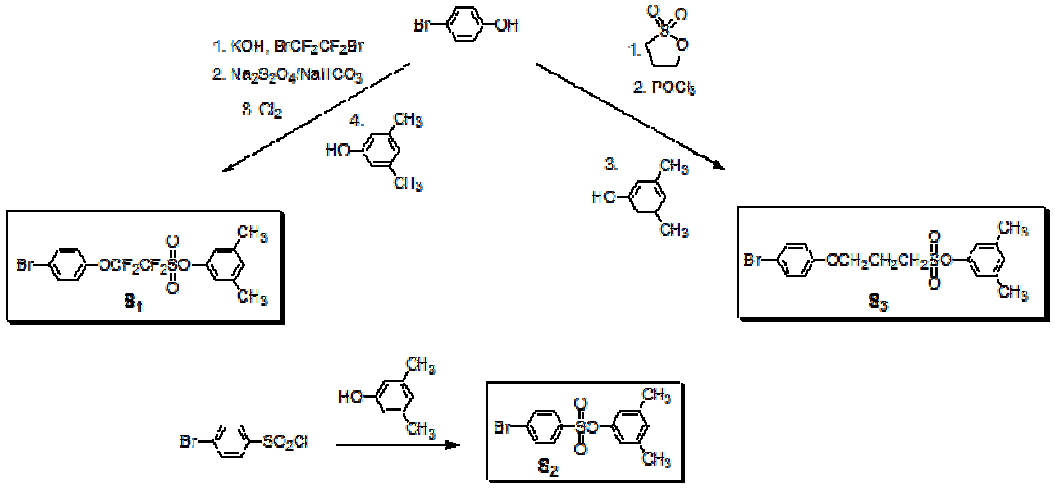

Figure 39: Scheme 2 Synthesis of sulfonated phenyl bromides.

Synthesis of Sulfonated Phenyl Bromides. To introduce sulfonate groups with different acidity strengths into sPS via the Suzuki–Miyaura coupling reaction, we prepared three types of phenyl bromides functionalized with sulfonate groups: fluoroalkyl sulfonated S_1, aryl sulfonated S_2, and alkyl sulfonated S_3 (Scheme 2, Figure 39). All three sulfonated

phenyl bromides were capped with a 3,5-dimethylphenol protecting group at the end and conveniently prepared from readily available chemicals in high yields using traditional organic synthetic methods. Nucleophilic substitution reaction of 4-bromophenol with 1,2-dibromotetrafluoroethane under basic conditions produces an ether covalent bond between oxygen and CF_2CF_2Br.[240] The terminal bromide was converted first to its sodium sulfinate form ($–SO_2Na$) via reaction with sodium dithionite and sodium bicarbonate and then to its sulfonyl chloride form ($–SO_2Cl$) by bubbling chlorine. The sulfonyl chloride was transformed to 3,5-dimethylphenol-protected sulfonate S_1 via reaction with 3,5-dimethylphenol in the presence of *N*,*N*-dimethylaminopyridine. Ring-opening of 1,3-propanesultone with 4-bromophenol under basic conditions, subsequent conversion of sodium sulfonate to sulfonyl chloride, and protection with 3,5-dimethylphenol afforded S_3 in good yield. S_2 was prepared from a condensation reaction of 4-bromobenzenesulfonyl chloride with 3,5-dimethylphenol in one step. All three protected sulfonates were air- and moisture-stable and could be stored under ambient conditions.

Synthesis and Characterization of Sulfonated Polymers. We recently reported a highly effective borylation of aromatic polymers using bis(pinacolato)diboron (B_2pin_2) as a borylation reagent in the iridium-catalyzed activation of aromatic C–H bonds.[241, 242] Because sPS gives a ^1H NMR spectrum that is more finely resolved than that of atactic polystyrene, owing to the high stereo-regularity of the phenyl rings along the polymer main chain (see Figure 40a), we chose sPS for post-functionalization in this study. The iridium-catalyzed borylation substitutes aromatic C–H bonds to C–B bonds under mild conditions while tolerating various functional groups.[243, 244] As reported

elsewhere,[241] the C–H borylation of sPS [weight average molecular weight (M_w) = 140.9 kg/mol; polydispersity index (M_w/M_n) = 2.90] was conducted in cyclooctane solvent at high temperature (150 ºC).

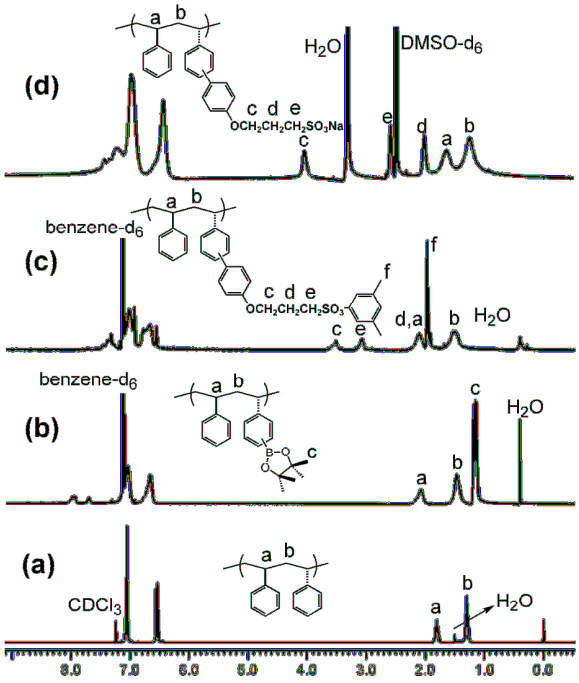

Figure 40: ^{1} H NMR spectra of (a) sPS, (b) sPS-Bpin, (c) sPS-S_3 in the 3,5-dimethylphenol protected form, and (d) sPS-S_3 in the –SO_3Na form.

After borylation of the polymer, a new proton signal corresponding to the four methyl groups of the pinacolboronic ester (Bpin) appeared at 1.16 ppm (Figure 40b). Integrals of the resonances of methylene at 1.49 ppm and methine at 2.09 ppm in the sPS main chain maintained a ratio of 2:1 in the ^{1}H NMR spectrum, suggesting that the main-chain structure of sPS remained intact during the borylation. Thus, the molar concentration of the attached Bpin group in the borylated polymer was estimated by comparing the

resonance integrals of the methyl group at 1.16 ppm and the methine proton of the polymer main chain at 2.09 ppm. The incorporated Bpin concentration was well controlled up to ~50 mol% simply by changing the loading amount of B_2pin_2 relative to the polymer repeating unit. For this work, we focused on borylated sPS with 40 mol% Bpin concentration.

The palladium-catalyzed Suzuki–Miyaura cross-coupling reaction of aryl boron compounds and aryl halides[245] has been a powerful method for biaryl C–C bond formation because of its high efficiency and good tolerance of functional groups. Thus, we conducted Suzuki–Miyaura coupling reactions of the borylated polymers with sulfonated phenyl bromides (S_1, S_2, and S_3 in Scheme 1) to incorporate the corresponding sulfonate groups into sPS. After the coupling reactions, the Bpin resonance of sPS-Bpin at 1.16 ppm disappeared completely in the ^{1}H NMR spectra, and a new signal at 1.97 ppm appeared and was assigned to the two methyl groups of the 3,5-dimethylphenol structure of the sulfonated sPS (Figure 40c).

Similar to that in the sPS-Bpin characterization, the concentration of 3,5-dimethylphenol-protected sulfonate groups in the polymers was calculated based on the integral ratio of the methine proton of the sPS main chain (at 2.09 ppm) and the terminal methyl groups in the side chain of sulfonated sPS (at 1.97 ppm). The molar concentration of the sulfonate group matched well with that of the borylated group in the precursor polymer (i.e., 40 mol%). In the case of the coupling reaction with S_3, the resulting polymer also showed the characteristic propylene group of S_3 at 3.52, 3.08, and 2.12 ppm with the expected molar concentrations. Successful incorporation of the fluoroalkyl sulfonate group after the coupling reaction with S_1 was further confirmed by two clean resonances at –80.3

ppm (–OCF_2–) and –111.9 ppm (–CF_2SO_3–) in the ^{19}F NMR spectrum (Figure 41a). Unlike electrophilic sulfonation of aromatic polymers using chlorosulfonic acid or sulfuric acid, in which polymer gelation frequently occurs because of undesired side reactions (cross-linking) in the polymer chains,[246] the borylation and the subsequent coupling reaction caused no gelation.

Removal of 3,5-dimethylphenol from the protected sulfonate groups of sPS using basic hydrolysis and subsequent acidification with sulfuric acid yielded the final sPS ionomers functionalized with fluoroalkyl, aryl, or alkyl sulfonic acid groups (sPS-S_1, sPS-S_2, and sPS-S_3, respectively, in Scheme 1). Basic hydrolysis of the protected sulfonated sPS was conducted with sodium hydroxide in a mixture of dioxane and water. Upon completion of the reaction, the sPS ionomers in the sodium salt form precipitated owing to a dramatic solubility change in the medium. The ionic polymers were stirred in a refluxing solution of water and methanol to remove salt and organic impurities and filtered. After the deprotection step, the ^{1}H NMR resonance of the methyl side groups at 1.97 ppm disappeared, and the ^{19}F NMR resonance of –CF_2SO_3– in sPS-S_1 shifted to –116.2 ppm (Figure 41b). A small amount of desulfonation was also detected during the deprotection of the 3,5-dimethylphenol group of sPS-S_1. In addition to the expected resonances of –$CF_2CF_2SO_3Na$ at –80.4 and –116.2 ppm, two small resonances were observed at –86.9 ppm and –137.2 ppm in the ^{19}F NMR spectrum of deprotected sPS-S_1, and they were identified as –CF_2CF_2H and –CF_2CF_2H, respectively (Figure 41b). Confirmation of the desulfonated side chain structure was made from its anticipated chemical shift range and the splitting pattern of CF_2CF_2H in the ^{19}F NMR spectrum (doublet; J = 59 Hz). The ^{19}F NMR resonance integral of the desulfonated structure was less than 5% of that of –

$CF_2CF_2SO_3Na$. In contrast, no similar desulfonation was observed when we examined the ^1H and ^{13}C NMR spectra of sPS-S_3. Therefore, the desulfonation that occurs during the deprotection step of the sPS-S_1 synthesis might be due to the presence of the strong electron-withdrawing fluoroalkyl group, which can weaken the C–S bond. Although further study is needed to confirm this hypothesis, we were delighted to see that only a small fraction of the sulfonate group in sPS-S_1 underwent the undesired side reaction.

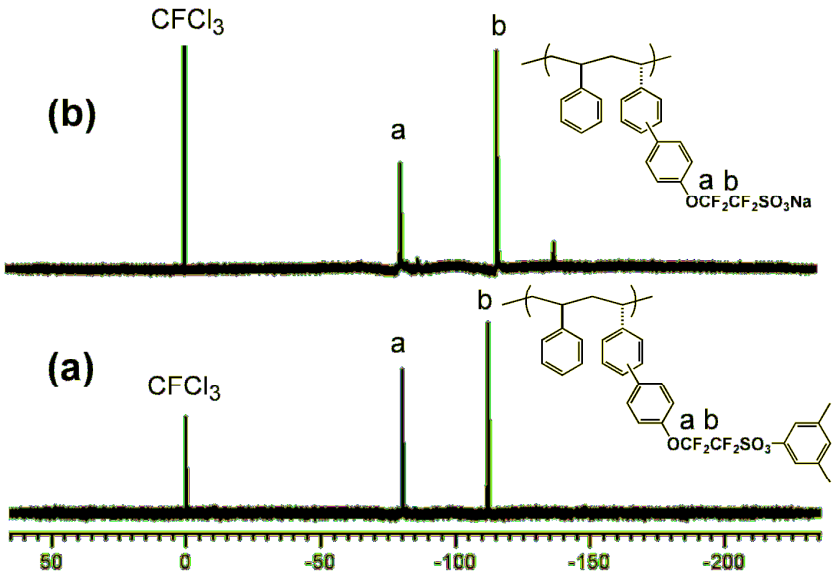

Figure 41: ^{19}F NMR spectra of sulfonated sPS-S_1 before (a) and after (b) deprotection of the 3,5-dimethylphenol group.

References

[1] E. I. A. (EIA), "Annual Energy Review 2011," D. o. Energy, Ed., ed. Washington DC, 2012.

[2] S. Solomon, D. Qin, M. Manning, Z. Chen, M. Marquis, K.B. Averyt, M. Tignor, H.L. Miller *Contribution of Working Group I to the Fourth Assessment Report of the Intergovernmental Panel on Climate Change*: Cambridge University Press, 2007.

[3] B. G. Pollet, I. Staffell, and J. L. Shang, "Current status of hybrid, battery and fuel cell electric vehicles: From electrochemistry to market prospects," *Electrochimica Acta,* vol. 84, pp. 235-249, 12/1/ 2012.

[4] L. Carrette, K. A. Friedrich, and U. Stimming, "Fuel cells: Principles, types, fuels, and applications," *Chemphyschem,* vol. 1, pp. 162-193, 2000.

[5] A. Chen. (2008). *Modeling to Build Better Fuel Cell*. Available: newscenter.lbl.gov/feature-stories/2008/04/18/modeling-to-build-a-better-fuel-cell/

[6] K. D. Kreuer, "On the development of proton conducting polymer membranes for hydrogen and methanol fuel cells," *Journal of Membrane Science,* vol. 185, pp. 29-39, Apr 15 2001.

[7] A. Aiyejina and M. K. S. Sastry, "PEMFC Flow Channel Geometry Optimization: A Review," *Journal of Fuel Cell Science and Technology,* vol. 9, p. 011011, 2012.

[8] Y. Wang, K. S. Chen, J. Mishler, S. C. Cho, and X. C. Adroher, "A review of polymer electrolyte membrane fuel cells: Technology, applications, and needs on fundamental research," *Applied Energy,* vol. 88, pp. 981-1007, 4// 2011.

[9] Y. Yu, H. Li, H. Wang, X.-Z. Yuan, G. Wang, and M. Pan, "A review on performance degradation of proton exchange membrane fuel cells during startup and shutdown processes: Causes, consequences, and mitigation strategies," *Journal of Power Sources,* vol. 205, pp. 10-23, 5/1/ 2012.

[10] R. Feynman, "The Feynman lectures on physics," ed, 1977.

[11] D. J. Griffiths, *Introduction to quantum mechanics*. Upper Saddle River, NJ: Pearson Prentice Hall, 2005.

[12] M. Planck, "Entropy and Temperature of Radiant Heat," *Annalen der Physik,* vol. 1, 1900.

[13] L. de Broglie, "Recherches sur la theorie des quanta," Paris, 1924.

[14] O. J. R. Born M, "Quantum theory of molecules," *Annalen der Physik,* vol. 84, p. 457, 1927.

[15] A. Szabo and N. S. Ostlund, *Moderm Quantum Chemistry. Introduction to Advanced Electronic Structure Theory*. New York: McGraw-Hill, 1996.

[16] P. Hohenberg and W. Kohn, "Inhomogeneous Electron Gas," *Physical Review,* vol. 136, pp. B864-B871, 11/09/ 1964.

[17] D. S. Sholl and J. A. Steckel, *Density Functional Theory. A Practical Introduction*: Wiley, 2009.

[18] W. Kohn and L. J. Sham, "Self-Consistent Equations Including Exchange and Correlation Effects," *Physical Review,* vol. 140, pp. A1133-A1138, 11/15/ 1965.
[19] D. Frenkel and B. Smit, *Understanding Molecular Simulation*: Academic Press, 2002.
[20] W. C. Swope, H. C. Andersen, P. H. Berens, and K. R. Wilson, "A COMPUTER-SIMULATION METHOD FOR THE CALCULATION OF EQUILIBRIUM-CONSTANTS FOR THE FORMATION OF PHYSICAL CLUSTERS OF MOLECULES - APPLICATION TO SMALL WATER CLUSTERS," *Journal of Chemical Physics,* vol. 76, pp. 637-649, 1982 1982.
[21] S. L. Mayo, B. D. Olafson, and W. A. Goddard, III, "DREIDING - A GENERIC FORCE-FIELD FOR MOLECULAR SIMULATIONS," *J. Phys. Chem.,* vol. 94, pp. 8897-8909, 1990.
[22] J. A. Elliott, S. Hanna, A. M. S. Elliott, and G. E. Cooley, "Atomistic simulation and molecular dynamics of model systems for perfluorinated ionomer membranes," *Phys. Chem. Chem. Phys.,* vol. 1, pp. 4855-4863, 1999.
[23] A. Vishnyakov and A. V. Neimark, "Molecular simulation study of nafion membrane solvation in water and methanol," *J. Phys. Chem. B,* vol. 104, pp. 4471-4478, 2000.
[24] A. Vishnyakov and A. V. Neimark, "Molecular dynamics simulation of nafion oligomer solvation in equimolar methanol-water mixture," *J. Phys. Chem. B,* vol. 105, pp. 7830-7834, 2001.
[25] T. Li, A. Wlaschin, and P. B. Balbuena, "Theoretical studies of proton transfer in water and model polymer electolyte systems," *Industrial & Engineering Chemistry Research,* vol. 40, pp. 4789-4800, 2001.
[26] S. S. Jang, V. Molinero, T. Cagin, and W. A. Goddard, III, "Nanophse-segregation and transport in Nafion 117 from molecular dynamics simulations: Effect of monomeric sequence," *J. Phys. Chem. B,* vol. 108, pp. 3149-3157, 2004.
[27] R. Devanathan, A. Venkatnathan, and M. Dupuis, "Atomistic simulation of nafion membrane. 2. Dynamics of water molecules and hydronium ions," *Journal of Physical Chemistry B,* vol. 111, pp. 13006-13013, Nov 15 2007.
[28] R. Devanathan, A. Venkatnathan, and M. Dupuis, "Atomistic simulation of nafion membrane: I. Effect of hydration on membrane nanostructure," *Journal of Physical Chemistry B,* vol. 111, pp. 8069-8079, Jul 19 2007.
[29] S. S. Jang, S.-T. Lin, T. Cagin, V. Molinero, and W. A. Goddard, III, "Nanophase-segregation and water dynamics in the dendrion diblock copolymer formed from the Frechet polyaryl ethereal dendrimer and linear PTFE," *J. Phys. Chem. B,* vol. 109, pp. 10154-10167, 2005.
[30] S. S. Jang and W. A. Goddard, III, "Structures and Transport Properties of Hydrated Water-Soluble Dendrimer-Grafted Polymer Membranes for Application to Polymer Electrolyte Membrane Fuel Cells: Classical Molecular Dynamics Approach," *Journal of Physical Chemistry C,* vol. 111, pp. 2759-2769, 2007.
[31] S. S. Jang, W. A. Goddard, III, M. Y. S. Kalani, D. Myung, and C. W. Frank, "Mechanical and transport properties of the poly(ethylene oxide)-poly(acrylic acid) double network hydrogel from molecular dynamic Simulations (vol 111B, pg 1729, 2007)," *Journal of Physical Chemistry B,* vol. 111, pp. 14440-14440, Dec 2007.

[32] S. S. Jang, W. A. Goddard, III, and Y. Kalani, "Mechanical and Transport Properties of Poly (Ethylene Oxide) - Poly (Acrylic Acid) Double Network Hydrogel: Molecular Dynamic Simulation Approach," *J. Phys. Chem. B,* vol. 111, pp. 1729-1737, 2007.

[33] S. S. Jang and W. A. Goddard, "Structures and properties of newton black films characterized using molecular dynamics simulations," *Journal of Physical Chemistry B,* vol. 110, pp. 7992-8001, Apr 20 2006.

[34] S. S. Jang, S.-T. Lin, P. K. Maiti, M. Blanco, W. A. Goddard, III, P. Shuler*, et al.*, "Molecular dynamics study of surfactant-mediated decane/water interface: Effect of molecular architecture of alkyl benzne sulfonate," *J. Phys. Chem. B,* vol. 108, pp. 12130-12140, 2004.

[35] Y. H. Kim, S. S. Jang, and W. A. Goddard, "Possible performance improvement in [2]catenane molecular electronic switches," *Applied Physics Letters,* vol. 88, Apr 2006.

[36] S. S. Jang, Y. H. Jang, Y.-H. Kim, W. A. Goddard, III, J. W. Choi, J. R. Heath*, et al.*, "Molecular Dynamics Simulation of Amphiphilic Bistable [2] Rotaxane Langmuir Monolayer at the Air/Water Interface," *J. Am. Chem. Soc.,* vol. 127, pp. 14804-14816, 2005.

[37] S. S. Jang, Y. H. Jang, Y.-H. Kim, W. A. Goddard, III, A. H. Flood, B. W. Laursen*, et al.*, "Structures and Properties of Self-Assembled Monolayers of Bistable [2]Rotaxanes on Au (111) Surfaces from Molecular Dynamics Simulations Validated with Experiment," *Journal of the American Chemical Society,* vol. 127, pp. 1563-1575, 2005.

[38] Y. H. Kim, S. S. Jang, and W. A. Goddard, III, "Conformations and charge transport characteristics of biphenyldithiol self-assembled-monolayer molecular electronic devices: A multiscale computational study (vol 122, art no 244703, 2005)," *Journal of Chemical Physics,* vol. 123, Oct 2005.

[39] Y. H. Kim, S. S. Jang, and W. A. Goddard, III, "Conformations and charge transport characteristics of biphenyldithiol self-assembled-monolayer molecular electronic devices: A multiscale computational study," *Journal of Chemical Physics,* vol. 122, Jun 2005.

[40] Y. H. Kim, S. S. Jang, Y. H. Jang, and W. A. Goddard, III, "First-principles study of the switching mechanism of [2]catenane molecular electronic devices," *Physical Review Letters,* vol. 94, Apr 2005.

[41] M. Levitt, M. Hirshberg, R. Sharon, K. E. Laidig, and V. Daggett, "Calibration and Testing of a Water Model for Simulation of the Molecular Dynamics of Proteins and Nucleic Acids in Solution," *Journal of Physical Chemistry B,* vol. 101, pp. 5051-5061, 1997.

[42] S. S. Jang, M. Blanco, W. A. Goddard, III, G. Caldwell, and R. B. Ross, "THE SOURCE OF HELICITY IN PERFLUORINATED N-ALKANES," *Macromolecules,* vol. 36, pp. 5331-5341, 2003.

[43] R. W. Hockney and J. W. Eastwood, *Computer simulation using particles*. New York: McGraw-Hill International Book Co., 1981.

[44] S. Nose, "A UNIFIED FORMULATION OF THE CONSTANT TEMPERATURE MOLECULAR-DYNAMICS METHODS," *Journal of Chemical Physics,* vol. 81, pp. 511-519, 1984 1984.

[45] S. Nose, "A MOLECULAR-DYNAMICS METHOD FOR SIMULATIONS IN THE CANONICAL ENSEMBLE," *Molecular Physics,* vol. 52, pp. 255-268, 1984 1984.
[46] S. Nose, "AN EXTENSION OF THE CANONICAL ENSEMBLE MOLECULAR-DYNAMICS METHOD," *Molecular Physics,* vol. 57, pp. 187-191, Jan 1986.
[47] S. J. Plimpton, "Fast Parallel Algorithms for Short-Range Molecular Dynamics," *J. Comp. Phys.,* vol. 117, pp. 1-19, 1995.
[48] S. J. Plimpton, R. Pollock, and M. Stevens, "Particle-Mesh Ewald and rRESPA for Parallel Molecular Dynamics Simulations," in *the Eighth SIAM Conference on Parallel Processing for Scientific Computing*, Minneapolis, 1997.
[49] W. H. Jo and S. S. Jang, "Monte Carlo simulation of the order-disorder transition of a symmetric cyclic diblock copolymer system," *J. Chem. Phys.,* vol. 111, pp. 1712-1720, 1999.
[50] W. H. Jo, J. G. Kim, S. S. Jang, J. H. Youk, and S. C. Lee, "Effects of Ester Interchange Reactions on the Phase Behavior of an Immiscible polyester Blend: Monte Carlo Simulation," *Macromolecules,* vol. 32, pp. 1679-1685, 1999.
[51] G. Brunello, S. G. Lee, S. S. Jang, and Y. Qi, "A molecular dynamics simulation study of hydrated sulfonated poly(ether ether ketone) for application to polymer electrolyte membrane fuel cells: Effect of water content," *Journal of Renewable and Sustainable Energy,* vol. 1, May 2009.
[52] M. Rikukawa and K. Sanui, "Proton-conducting polymer electrolyte membranes based on hydrocarbon polymers," *Progress in Polymer Science,* vol. 25, pp. 1463-1502, Dec 2000.
[53] T. Kobayashi, M. Rikukawa, K. Sanui, and N. Ogata, "Proton-conducting polymers derived from poly(ether-etherketone) and poly(4-phenoxybenzoyl-1,4-phenylene)," *Solid State Ionics,* vol. 106, pp. 219-225, Feb 1998.
[54] Y. Sone, P. Ekdunge, and D. Simonsson, "Proton Conductivity of Nafion 117 as Measured by a Four-Electrode AC Impedance Method," *Journal of The Electrochemical Society,* vol. 143, pp. 1254-1259, January 1, 1996 1996.
[55] K. D. Kreuer, "On the development of proton conducting polymer membranes for hydrogen and methanol fuel cell," *Journal of Membrane Science,* vol. 185, pp. 29-39, 2001.
[56] S. M. J. Zaidi, S. D. Mikhailenko, G. P. Robertson, M. D. Guiver, and S. Kaliaguine, "Proton conducting composite membranes from polyether ether ketone and heteropolyacids for fuel cell applications," *Journal of Membrane Science,* vol. 173, pp. 17-34, Jul 10 2000.
[57] S. Kaliaguine, S. D. Mikhailenko, K. P. Wang, P. Xing, G. Robertson, and M. Guiver, "Properties of SPEEK based PEMs for fuel cell application," *Catalysis Today,* vol. 82, pp. 213-222, Jul 30 2003.
[58] P. X. Xing, G. P. Robertson, M. D. Guiver, S. D. Mikhailenko, K. P. Wang, and S. Kaliaguine, "Synthesis and characterization of sulfonated poly(ether ether ketone) for proton exchange membranes," *Journal of Membrane Science,* vol. 229, pp. 95-106, Feb 1 2004.

[59] J. A. Elliott and S. J. Paddison, "Modelling of morphology and proton transport in PFSA membranes," *Physical Chemistry Chemical Physics,* vol. 9, pp. 2602-2618, Jun 2007.

[60] S. J. Paddison and J. A. Elliott, "On the consequences of side chain flexibility and backbone conformation on hydration and proton dissociation in perfluorosulfonic acid membranes," *Physical Chemistry Chemical Physics,* vol. 8, pp. 2193-2203, May 2006.

[61] L. H. Hristov, S. J. Paddison, and R. Paul, "Molecular modeling of proton transport in the short-side-chain perfluorosulfonic acid ionomer," *Journal of Physical Chemistry B,* vol. 112, pp. 2937-2949, Mar 2008.

[62] J. W. Liu, M. E. Selvan, S. Cui, B. J. Edwards, D. J. Keffer, and W. V. Steele, "Molecular-level Modeling of the structure and wetting of Electrode/Electrolyte interfaces in hydrogen fuel cells," *Journal of Physical Chemistry C,* vol. 112, pp. 1985-1993, Feb 2008.

[63] S. T. Cui, J. Liu, M. Esai Selvan, D. J. Keffer, B. J. Edwards, and W. V. Steele, "A Molecular Dynamics Study of a Nafion Polyelectrolyte Membrane and the Aqueous Phase Structure for Proton Transport," *J. Phys. Chem. B,* vol. 111, pp. 3469-3475, 2007.

[64] M. E. Selvan, J. Liu, D. J. Keffer, S. Cui, B. J. Edwards, and W. V. Steele, "Molecular dynamics study of structure and transport of water and hydronium ions at the membrane/vapor interface of Nafion," *Journal of Physical Chemistry C,* vol. 112, pp. 1975-1984, Feb 2008.

[65] A. Venkatnathan, R. Devanathan, and M. Dupuis, "Atomistic simulations of hydrated Nafion and temperature effects on hydronium ion mobility," *Journal of Physical Chemistry B,* vol. 111, pp. 7234-7244, Jun 2007.

[66] S. Dokmaisrijan and E. Spohr, "MD simulations of proton transport along a model Nafion surface decorated with sulfonate groups," *Journal of Molecular Liquids,* vol. 129, pp. 92-100, Oct 2006.

[67] N. P. Blake, G. Mills, and H. Metiu, "Dynamics of H2O and Na+ in nafion membranes," *Journal of Physical Chemistry B,* vol. 111, pp. 2490-2494, Mar 2007.

[68] N. P. Blake, M. K. Petersen, G. A. Voth, and H. Metiu, "Structure of Hydrated Na-Nafion Polymer Membrane," *J. Phys. Chem. B,* vol. 109, pp. 24244-24253, 2005.

[69] D. Brandell, J. Karo, A. Liivat, and J. O. Thomas, "Molecular dynamics studies of the Nafion (R), Dow (R) and Aciplex (R) fuel-cell polymer membrane systems," *Journal of Molecular Modeling,* vol. 13, pp. 1039-1046, Oct 2007.

[70] A. K. Rappe and W. A. Goddard, III, "Charge Equilibration for Molecular-Dynamics Simulations," *Journal of Physical Chemistry,* vol. 95, pp. 3358-3363, Apr 18 1991.

[71] S. Nose, "A Unified Formulation of the Constant Temperature Molecular-Dynamics Methods," *Journal of Chemical Physics,* vol. 81, pp. 511-519, 1984.

[72] Accelrys_Inc., *Cerius2 Modeling Environment, Release 4.0*. San Diego: Accelrys Inc., 1999.

[73] N. Agmon, "THE GROTTHUSS MECHANISM," *Chemical Physics Letters,* vol. 244, pp. 456-462, Oct 13 1995.

[74] N. Agmon, S. Y. Goldberg, and D. Huppert, "SALT EFFECT ON TRANSIENT PROTON-TRANSFER TO SOLVENT AND MICROSCOPIC PROTON MOBILITY," *Journal of Molecular Liquids,* vol. 64, pp. 161-195, Aug 1995.

[75] K. D. Kreuer, "Proton conductivity: materials and applications," *Chem. Mater.,* vol. 8, pp. 610-641, 1996.

[76] K. D. Kreuer, "On the development of proton conducting materials for technological applications," *Solid state ionics,* vol. 97, pp. 1-15, 1997.

[77] K. D. Kreuer, "On the complexity of proton conduction phenomena," *Solid state ionics,* vol. 136-137, pp. 149-160, 2000.

[78] M. Tuckerman, K. Laasonen, M. Sprik, and M. Parrinello, "AB-INITIO MOLECULAR-DYNAMICS SIMULATION OF THE SOLVATION AND TRANSPORT OF H3O+ AND OH- IONS IN WATER," *Journal of Physical Chemistry,* vol. 99, pp. 5749-5752, Apr 20 1995.

[79] M. E. Tuckerman, D. Marx, M. L. Klein, and M. Parrinello, "On the quantum nature of the shared proton in hydrogen bonds," *Science,* vol. 275, pp. 817-820, Feb 7 1997.

[80] D. Marx, M. E. Tuckerman, J. Hutter, and M. Parrinello, "The nature of the hydrated excess proton in water," *Nature,* vol. 397, pp. 601-604, Feb 18 1999.

[81] D. Marx, M. E. Tuckerman, and M. Parrinello, "Solvated excess protons in water: quantum effects on the hydration structure," *Journal of Physics-Condensed Matter,* vol. 12, pp. A153-A159, Feb 28 2000.

[82] M. W. Verbrugge and R. F. Hill, "Ion and solvent transport in ion-exchange membranes: II. A radiotracer study of the sulfuric-acid, Nafion-117 system," *J. Electrochem. Soc.,* vol. 137, pp. 893-899, 1990.

[83] M. W. Verbrugge and R. F. Hill, "Analysis of promising perfluorosulfonic acid membranes for fuel-cell electrolytes," *J. Electrochem. Soc.,* vol. 137, pp. 3770-3777, 1990.

[84] T. A. Zawodzinski, M. Neeman, L. O. Sillerud, and S. Gottesfeld, "Determination of water diffusion coefficients in perfluorosulfonate ionomeric membrane," *Journal of Physical Chemistry,* vol. 95, pp. 6040-6044, 1991.

[85] S. J. Paddison, "Proton conduction mechanisms at low degrees of hydration in sulfonic acid-based polymer electrolyte membranes," *Annual Review of Materials Research,* vol. 33, pp. 289-319, 2003 2003.

[86] A. K. Soper and M. G. Phillips, "A new determination of the structure of water at 25 C," *Chem. Phys.,* vol. 107, pp. 47-60, 1986.

[87] M. Schuster, K. D. Kreuer, and J. Maier, "Proton, Water and methanol transport in Nafion and sulfonated polyether ketone based membranes: A microstructural approach," in *14th international conference on solid state ionics*, Monterey, USA, 2003, p. 395.

[88] K. Krynicki, C. D. Green, and D. W. Sawyer, "Pressure and temperature dependence of self-diffusion in water," *Discuss. Faraday Soc.,* vol. 66, pp. 199-208, 1978.

[89] R. Mills, "Self-diffusion in normal and heavy water in the range 1-45o," *J. Phys. Chem.,* vol. 77, pp. 685-688, 1973.

[90] W. S. Price, H. Ide, and Y. Arata, "Self-Diffusion of Supercooled Water to 238 K Using PGSE NMR Diffusion Measurements," *J. Phys. Chem. A,* vol. 103, pp. 448-450, 1999.
[91] T. Okada, G. Xie, and M. Meeg, "Simulation for water management in membranes for polymer electrolyte fuel cell," *Electrochim. Acta,* vol. 14, pp. 2141-2155, 1998.
[92] G. F. Brunello, W. R. Mateker, S. G. Lee, J. I. Choi, and S. S. Jang, "Effect of temperature on structure and water transport of hydrated sulfonated poly(ether ether ketone): A molecular dynamics simulation approach," *Journal of Renewable and Sustainable Energy,* vol. 3, p. 043111, 2011.
[93] A. Eisenberg and H. L. Yeager, Eds., *Perfluorinated Ionomer Membranes* (ACS Sumposium Series. Washington, D.C.: American Chemical Society, 1982, p.^pp. Pages.
[94] H. L. Yeager and A. Steck, *Analytical Chemistry,* vol. 51, pp. 862-865, 1979.
[95] S. C. Yeo and A. Eisenberg, "Physical properties and supermolecular structure of perfluorinated ion-containing (Nafion) polymers," *J. Appl. Polym. Sci.,* vol. 21, pp. 875-898, 1977.
[96] A. Eisenberg and M. King, in *Polymer Physics*, R. S. Stein, Ed., ed New York: Academic Press, 1977.
[97] G. Scibona, C. Fabiani, and B. Scuppa, "ELECTROCHEMICAL-BEHAVIOR OF NAFION TYPE MEMBRANE," *J. Membr. Sci.,* vol. 16, pp. 37-50, 1983.
[98] A. Roy, X. Yu, S. Dunn, and J. E. McGrath, "Influence of microstructure and chemical composition on proton exchange membrane properties of sulfonated-fluorinated, hydrophilic-hydrophobic multiblock copolymers," *Journal of Membrane Science,* vol. 327, pp. 118-124, Feb 5 2009.
[99] J. Liu, M. Wang, S. Y. Chen, and M. O. Robbins, "Molecular simulations of electroosmotic flows in rough nanochannels," *Journal of Computational Physics,* vol. 229, pp. 7834-7847, Oct 1 2010.
[100] C. W. James, A. Roy, J. E. McGrath, and E. Marand, "Determination of the effect of temperature and humidity on the O-2 sorption in sulfonated poly(arylene ether sulfone) membranes," *Journal of Membrane Science,* vol. 309, pp. 141-145, Feb 15 2008.
[101] Y. S. Kim, M. A. Hickner, L. M. Dong, B. S. Pivovar, and J. E. McGrath, "Sulfonated poly(arylene ether sulfone) copolymer proton exchange membranes: composition and morphology effects on the methanol permeability," *Journal of Membrane Science,* vol. 243, pp. 317-326, Nov 1 2004.
[102] J. Liu, N. Suraweera, D. J. Keffer, S. Cui, and S. J. Paddison, "On the Relationship between Polymer Electrolyte Structure and Hydrated Morphology of Perfluorosulfonic Acid Membranes," *The Journal of Physical Chemistry C,* vol. 114, pp. 11279-11292, 2010.
[103] C. V. Mahajan and V. Ganesan, "Atomistic Simulations of Structure of Solvated Sulfonated Poly(ether ether ketone) Membranes and Their Comparisons to Nafion: I. Nanophase Segregation and Hydrophilic Domains," *Journal of Physical Chemistry B,* vol. 114, pp. 8357-8366, Jul 1 2010.
[104] C. V. Mahajan and V. Ganesan, "Atomistic Simulations of Structure of Solvated Sulfonated Poly(ether ether ketone) Membranes and Their Comparisons to

Nafion: II. Structure and Transport Properties of Water, Hydronium Ions, and Methanol," *Journal of Physical Chemistry B,* vol. 114, pp. 8367-8373, Jul 1 2010.
[105] R. D. Lins, R. Devanathan, and M. Dupuis, "Modeling the Nanophase Structural Dynamics of Phenylated Sulfonated Poly Ether Ether Ketone Ketone (Ph-SPEEKK) Membranes As a Function of Hydration," *Journal of Physical Chemistry B,* vol. 115, pp. 1817-1824, Mar 3 2011.
[106] E. Tocci and P. Pullumbi, "Molecular simulation of realistic membrane models of alkylated PEEK membranes," *Molecular Simulation,* vol. 32, pp. 145-154, Feb 2006.
[107] R. K. Goyal, A. N. Tiwari, U. P. Mulik, and Y. S. Negi, "Thermal expansion behaviour of high performance PEEK matrix composites," *Journal of Physics D-Applied Physics,* vol. 41, pp. -, Apr 21 2008.
[108] Y. Chang, G. F. Brunello, J. Fuller, M. Hawley, Y. S. Kim, M. Disabb-Miller*, et al.*, "Aromatic Ionomers with Highly Acidic Sulfonate Groups: Acidity, Hydration, and Proton Conductivity," *Macromolecules,* vol. 44, pp. 8458-8469, 2011/11/08 2011.
[109] M. A. Hickner, H. Ghassemi, Y. S. Kim, B. R. Einsla, and J. E. McGrath, "Alternative polymer systems for proton exchange membranes (PEMs)," *Chemical Reviews,* vol. 104, pp. 4587-4611, Oct 2004.
[110] W. L. Harrison, M. A. Hickner, Y. S. Kim, and J. E. McGrath, "Poly(arylene ether sulfone) copolymers and related systems from disulfonated monomer building blocks: Synthesis, characterization, and performance - A topical review," *Fuel Cells,* vol. 5, pp. 201-212, Apr 2005.
[111] G. Alberti, M. Casciola, L. Massinelli, and B. Bauer, "Polymeric proton conducting membranes for medium temperature fuel cells (110-160 degrees C)," *Journal of Membrane Science,* vol. 185, pp. 73-81, Apr 15 2001.
[112] Q. F. Li, R. H. He, J. O. Jensen, and N. J. Bjerrum, "Approaches and recent development of polymer electrolyte membranes for fuel cells operating above 100 degrees C," *Chemistry of Materials,* vol. 15, pp. 4896-4915, Dec 30 2003.
[113] K. D. Kreuer, "Proton conductivity: Materials and applications," *Chemistry of Materials,* vol. 8, pp. 610-641, Mar 1996.
[114] T. A. Zawodzinski, M. Neeman, L. O. Sillerud, and S. Gottesfeld, "DETERMINATION OF WATER DIFFUSION-COEFFICIENTS IN PERFLUOROSULFONATE IONOMERIC MEMBRANES," *Journal of Physical Chemistry,* vol. 95, pp. 6040-6044, Jul 25 1991.
[115] K. A. Mauritz and R. B. Moore, "State of understanding of Nafion," *Chemical Reviews,* vol. 104, pp. 4535-4585, Oct 2004.
[116] R. W. Kopitzke, C. A. Linkous, H. R. Anderson, and G. L. Nelson, "Conductivity and water uptake of aromatic-based proton exchange membrane electrolytes," *Journal of the Electrochemical Society,* vol. 147, pp. 1677-1681, May 2000.
[117] F. Ng, J. Peron, D. J. Jones, and J. Roziere, "Synthesis of Novel Proton-Conducting Highly Sulfonated Polybenzimidazoles for PEMFC and the Effect of the Type of Bisphenyl Bridge on Polymer and Membrane Properties," *Journal of Polymer Science Part a-Polymer Chemistry,* vol. 49, pp. 2107-2117, May 15 2011.

[118] B. Liu, G. P. Robertson, D.-S. Kim, M. D. Guiver, W. Hu, and Z. Jiang, "Aromatic poly(ether ketone)s with pendant sulfonic acid phenyl groups prepared by a mild sulfonation method for proton exchange membranes," *Macromolecules,* vol. 40, pp. 1934-1944, Mar 20 2007.

[119] F. Wang, M. Hickner, Q. Ji, W. Harrison, J. Mecham, T. A. Zawodzinski*, et al.*, "Synthesis of highly sulfonated poly(arylene ether sulfone) random (statistical) copolymers via direct polymerization," *Macromolecular Symposia,* vol. 175, pp. 387-395, Aug 2001.

[120] N. W. Li, D. W. Shin, D. S. Hwang, Y. M. Lee, and M. D. Guiver, "Polymer Electrolyte Membranes Derived from New Sulfone Monomers with Pendent Sulfonic Acid Groups," *Macromolecules,* vol. 43, pp. 9810-9820, Dec 2010.

[121] A. Katzfuss, K. Krajinovic, A. Chromik, and J. Kerres, "Partially Fluorinated Sulfonated Poly(arylene sulfone)s Blended with Polybenzimidazole," *Journal of Polymer Science Part a-Polymer Chemistry,* vol. 49, pp. 1919-1927, Apr 15 2011.

[122] N. Asano, M. Aoki, S. Suzuki, K. Miyatake, H. Uchida, and M. Watanabe, "Aliphatic/aromatic polyimide lonomers as a proton conductive membrane for fuel cell applications," *Journal of the American Chemical Society,* vol. 128, pp. 1762-1769, Feb 8 2006.

[123] C. Genies, R. Mercier, B. Sillion, N. Cornet, G. Gebel, and M. Pineri, "Soluble sulfonated naphthalenic polyimides as materials for proton exchange membranes," *Polymer,* vol. 42, pp. 359-373, Jan 2001.

[124] X. Chen, K. Chen, P. Chen, M. Higa, K.-I. Okamoto, and T. Hiran, "Effects of Tetracarboxylic Dianhydrides on the Properties of Sulfonated Polyimides," *Journal of Polymer Science Part a-Polymer Chemistry,* vol. 48, pp. 905-915, Feb 15 2010.

[125] C. H. Fujimoto, M. A. Hickner, C. J. Cornelius, and D. A. Loy, "Ionomeric poly(phenylene) prepared by diels-alder polymerization: Synthesis and physical properties of a novel polyelectrolyte," *Macromolecules,* vol. 38, pp. 5010-5016, Jun 14 2005.

[126] M. A. Hickner and B. S. Pivovar, "The chemical and structural nature of proton exchange membrane fuel cell properties," *Fuel Cells,* vol. 5, pp. 213-229, Apr 2005.

[127] M. L. Einsla, Y. S. Kim, M. Hawley, H.-S. Lee, J. E. McGrath, B. Liu*, et al.*, "Toward improved conductivity of sulfonated aromatic proton exchange membranes at low relative humidity," *Chemistry of Materials,* vol. 20, pp. 5636-5642, Sep 9 2008.

[128] Y. A. Elabd and M. A. Hickner, "Block Copolymers for Fuel Cells," *Macromolecules,* vol. 44, pp. 1-11, Jan 11 2011.

[129] T. J. Peckham and S. Holdcroft, "Structure-Morphology-Property Relationships of Non-Perfluorinated Proton-Conducting Membranes," *Advanced Materials,* vol. 22, pp. 4667-4690, Nov 9 2010.

[130] B. Bae, T. Yoda, K. Miyatake, H. Uchida, and M. Watanabe, "Proton-Conductive Aromatic Ionomers Containing Highly Sulfonated Blocks for High-Temperature-Operable Fuel Cells," *Angewandte Chemie-International Edition,* vol. 49, pp. 317-320, 2010.

[131] S. Tian, Y. Meng, and A. S. Hay, "Membranes from Poly(aryl ether)-Based Ionomers Containing Multiblock Segments of Randomly Distributed Nanoclusters of 18 Sulfonic Acid Groups," *Journal of Polymer Science Part a-Polymer Chemistry,* vol. 47, pp. 4762-4773, Sep 15 2009.
[132] N. W. Li, D. S. Hwang, S. Y. Lee, Y. L. Liu, Y. M. Lee, and M. D. Guiver, "Densely Sulfophenylated Segmented Copoly(arylene ether sulfone) Proton Exchange Membranes," *Macromolecules,* vol. 44, pp. 4901-4910, Jun 2011.
[133] Y. S. Kim and B. S. Pivovar, "Moving Beyond Mass-Based Parameters for Conductivity Analysis of Sulfonated Polymers," in *Annual Review of Chemical and Biomolecular Engineering, Vol 1*. vol. 1, J. M. Prausnitz, M. F. Doherty, and M. A. Segalman, Eds., ed, 2010, pp. 123-148.
[134] G. A. Olah, G. K. S. Prakash, and J. Sommer, *Superacids*. New York: Wiley-Interscience, 1986.
[135] T. Mikami, K. Miyatake, and M. Watanabe, "Poly(arylene ether)s Containing Superacid Groups as Proton Exchange Membranes," *Acs Applied Materials & Interfaces,* vol. 2, pp. 1714-1721, Jun 2010.
[136] K. Miyatake, T. Shimura, T. Mikami, and M. Watanabe, "Aromatic ionomers with superacid groups," *Chemical Communications,* pp. 6403-6405, 2009 2009.
[137] K. Yoshimura and K. Iwasaki, "Aromatic Polymer with Pendant Perfluoroalkyl Sulfonic Acid for Fuel Cell Applications," *Macromolecules,* vol. 42, pp. 9302-9306, Dec 8 2009.
[138] H. Ghassemi, D. A. Schiraldi, T. A. Zawodzinski, and S. Hamrock, "Poly(arylene ether)s with Pendant Perfluoroalkyl Sulfonic Acid Groups as Proton-Exchange Membrane Materials," *Macromolecular Chemistry and Physics,* vol. 212, pp. 673-678, Apr 2011.
[139] H. B. Li, A. B. Jackson, N. J. Kirk, K. A. Mauritz, and R. F. Storey, "Poly(arylene ether sulfone) Statistical Copolymers Bearing Perfluoroalkylsulfonic Acid Moieties," *Macromolecules,* vol. 44, pp. 694-702, Feb 2011.
[140] T. Mikami, K. Miyatake, and M. Watanabe, "Synthesis and Properties of Multiblock Copoly(arylene ether)s Containing Superacid Groups for Fuel Cell Membranes," *Journal of Polymer Science Part a-Polymer Chemistry,* vol. 49, pp. 452-464, Jan 15 2011.
[141] K. Nakabayashi, T. Higashihara, and M. Ueda, "Polymer Electrolyte Membranes Based on Poly(phenylene ether)s with Pendant Perfluoroalkyl Sulfonic Acids," *Macromolecules,* vol. 44, pp. 1603-1609, Mar 22 2011.
[142] K. Xu, H. Oh, M. A. Hickner, and Q. Wang, "Highly Conductive Aromatic Ionomers with Perfluorosulfonic Acid Side Chains for Elevated Temperature Fuel Cells," *Macromolecules,* vol. 44, pp. 4605-4609, Jun 28 2011.
[143] H. Li, A. B. Jackson, N. J. Kirk, K. A. Mauritz, and R. F. Storey, "Poly(arylene ether sulfone) Statistical Copolymers Bearing Perfluoroalkylsulfonic Acid Moieties," *Macromolecules,* vol. 44, pp. 694-702, Feb 22 2011.
[144] S. L. Mayo, B. D. Olafson, and W. A. Goddard, "DREIDING - A GENERIC FORCE-FIELD FOR MOLECULAR SIMULATIONS," *Journal of Physical Chemistry,* vol. 94, pp. 8897-8909, Dec 27 1990.
[145] S. S. Jang, V. Molinero, T. Cagin, and W. A. Goddard, "Nanophase-segregation and transport in Nafion 117 from molecular dynamics simulations: Effect of

monomeric sequence," *Journal of Physical Chemistry B,* vol. 108, pp. 3149-3157, Mar 11 2004.

[146] S. S. Jang, S. T. Lin, T. Cagin, V. Molinero, and W. A. Goddard, "Nanophase segregation and water dynamics in the dendrion diblock copolymer formed from the Frechet polyaryl ethereal dendrimer and linear PTFE," *Journal of Physical Chemistry B,* vol. 109, pp. 10154-10167, May 26 2005.

[147] S. S. Jang and W. A. Goddard, III, "Structures and transport properties of hydrated water-soluble dendrimer-grafted polymer membranes for application to polymer electrolyte membrane fuel cells: Classical molecular dynamics approach," *Journal of Physical Chemistry C,* vol. 111, pp. 2759-2769, Feb 15 2007.

[148] S. S. Jang, W. A. Goddard, III, and M. Y. S. Kalani, "Mechanical and transport properties of the poly(ethylene oxide)-poly(acrylic acid) double network hydrogel from molecular dynamic simulations," *Journal of Physical Chemistry B,* vol. 111, pp. 1729-1737, Feb 22 2007.

[149] S. S. Jang, S. T. Lin, P. K. Maiti, M. Blanco, W. A. Goddard, P. Shuler*, et al.*, "Molecular dynamics study of a surfactant-mediated decane-water interface: Effect of molecular architecture of alkyl benzene sulfonate," *Journal of Physical Chemistry B,* vol. 108, pp. 12130-12140, Aug 12 2004.

[150] S. S. Jang, Y. H. Jang, Y. H. Kim, W. A. Goddard, J. W. Choi, J. R. Heath*, et al.*, "Molecular dynamics simulation of amphiphilic bistable 2 rotaxane Langmuir monolayers at the air/water interface," *Journal of the American Chemical Society,* vol. 127, pp. 14804-14816, Oct 26 2005.

[151] S. S. Jang, Y. H. Jang, Y. H. Kim, W. A. Goddard, A. H. Flood, B. W. Laursen*, et al.*, "Structures and properties of self-assembled monolayers of bistable 2 rotaxanes on Au(111) surfaces from molecular dynamics simulations validated with experiment," *Journal of the American Chemical Society,* vol. 127, pp. 1563-1575, Feb 9 2005.

[152] M. Levitt, M. Hirshberg, R. Sharon, K. E. Laidig, and V. Daggett, "Calibration and testing of a water model for simulation of the molecular dynamics of proteins and nucleic acids in solution," *Journal of Physical Chemistry B,* vol. 101, pp. 5051-5061, Jun 19 1997.

[153] S. Plimpton, "FAST PARALLEL ALGORITHMS FOR SHORT-RANGE MOLECULAR-DYNAMICS," *Journal of Computational Physics,* vol. 117, pp. 1-19, Mar 1 1995.

[154] F. G. Bordwell, "EQUILIBRIUM ACIDITIES IN DIMETHYL-SULFOXIDE SOLUTION," *Accounts of Chemical Research,* vol. 21, pp. 456-463, Dec 1988.

[155] J. P. Guthrie, "HYDROLYSIS OF ESTERS OF OXY ACIDS - PKA VALUES FOR STRONG ACIDS - BRONSTED RELATIONSHIP FOR ATTACK OF WATER AT METHYL - FREE-ENERGIES OF HYDROLYSIS OF ESTERS OF OXY ACIDS - AND A LINEAR RELATIONSHIP BETWEEN FREE-ENERGY OF HYDROLYSIS AND PKA HOLDING OVER A RANGE OF 20 PK UNITS," *Canadian Journal of Chemistry-Revue Canadienne De Chimie,* vol. 56, pp. 2342-2354, 1978 1978.

[156] J. E. McMurry, *Organic Chemistry*. Belmont, CA: Thomson Brooks/Cole, 2008.

[157] M. L. Einsla, Y. S. Kim, M. Hawley, H. S. Lee, J. E. McGrath, B. J. Liu*, et al.*, "Toward improved conductivity of sulfonated aromatic proton exchange membranes at low relative humidity," *Chemistry of Materials,* vol. 20, pp. 5636-5642, Sep 2008.

[158] F. Wang, M. Hickner, Y. S. Kim, T. A. Zawodzinski, and J. E. McGrath, "Direct polymerization of sulfonated poly(arylene ether sulfone) random (statistical) copolymers: candidates for new proton exchange membranes," *Journal of Membrane Science,* vol. 197, pp. 231-242, Mar 15 2002.

[159] M. A. Lill and V. Helms, "Reaction rates for proton transfer over small barriers and connection to transition state theory," *Journal of Chemical Physics,* vol. 115, pp. 7985-7992, Nov 1 2001.

[160] M. A. Lill and V. Helms, "Compact parameter set for fast estimation of proton transfer rates," *Journal of Chemical Physics,* vol. 114, pp. 1125-1132, Jan 15 2001.

[161] B. H. Greeley, T. V. Russo, D. T. Mainz, R. A. Friesner, J. M. Langlois, W. A. Goddard*, et al.*, "NEW PSEUDOSPECTRAL ALGORITHMS FOR ELECTRONIC-STRUCTURE CALCULATIONS - LENGTH SCALE SEPARATION AND ANALYTICAL 2-ELECTRON INTEGRAL CORRECTIONS," *Journal of Chemical Physics,* vol. 101, pp. 4028-4041, Sep 1 1994.

[162] B. Marten, K. Kim, C. Cortis, R. A. Friesner, R. B. Murphy, M. N. Ringnalda*, et al.*, "New model for calculation of solvation free energies: Correction of self-consistent reaction field continuum dielectric theory for short-range hydrogen-bonding effects," *Journal of Physical Chemistry,* vol. 100, pp. 11775-11788, Jul 11 1996.

[163] K. Koga, T. Ikeshoji, and K. Sugawara, "Size- and Temperature-Dependent Structural Transitions in Gold Nanoparticles," *Physical Review Letters,* vol. 92, p. 115507, 2004.

[164] Y. Sun and Y. Xia, "Shape-Controlled Synthesis of Gold and Silver Nanoparticles," *Science,* vol. 298, pp. 2176-2179, December 13, 2002 2002.

[165] R. Sardar, A. M. Funston, P. Mulvaney, and R. W. Murray, "Gold Nanoparticles: Past, Present, and Future," *Langmuir,* vol. 25, pp. 13840-13851, 2012/05/16 2009.

[166] S. Link, C. Burda, B. Nikoobakht, and M. A. El-Sayed, "Laser-Induced Shape Changes of Colloidal Gold Nanorods Using Femtosecond and Nanosecond Laser Pulses," *The Journal of Physical Chemistry B,* vol. 104, pp. 6152-6163, 2012/05/16 2000.

[167] G. Hodes, "When Small Is Different: Some Recent Advances in Concepts and Applications of Nanoscale Phenomena," *Advanced Materials,* vol. 19, pp. 639-655, 2007.

[168] M. J. Yacaman, J. A. Ascencio, H. B. Liu, and J. Gardea-Torresdey, "Structure shape and stability of nanometric sized particles," *Journal of Vacuum Science & Technology B: Microelectronics and Nanometer Structures,* vol. 19, pp. 1091-1103, 2001.

[169] J. P. Wilcoxon and B. L. Abrams, "Synthesis, structure and properties of metal nanoclusters," *Chemical Society Reviews,* vol. 35, pp. 1162-1194, 2006.

[170] H. Häkkinen and M. Manninen, "How “Magic” is a Magic Metal Cluster?," *Physical Review Letters,* vol. 76, pp. 1599-1602, 03/04/ 1996.
[171] S. Varga, B. Fricke, H. Nakamatsu, T. Mukoyama, J. Anton, D. Geschke*, et al.*, "Four-component relativistic density functional calculations of heavy diatomic molecules," *The Journal of Chemical Physics,* vol. 112, pp. 3499-3506, 2000.
[172] H. Grönbeck and W. Andreoni, "Gold and platinum microclusters and their anions: comparison of structural and electronic properties," *Chemical Physics,* vol. 262, pp. 1-14, 2000.
[173] J. Wang, G. Wang, and J. Zhao, "Density-functional study of Aun (n=2–20) clusters: Lowest-energy structures and electronic properties," *Physical Review B,* vol. 66, p. 035418, 2002.
[174] E. Aprà and A. Fortunelli, "Density-Functional Calculations on Platinum Nanoclusters: Pt13, Pt38, and Pt55," *The Journal of Physical Chemistry A,* vol. 107, pp. 2934-2942, 2003/04/01 2003.
[175] L. Xiao and L. Wang, "Structures of Platinum Clusters: Planar or Spherical?," *The Journal of Physical Chemistry A,* vol. 108, pp. 8605-8614, 2004/10/01 2004.
[176] W. Q. Tian, M. Ge, B. R. Sahu, D. Wang, T. Yamada, and S. Mashiko, "Geometrical and Electronic Structure of the Pt7 Cluster: A Density Functional Study," *The Journal of Physical Chemistry A,* vol. 108, pp. 3806-3812, 2004/04/01 2004.
[177] D.-K. Lee, G.-H. Jeung, and Y. S. Lee, "Two component calculations of Pt2 with relativistic effective core potential including spin-orbit operator," *International Journal of Quantum Chemistry,* vol. 109, pp. 1975-1983, 2009.
[178] W. Eberhardt, P. Fayet, D. M. Cox, Z. Fu, A. Kaldor, R. Sherwood*, et al.*, "Photoemission from mass-selected monodispersed Pt clusters," *Physical Review Letters,* vol. 64, pp. 780-783, 1990.
[179] Z. L. Wang, J. M. Petroski, T. C. Green, and M. A. El-Sayed, "Shape Transformation and Surface Melting of Cubic and Tetrahedral Platinum Nanocrystals," *The Journal of Physical Chemistry B,* vol. 102, pp. 6145-6151, 1998/08/01 1998.
[180] M. B. Airola and M. D. Morse, "Rotationally resolved spectroscopy of Pt2," *The Journal of Chemical Physics,* vol. 116, pp. 1313-1317, 2002.
[181] M. N. Huda, M. K. Niranjan, B. R. Sahu, and L. Kleinman, "Effect of spin-orbit coupling on small platinum nanoclusters," *Physical Review A,* vol. 73, p. 053201, 2006.
[182] K. Bhattacharyya and C. Majumder, "Growth pattern and bonding trends in Ptn (n=2–13) clusters: Theoretical investigation based on first principle calculations," *Chemical Physics Letters,* vol. 446, pp. 374-379, 2007.
[183] A. Sebetci, "Does spin-orbit coupling effect favor planar structures for small platinum clusters?," *Physical Chemistry Chemical Physics,* vol. 11, pp. 921-925, 2009.
[184] R. V. Chepulskii and S. Curtarolo, "Ab Initio Insights on the Shapes of Platinum Nanocatalysts," *ACS Nano,* vol. 5, pp. 247-254, 2011/01/25 2011.
[185] R. Kikuchi, "A THEORY OF COOPERATIVE PHENOMENA," *Physical Review,* vol. 81, pp. 988-1003, 1951.

[186] J. M. Sanchez, F. Ducastelle, and D. Gratias, "GENERALIZED CLUSTER DESCRIPTION OF MULTICOMPONENT SYSTEMS," *Physica A,* vol. 128, pp. 334-350, 1984.
[187] M. H. F. Sluiter and Y. Kawazoe, "Invariance of truncated cluster expansions for first-principles alloy thermodynamics," *Physical Review B,* vol. 71, p. 212201, 06/09/ 2005.
[188] R. Drautz and A. Díaz-Ortiz, "Obtaining cluster expansion coefficients in ab initio thermodynamics of multicomponent lattice-gas systems," *Physical Review B,* vol. 73, p. 224207, 06/29/ 2006.
[189] D. J. Schmidt, "Cluster Expansion Studies of Oxygen Adsorption on Transition Metal Surfaces," Doctorate of Philosophy, Chemical and Biomolecular Engineering Notre Dame, 2012.
[190] E. Langenbach, A. Spitzer, and H. Lüth, "The adsorption of water on Pt(111) studied by irreflection and UV-photoemission spectroscopy," *Surface Science,* vol. 147, pp. 179-190, 1984.
[191] A. Michaelides, V. A. Ranea, P. L. de Andres, and D. A. King, "General Model for Water Monomer Adsorption on Close-Packed Transition and Noble Metal Surfaces," *Physical Review Letters,* vol. 90, p. 216102, 2003.
[192] A. B. Anderson, "REACTIONS AND STRUCTURES OF WATER ON CLEAN AND OXYGEN COVERED PT(111) AND FE(100)," *Surface Science,* vol. 105, pp. 159-176, 1981.
[193] H. P. Bonzel, G. Pirug, and J. E. Muller, "REVERSIBLE H2O ADSORPTION ON PT(111) +K - WORK-FUNCTION CHANGES AND MOLECULAR-ORIENTATION," *Physical Review Letters,* vol. 58, pp. 2138-2141, May 1987.
[194] T. Jacob and W. A. Goddard, "Agostic interactions and dissociation in the first layer of water on Pt(111)," *Journal of the American Chemical Society,* vol. 126, pp. 9360-9368, Aug 2004.
[195] S. Kandoi, A. A. Gokhale, L. C. Grabow, J. A. Dumesic, and M. Mavrikakis, "Why Au and Cu are more selective than Pt for preferential oxidation of CO at low temperature," *Catalysis Letters,* vol. 93, pp. 93-100, Mar 2004.
[196] J. Kua and W. A. Goddard, "Oxidation of methanol on 2nd and 3rd row Group VIII transition metals (Pt, Ir, Os, Pd, Rh, and Ru): Application to direct methanol fuel cells," *Journal of the American Chemical Society,* vol. 121, pp. 10928-10941, Dec 1999.
[197] S. Meng, E. G. Wang, and S. W. Gao, "Water adsorption on metal surfaces: A general picture from density functional theory studies," *Physical Review B,* vol. 69, May 2004.
[198] T. Ohwaki, K. Kamegai, and K. Yamashita, "Electric field effects on the adsorption, charge transfer and vibrational state at metal electrodes: A DFT study on H2O/Pt(111), (H2O)/Pt(100) and (H2O)(2)/Pt(111)," *Bulletin of the Chemical Society of Japan,* vol. 74, pp. 1021-1029, Jun 2001.
[199] P. Vassilev, R. A. van Santen, and M. T. M. Koper, "Ab initio studies of a water layer at transition metal surfaces," *Journal of Chemical Physics,* vol. 122, Feb 2005.

[200] P. A. Thiel and T. E. Madey, "THE INTERACTION OF WATER WITH SOLID-SURFACES - FUNDAMENTAL-ASPECTS," *Surface Science Reports,* vol. 7, pp. 211-385, 1987.
[201] A. Michaelides and K. Morgenstern, "Ice nanoclusters at hydrophobic metal surfaces," *Nature Materials,* vol. 6, pp. 597-601, Aug 2007.
[202] A. Michaelides, A. Alavi, and D. A. King, "Insight into H2O-ice adsorption and dissociation on metal surfaces from first-principles simulations," *Physical Review B,* vol. 69, Mar 2004.
[203] A. Hodgson and S. Haq, "Water adsorption and the wetting of metal surfaces," *Surface Science Reports,* vol. 64, pp. 381-451, Sep 2009.
[204] G. B. Fisher and J. L. Gland, "THE INTERACTION OF WATER WITH THE PT(111) SURFACE," *Surface Science,* vol. 94, pp. 446-455, 1980.
[205] S. Haq, J. Harnett, and A. Hodgson, "Growth of thin crystalline ice films on Pt(111)," *Surface Science,* vol. 505, pp. 171-182, May 2002.
[206] J. L. Daschbach, B. M. Peden, R. S. Smith, and B. D. Kay, "Adsorption, desorption, and clustering of H2O on Pt(111)," *Journal of Chemical Physics,* vol. 120, pp. 1516-1523, Jan 2004.
[207] C. Puglia, A. Nilsson, B. Hernnas, O. Karis, P. Bennich, and N. Martensson, "PHYSISORBED, CHEMISORBED AND DISSOCIATED O-2 ON PT(111) STUDIED BY DIFFERENT CORE-LEVEL SPECTROSCOPY METHODS," *Surface Science,* vol. 342, pp. 119-133, Nov 1995.
[208] B. C. Stipe, M. A. Rezaei, W. Ho, S. Gao, M. Persson, and B. I. Lundqvist, "Single-molecule dissociation by tunneling electrons," *Physical Review Letters,* vol. 78, pp. 4410-4413, Jun 1997.
[209] J. L. Gland, B. A. Sexton, and G. B. Fisher, "OXYGEN INTERACTIONS WITH THE PT(111) SURFACE," *Surface Science,* vol. 95, pp. 587-602, 1980.
[210] H. Steininger, S. Lehwald, and H. Ibach, "ADSORPTION OF OXYGEN ON PT(111)," *Surface Science,* vol. 123, pp. 1-17, 1982.
[211] A. Eichler and J. Hafner, "Molecular precursors in the dissociative adsorption of O-2 on Pt(111)," *Physical Review Letters,* vol. 79, pp. 4481-4484, Dec 1997.
[212] A. Eichler, F. Mittendorfer, and J. Hafner, "Precursor-mediated adsorption of oxygen on the (111) surfaces of platinum-group metals," *Physical Review B,* vol. 62, pp. 4744-4755, Aug 2000.
[213] M. L. Bocquet, J. Cerda, and P. Sautet, "Transformation of molecular oxygen on a platinum surface: A theoretical calculation of STM images," *Physical Review B,* vol. 59, pp. 15437-15445, Jun 1999.
[214] J. Roques and A. B. Anderson, "Electrode potential-dependent stages in OHads formation on the Pt3Cr alloy (111) surface," *Journal of the Electrochemical Society,* vol. 151, pp. E340-E347, 2004.
[215] A. Ohma, T. Ichiya, K. Fushinobu, and K. Okazaki, "Theoretical analysis of oxygen reduction reaction and H2O2 formation and the impact of CF3SO3H coverage on Pt (111)," *Surface Science,* vol. 604, pp. 965-973, 6/15/ 2010.
[216] I. Kendrick, D. Kumari, A. Yakaboski, N. Dimakis, and E. S. Smotkin, "Elucidating the Ionomer-Electrified Metal Interface," *Journal of the American Chemical Society,* vol. 132, pp. 17611-17616, 2010/12/15 2010.
[217] "Jaguar," 7.5 ed. New York: Schrödinger, LLC, 2008.

[218] Y. Zhao and D. G. Truhlar, "The M06 suite of density functionals for main group thermochemistry, thermochemical kinetics, noncovalent interactions, excited states, and transition elements: two new functionals and systematic testing of four M06-class functionals and 12 other functionals," *Theoretical Chemistry Accounts,* vol. 120, pp. 215-241, May 2008.
[219] Y. Zhao and D. G. Truhlar, "Exploring the Limit of Accuracy of the Global Hybrid Meta Density Functional for Main-Group Thermochemistry, Kinetics, and Noncovalent Interactions," *Journal of Chemical Theory and Computation,* vol. 4, pp. 1849-1868, Nov 2008.
[220] J. P. Perdew, K. Burke, and Y. Wang, "Generalized gradient approximation for the exchange-correlation hole of a many-electron system," *Physical Review B,* vol. 54, p. 16533, 1996.
[221] J. P. Perdew, K. Burke, and M. Ernzerhof, "Generalized gradient approximation made simple," *Physical Review Letters,* vol. 77, pp. 3865-3868, Oct 28 1996.
[222] A. D. Becke, "DENSITY-FUNCTIONAL THERMOCHEMISTRY .3. THE ROLE OF EXACT EXCHANGE," *Journal of Chemical Physics,* vol. 98, pp. 5648-5652, Apr 1993.
[223] P. J. Stephens, F. J. Devlin, C. F. Chabalowski, and M. J. Frisch, "AB-INITIO CALCULATION OF VIBRATIONAL ABSORPTION AND CIRCULAR-DICHROISM SPECTRA USING DENSITY-FUNCTIONAL FORCE-FIELDS," *Journal of Physical Chemistry,* vol. 98, pp. 11623-11627, Nov 1994.
[224] P. J. Hay and W. R. Wadt, "Ab initio effective core potentials for molecular calculations. Potentials for K to Au including the outermost core orbitals," *The Journal of Chemical Physics,* vol. 82, pp. 299-310, 1985.
[225] M. C. Payne, M. P. Teter, D. C. Allan, T. A. Arias, and J. D. Joannopoulos, "ITERATIVE MINIMIZATION TECHNIQUES FOR ABINITIO TOTAL-ENERGY CALCULATIONS - MOLECULAR-DYNAMICS AND CONJUGATE GRADIENTS," *Reviews of Modern Physics,* vol. 64, pp. 1045-1097, Oct 1992.
[226] "Materials Studio," 5.0 ed. San Diego: Accelrys Software Inc., 2009.
[227] J. Kua and W. A. Goddard, "Chemisorption of Organics on Platinum. 2. Chemisorption of C2Hx and CHx on Pt(111)," *The Journal of Physical Chemistry B,* vol. 102, pp. 9492-9500, 1998/11/01 1998.
[228] J. Kua and W. A. Goddard, "Chemisorption of Organics on Platinum. 1. The Interstitial Electron Model," *The Journal of Physical Chemistry B,* vol. 102, pp. 9481-9491, 1998/11/01 1998.
[229] J. A. Dean, *Lange's Handbook of Chemistry*

New York, NY: McGraw-Hill Book Company, 1979.
[230] N. E. Singh-Miller and N. Marzari, "Surface energies, work functions, and surface relaxations of low-index metallic surfaces from first principles," *PHYSICAL REVIEW B,* vol. 80, p. 235407, 2009.
[231] H. Iddir, V. Komanicky, S. Ogut, H. You, and P. Zapol, "Shape of platinum nanoparticles supported on SrTiO3: Experiment and theory," *JOURNAL OF PHYSICAL CHEMISTRY C,* vol. 111, pp. 14782-14789, 2007.
[232] S. Baud, C. Ramseyer, G. Bihlmayer, S. Blugel, C. Barreteau, M. C. Desjonqueres*, et al.*, "Comparative study of ab initio and tight-binding electronic

structure calculations applied to platinum surfaces," *PHYSICAL REVIEW B,* vol. 70, p. 235423, 2004.

[233] J. L. F. Da Silva, C. Stampfl, and M. Scheffler, "Converged properties of clean metal surfaces by all-electron first-principles calculations," *SURFACE SCIENCE* vol. 600, pp. 703-715, 2006.

[234] G. Boisvert, L. J. Lewis, and M. Scheffler, "Island morphology and adatom self-diffusion on Pt(111)," *PHYSICAL REVIEW B,* vol. 57, pp. 1881-1889, 1998.

[235] M. Connolly, "Analytical molecular surface calculation," *Journal of Applied Crystallography,* vol. 16, pp. 548-558, 1983.

[236] B. Krishnamurthy and S. Deepalochani, "Performance of Platinum Black and Supported Platinum Catalysts in a Direct Methanol Fuel Cell," *International Journal of Electrochemical Science,* vol. 4, pp. 386-395, Mar 2009.

[237] I. Esparbé, E. Brillas, F. Centellas, J. A. Garrido, R. M. Rodríguez, C. Arias*, et al.*, "Structure and electrocatalytic performance of carbon-supported platinum nanoparticles," *Journal of Power Sources,* vol. 190, pp. 201-209, 5/15/ 2009.

[238] A. Ignaszak, S. Ye, and E. d. Gyenge, "A Study of the Catalytic Interface for O2 Electroreduction on Pt: The Interaction between Carbon Support Meso/Microstructure and Ionomer (Nafion) Distribution," *The Journal of Physical Chemistry C,* vol. 113, pp. 298-307, 2009/01/08 2008.

[239] G. Sasikumar, J. W. Ihm, and H. Ryu, "Dependence of optimum Nafion content in catalyst layer on platinum loading," *Journal of Power Sources,* vol. 132, pp. 11-17, 5/20/ 2004.

[240] A. E. Feiring and E. R. Wonchoba, "Aromatic monomers with pendant fluoroalkylsulfonate and sulfonimide groups," *Journal of Fluorine Chemistry,* vol. 105, pp. 129-135, Aug 2000.

[241] J. Shin, S. M. Jensen, J. Ju, S. Lee, Z. Xue, S. K. Noh*, et al.*, "Controlled functionalization of crystalline polystyrenes via activation of aromatic C-H bonds," *Macromolecules,* vol. 40, pp. 8600-8608, Nov 27 2007.

[242] T. S. Jo, S. H. Kim, J. Shin, and C. Bae, "Highly Efficient Incorporation of Functional Groups into Aromatic Main-Chain Polymer Using Iridium-Catalyzed C-H Activation and Suzuki-Miyaura Reaction," *Journal of the American Chemical Society,* vol. 131, pp. 1656-+, Feb 11 2009.

[243] T. M. Boller, J. M. Murphy, M. Hapke, T. Ishiyama, N. Miyaura, and J. F. Hartwig, "Mechanism of the mild functionalization of arenes by diboron reagents catalyzed by iridium complexes. Intermediacy and chemistry of bipyridine-ligated iridium trisboryl complexes," *Journal of the American Chemical Society,* vol. 127, pp. 14263-14278, Oct 19 2005.

[244] G. A. Chotana, M. A. Rak, and M. R. Smith, "Sterically directed functionalization of aromatic C-H bonds: Selective borylation ortho to cyano groups in arenes and heterocycles," *Journal of the American Chemical Society,* vol. 127, pp. 10539-10544, Aug 3 2005.

[245] N. Miyaura and A. Suzuki, "PALLADIUM-CATALYZED CROSS-COUPLING REACTIONS OF ORGANOBORON COMPOUNDS," *Chemical Reviews,* vol. 95, pp. 2457-2483, Nov 1995.

[246] C. Iojoiu, M. Marechal, F. Chabert, and J. Y. Sanchez, "Mastering sulfonation of aromatic polysulfones: Crucial for membranes for fuel cell application," *Fuel Cells,* vol. 5, pp. 344-354, Aug 2005.